New Methods of Tilt Measurement for Applications in Medical Devices

A DISSERTATION SUBMITTED TO THE
GRADUATE SCHOOL OF ENGINEERING AND SCIENCE OF
SHIBAURA INSTITUTE OF TECHNOLOGY

by

DAO VIET HUNG

IN PARTIAL FULFILLMENT OF THE REQUIREMENTS
FOR THE DEGREE OF

DOCTOR OF ENGINEERING

SEPTEMBER 2016

Acknowledgments

I owe a deep sense of gratitude to all kindnesses and supports for my studies. Like once said that no one succeeds all by themselves, the work would not have been completed without the help of many individuals.

First and foremost, I would like to send my deepest appreciation to my family for their spiritual support, which motivates and encourages me to accomplish the research successfully. Moreover, those achievements of mine could not be attained without the presence of my wife, who has always been by my side and has given me strength to overcome the difficulties during these three years of hard working.

I would like to express my gratitude to my supervisor, Professor Takashi Komeda, for his research orientation from the very beginning of my study, the guidelines, valuable advice, throughout the time of the research as well as his enthusiastic supervision and encouragement for the successful completion of this dissertation.

I would also like to thank Prof. Akihiko Hanafusa, Prof. Kazuhisa Ito, Prof. Akihiro Matsumoto, and Prof. Shinichiro Yamamoto in the review board for their perceptive comments on the thesis in view of the fact that these comments not only led to the enhancement of my work but also suggested new tendencies for the research development. I truly appreciate the reviewers for dedicating their time to help me to successfully complete the study.

Being able to study in Japan gave me not only a great opportunity, but also the hardship on the grounds of the differences in term of culture and lifestyle. Hence, I would like to send my thankfulness to staff

members of Shibaura Institute of Technology, particularly personnel of the Student Affairs Section and Graduate School Section for their kind help and endless support. In addition, I am very grateful to my Japanese friends who have willingly helped me to become familiar with a new place, way of life and language here in Japan. Thanks to their moral support, I had more time to work at a high level without being distracted.

Furthermore, immeasurable appreciation is extended to the Olympus company for providing me a chance to get the use of endoscopic devices, together with Mr. Keita Suzuki who gave me beneficial advice related to endoscopic surgery. Following that, I would like to acknowledge the support of my friend, Mr. Lawrence E. Walker, who helped me proof checking to detect any language errors. My publications would not have been accomplished without his assistance.

Last but not least, I am very grateful to my kind friends and colleagues who are one way or another shared their support and understanding spirit, thank you all.

Saitama, September 2, 2016

Dao Viet Hung

Abstract

Tilt measurement is useful for a variety of applications. In medical field, the tilt angles can be used to determine inclinations of the human bodies, angles of human joints, as well as orientations of surgical devices. Tilt measurement is also necessary for consumer electronics, industrial electronics, avionics, and other applications in both civil and military, which require the inclinations of an object with respect to either vertical axis or horizontal plane.

Measuring the tilt angles with inertial sensors is a well-known technique. An accelerometer can sense any change in a linear velocity as well as measuring the constant gravitational acceleration. Hence, by using a triaxial acceleration sensor, three orthogonal projections of the gravity vector onto the sensor frame can be determined for computing the tilt angles. The calculation formulas depend on the definition of the tilt angles which can be classified into some major types.

Both analog and digital accelerometers are commonly utilized for measuring the tilt angles. Digital accelerometers are a good choice in many cases, whereas an analog accelerometer could be necessary when the system requirements are beyond the capability of the digital sensor. However, when using the analog sensors, the effects of the electromagnetic interference must be taken into account.

Another challenge in measuring the tilt angles is the influence of movement and vibration. Any linear acceleration can perturb the sensor data, and therefore may degrade the measurement accuracy. Consequently, additional sensors or algorithms should be integrated into the systems if the static or quasi-static conditions cannot be guaranteed.

The objectives of this work are to partially solve the limitations of the tilt measurement technique in the medical field. The whole work is divided into four elemental studies. The first three studies are proposed based on the same idea that is the interference cancellation can be achieved by changing the mounting orientation of the acceleration sensors. In each study, a rotation matrix is proposed to rotate the sensor frame and convert the calculation formulas. This change allows computing the tilt angles from the differences between the voltages of three sensor outputs. Thus, an advantage of the differential signaling technique, that is interference immunity, is taken within the single-ended systems. In spite of using the same mechanism, each study plays a dedicated role because they improve three major types of the tilt components.

In the last study, a new sensor-fusion method is proposed to reduce the effects of motion on the tilt angles. The key algorithm is a so-called predict-and-choose process which combines the accelerometer readings and the output data of a triaxial gyroscope. During the dynamic states, this process predicts three gravitational components to estimate the tilt angles. Therefore, the dependence of the computed results on the motion can be reduced.

In each study, both simulations and experiments have been performed to validate the proposed methods. The results showed significant improvements in the output angles. Although there are some shortcomings that need to be addressed in a further research, the reported results may contribute to increasing the applicability of the tilt measurement technique in medical systems. Moreover, the advantages of the first three studies could be useful for applications in other fields.

Contents

List of Figures

List of Tables

Nomenclature

Roman Symbols

$\mathbf{a}$	linear acceleration vector
a_X	orthogonal projection of $\mathbf{a}$ onto the X-axis
a_Y	orthogonal projection of $\mathbf{a}$ onto the Y-axis
a_Z	orthogonal projection of $\mathbf{a}$ onto the Z-axis
$\mathbf{F}$	sum of $\mathbf{g}$ and $\mathbf{a}$
F_X	orthogonal projection of $\mathbf{F}$ onto the X-axis
F_Y	orthogonal projection of $\mathbf{F}$ onto the Y-axis
F_Z	orthogonal projection of $\mathbf{F}$ onto the Z-axis
g	standard gravity, about $9.8 m/s^2$
$\mathbf{g}$	gravitational vector
g_X	orthogonal projection of $\mathbf{g}$ onto the X-axis
g_x	orthogonal projection of $\mathbf{g}$ onto the x-axis
g_Y	orthogonal projection of $\mathbf{g}$ onto the Y-axis
g_y	orthogonal projection of $\mathbf{g}$ onto the y-axis
g_Z	orthogonal projection of $\mathbf{g}$ onto the Z-axis

g_z orthogonal projection of **g** onto the z-axis

n external noise

n_x noise in the measured signal of the x-axis

n_y noise in the measured signal of the y-axis

n_z noise in the measured signal of the z-axis

$O_1O_2O_3$ coordinate system of the measured object

r_F downsampling ratio for accelerometer

r_ω downsampling ratio for gyroscope

R rotation matrix

$R_X(\alpha)$ elemental rotation about the X-axis by α

$R_Y(\beta)$ elemental rotation about the Y-axis by β

$R_Z(\gamma)$ elemental rotation about the Z-axis by γ

s accelerometer sensitivity

U_x output voltage of the sensor on the x-axis

U_y output voltage of the sensor on the y-axis

U_z output voltage of the sensor on the z-axis

v, v' column vectors which represent coordinates of a point

XYZ conventional mounting orientation of the accelerometers

xyz proposed mounting orientation of the accelerometers

Greek Symbols

α, β, γ rotation angles

Δ_t time interval between two consecutive samples after downsampling

ω_X angular velocity about the X-axis

ω_Y angular velocity about the Y-axis

ω_Z angular velocity about the Z-axis

Φ the third elemental rotations of ZYX convention Euler angles

Ψ the first elemental rotations of ZYX convention Euler angles

Θ the second elemental rotations of ZYX convention Euler angles

θ_1, θ_2 two tilt angles when non-Euler angles are used

Superscripts

a active

Subscripts

C conventional method

c common-mode

d differential-mode

k x, y, z, or all of them

n time point with labels in chronological order

O original (angles)

P proposed method

Acronyms

ADC analog-to-digital converter

CMRR common-mode rejection ratio

DAQ data acquisition

deg degree

EMI electromagnetic interference

f video frame

FS full scale

IC integrated circuit

IMU inertial measurement unit

MEMS micro-electro-mechanical systems

NOSCAR Natural Orifice Surgery Consortium for Assessment and Research

NOTES natural orifice translumenal endoscopic surgery

RFI radio frequency interference

RMS root mean square

c cosine function

SD standard deviation

s sine function

Chapter 1

Introduction

This chapter provides an outline of the whole work. In the first section, an overview of the tilt measurement technique and its challenges are introduced. This is the basis for the research objectives in the following section. After that, the outstanding results of each elemental study are summarized to highlight the contributions of the work. Finally, a listing of all chapters provides a panoramic view of the entire study.

1.1 Overview

In recent years, the development of micro-electro-mechanical systems (MEMS) technology allows utilizing the inertial sensors in more and more applications, including tilt measurement. A low cost three-axis MEMS accelerometer, with a size of a few millimeters, can measure three Cartesian components of any acceleration. In the static or quasi-static conditions, these components are three elements of the gravitational vector, by which the tilt angles can be computed with trigonometric formulas. Because of the small size and ease of use, the MEMS accelerometers are not only integrated into new designs, but also used to upgrade the existing systems.

Measuring the orientation with accelerometers has some major challenges. First, the sensor errors could significantly affect the measurement accuracy. Thus,

many studies have focused on sensor calibration, sensor-fusion, and calculation algorithm to reduce the influence of these intrinsic limitations. An analog accelerometer can overcome some common limitations of the digital sensors. However, when using the analog accelerometer, we face another challenge: interference susceptibility. Electromagnetic interference (EMI) can cause unwanted signals in transmission lines, and therefore disturb the final results. Although prevailing methods of interference reduction can effectively suppress the external noise, almost all solutions require additional hardware or software or both of them, which could limit the applicability of the measurement system. The last challenge is the highest barrier in tilt measurement: effects of motion. According to the above mechanism, when vibration or movement appears, the accelerometer readings are no longer the gravitational components. In this case, additional processes or sensors are necessary to maintain the measurement accuracy. However, all of them have their own advantages and drawbacks. In general, there is always the need for developing the new methods which address the above limitations in the new way to expand the applicability of the tilt measurement systems.

1.2 Objectives

The objectives of this work are to partially solve the limitations of the tilt measurement technique in the medical field. The whole work consists of four elemental studies. The first three studies address the limitation of interference susceptibility of the analog accelerometers for expanding the applicability. Meanwhile, reducing the effects of motion on the tilt angles is taken into account in the last study.

First three studies have the same basic idea in which the sensor frame of an accelerometer is rotated by rotation matrices before being attached onto the measured object. This change allows converting the conventional calculation formulas to take an advantage of the differential signaling technique within a single-ended system. Hence, the interference cancellation can be achieved without the need for any additional hardware or software. Because the tilt angles can be defined in various ways and each of them plays a dedicated role, three studies have been proposed to improve three major types of the tilt components.

In the fourth study, the effects of motion on the tilt angles are reduced by a new sensor-fusion method. This method allows estimating three gravitational components under all conditions. The key algorithm is a so-called *predict-and-choose* process which combines the output data of an accelerometer and a gyroscope. The calculation algorithm guarantees that even in highly dynamic testing conditions, the estimated angles are reliable without any cumulative error. This study is developed to be applied in new surgical devices, particularly for natural orifice translumenal endoscopic surgery (NOTES) systems.

Because of time and equipment constraints, the scope of the whole work is limited to be applied in the initially expected area, the medical field. The applications would be expanded if further studies are conducted under other conditions with dedicated measurement systems. Although this prediction has not been validated, the author believes that the idea of the first three studies can be utilized to enhance the EMI immunity and reduce the hardware complexity for many applications in a variety of fields.

1.3 Contributions

This work contributes three methods of EMI reduction and a method of sensor-fusion to enhance the accuracy of the tilt measurement systems. In order to highlight the difference among the first three methods, the definition of the tilt should be briefly clarified.

According to the literature, the author classified the definitions of the tilt into two categories: using Euler angles and using the geometrical relations (non-Euler angles). In the first type, two of the three Euler angles in yaw-pitch-row sequence (ZYX convention), namely pitch and roll, are used to define two components of the tilt. These angles play different roles, and therefore have different applications. In the second category, the tilt is defined by the geometrical relations between the sensor frame and the reference frame. In this type, the tilt has two components; however, their roles are interchangeable because of the similarity in the definitions. Hence, three are three major types of the tilt angles.

The main contributions of this work are listed below:

EMI reduction in measuring the pitch angle By proposing a so-called *pitch-improved* rotation matrix (R_Θ) to define a new mounting orientation for the accelerometers, the author achieved a new measurement method in which the pitch angle can be measured without any error caused by EMI. The experimental results showed that the error in the pitch angle was reduced 2–20 times, in comparison with the conventional method. Hence, the second angle of the ZYX convention Euler angles was improved.

EMI reduction in measuring the roll angle In this study, the author also proposed a so-called *roll-improved* rotation matrix (R_Φ) to define a new mounting orientation for the accelerometers. Then, the new method was validated by an upgraded simulation model and a new experimental system. The results showed that by this method, the error in the roll angle was reduced 5–22.5 times. Consequently, the third angle of the ZYX convention Euler angles was significantly improved.

EMI reduction in measuring both non-Euler angles In the third study, the author theoretically proposed a solution to improve the two interchangeable tilt components simultaneously by a rotation matrix, $R_{\theta_{1,2}}$. After this change, both non-Euler tilt angles can be immune to EMI at the same time, instead of only one angle as in the two above studies. Additionally, some alternative solutions for rotating the sensor were also proposed. Each of them rotates the sensor frame in a different way. Thus, the mechanical attachment in each application will be more flexible.

Sensor-fusion in tilt measurement for surgical devices In this contribution, the author proposed the *predict-and-choose* process to combine the output data of an accelerometer and a gyroscope. This process allows predicting the gravitational components for calculating the tilt angles under both static and dynamic states. Compared with results of a reference method, the proposed method

has smaller errors, smoother angle changes, and a smaller delay time, although the complexity of the hardware is almost unchanged.

The methods in the first three contributions have a common outstanding advantage that is the external EMI can be rejected without the need for any additional component or extra process. The EMI cancellation mechanism of the balanced lines has been achieved, although the proposed systems are single-ended. In other words, the author's designs take an advantage of the differential signaling technique without the need for differential accelerometers, additional connection wires, and other necessary components of the differential systems. In conclusion, a totally new idea of EMI reduction in tilt measurement has been proposed, developed, and validated. This idea may be a good solution for many applications; particularly when the sensor is far from the processing circuit, the whole system works in a strong noise environment, and the size of all components should be kept to a minimum.

1.4 Structure of This Work

This dissertation is composed of seven chapters. Chapter 1 has provided the outline of the whole work. The next chapters are listed below:

Chapter 2 summarizes a technical background of the tilt measurement technique and reviews the related studies. The content of this chapter includes: rotation and mathematical representation, tilt definition and angle calculation, and the common limitations of tilt measurement with inertial sensors. Simultaneously, many related studies are reviewed.

Chapter 3 describes the new method of interference reduction in measuring the pitch angle with analog accelerometers. The structure of this chapter is similar to a scientific research articles, including descriptions of the method, simulation steps, and experiments processes.

Chapter 4 presents a development and validation of the new interference reduction method for measuring the roll angle with analog accelerometers. The

structure of this chapter is similar to chapter 2. However, the objectives and implements of the two studies are different.

Chapter 5 briefly introduces the method that simultaneously improves the noise immunity of both non-Euler angles. Only equations are formulated here because there is no change in the validation method. This chapter also provides overall evaluations of the three presented studies and develops some alternative mounting solutions.

Chapter 6 presents the new method for estimating the tilt angles of endoscopic images. Here, the new sensor-fusion method that combines the data of an accelerometer and a gyroscope is proposed. The results are evaluated by being applied in a well-known application, endoscopic horizon stabilization.

The dissertation ends with conclusions and future works in chapter 7.

Chapter 2

Technical Background and Literature Review

This chapter presents an overview of tilt measurement and reviews the related studies. In the first section, the fundamental of rotation and mathematical representations are briefly presented. This part provides the most important concepts and equations for the whole work. In the next section, a variety of the tilt definitions in many studies are reviewed. Conventional methods of tilt sensing with inertial sensors are also described in this part. The last section summarizes major challenges in tilt measurement, including limitations of the sensor and limitations of the calculation algorithm. Some prevailing solutions are also introduced to clarify the novelty of the contributions in this work.

2.1 Rotation and Representation

2.1.1 Basic Concepts

In three dimensions, any rotation of a point about a reference frame can be performed by a 3×3 rotation matrix. The rotation, therefore, can be expressed by an equation, as in Eqn. (2.1). Here, the rotation matrix R^a rotates the point represented by a column vector v to a new position represented by v'; the reference

frame is XYZ. In some cases, row vectors can also be used if the positions of R^a and v in the matrix multiplication are interchanged. The superscript a in R^a denotes the active rotation (alibi transformation) in which the point is moved while the reference frame is fixed [32], as depicted in Fig. 2.1(a). In many cases, the passive rotation (alias transformation) is preferred. Here, the point (or vector v) is fixed while the reference frame (XYZ) moves in the opposite direction, as in Fig. 2.1(b). This representation is very popular in engineering, when sensors are placed on the moving parts.

$$\begin{bmatrix} v'_X \\ v'_Y \\ v'_Z \end{bmatrix} = R^a_{3\times 3} \begin{bmatrix} v_X \\ v_Y \\ v_Z \end{bmatrix} \tag{2.1}$$

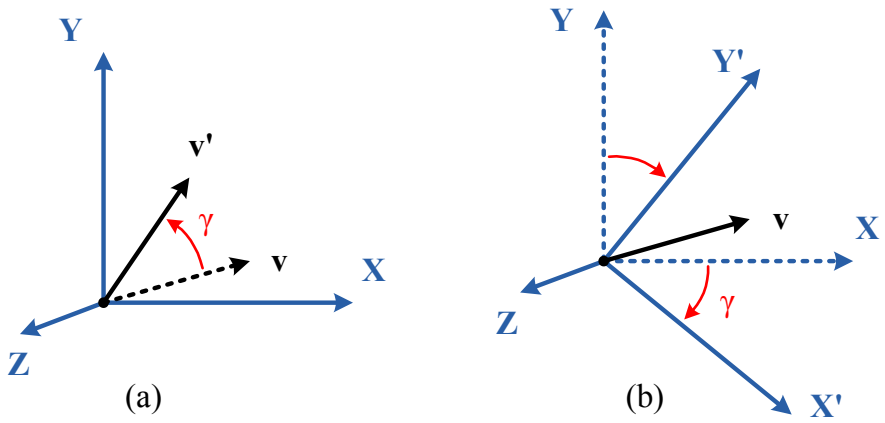

Figure 2.1: A rotation about Z-axis: (a) active rotation and (b) passive rotation

Every rotation can be achieved by composing three elemental rotations which are the rotations about three axes of the Cartesian coordinate system. Equivalently, the rotation matrix R^a can be decomposed as the product of three elemental rotation matrices [13]. The first elemental rotation matrix rotates the point about the X-axis in Eqn. (2.2); the second one rotates the point about the Y-axis in Eqn. (2.3); and the last matrix rotates the point about the Z-axis in Eqn. (2.4). Here, the rotations are positive if they appear counterclockwise when

observing in the negative direction of the corresponding rotation axes.

$$R_X^a(\alpha) = \begin{bmatrix} 1 & 0 & 0 \\ 0 & \cos\alpha & -\sin\alpha \\ 0 & \sin\alpha & \cos\alpha \end{bmatrix} \tag{2.2}$$

$$R_Y^a(\beta) = \begin{bmatrix} \cos\beta & 0 & \sin\beta \\ 0 & 1 & 0 \\ -\sin\beta & 0 & \cos\beta \end{bmatrix} \tag{2.3}$$

$$R_Z^a(\gamma) = \begin{bmatrix} \cos\gamma & -\sin\gamma & 0 \\ \sin\gamma & \cos\gamma & 0 \\ 0 & 0 & 1 \end{bmatrix} \tag{2.4}$$

When composing the above matrices, the position of the factors in the multiplication determines the order in the rotation sequence. Before distinguishing this order, there are two terms should be clarified: extrinsic rotation and intrinsic rotation. Extrinsic rotations are rotations about the axes of the fixed coordinate system as depicted in Fig. 2.2(a), whereas intrinsic rotations are rotations about the axes of the rotating coordinate system, as in Fig. 2.2(b). The rotating coordinate system is initially aligned with the fixed one; however, its orientation changes after each elemental rotation [24]. Equation (2.5) is an example in which: if the rotations are intrinsic, the rotation order is X-Y-Z; meanwhile, if the rotations are extrinsic, the order is inverted. In the active rotations, because the reference frame is fixed, the extrinsic rotation is commonly used for representation. In Eqn. (2.5), elements of R^a are calculated from the trigonometric functions of the rotation angles. Here, s is the abbreviation of the sine function (e.g., s_α is $\sin\alpha$), while c is the abbreviation of the cosine function.

$$R^a = R_X^a(\alpha)R_Y^a(\beta)R_Z^a(\gamma) = \begin{bmatrix} c_\beta c_\gamma & -c_\beta s_\gamma & s_\beta \\ c_\alpha s_\gamma + s_\alpha s_\beta c_\gamma & c_\alpha c_\gamma - s_\alpha s_\beta s_\gamma & -s_\alpha c_\beta \\ s_\alpha s_\gamma - c_\alpha s_\beta c_\gamma & s_\alpha c_\gamma + c_\alpha s_\beta s_\gamma & c_\alpha c_\beta \end{bmatrix} \tag{2.5}$$

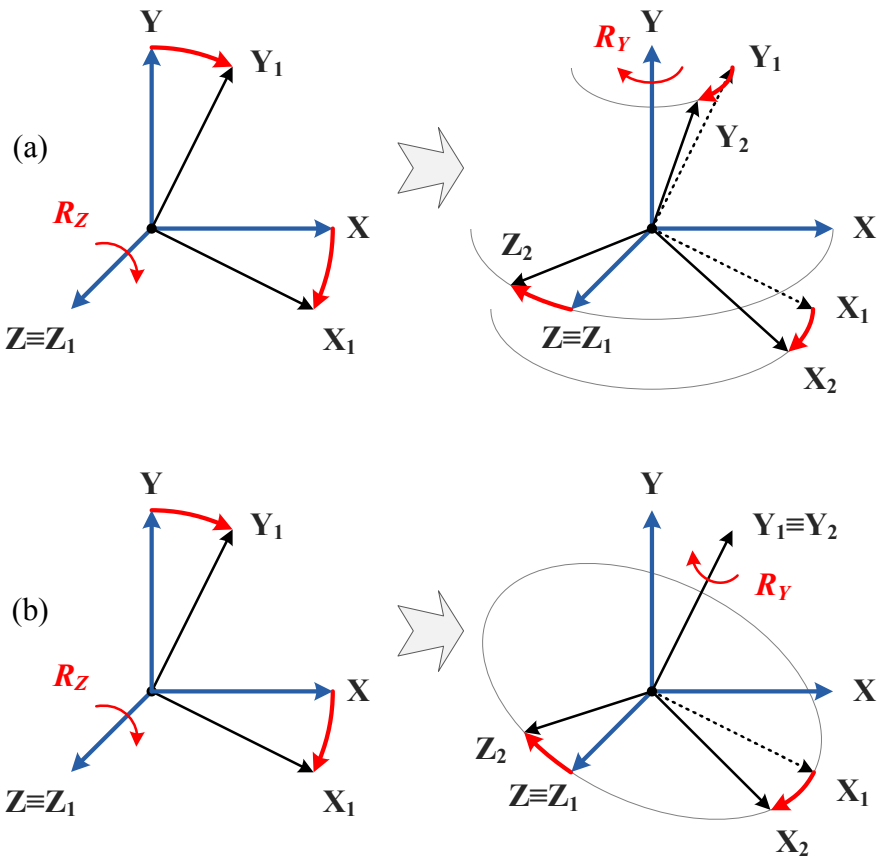

Figure 2.2: Two types of rotation: (a) extrinsic rotation and (b) intrinsic rotation

2.1.2 Rotation of Sensors

In this work, the passive rotation is used. The main reason is that the sensors are attached on the measured object; therefore, the coordinate system of the sensors is moved, while the gravitational vector is fixed. This means that the use of the passive rotation is more convenient, as mentioned in Sec. 2.1.1. Because the rotation directions of the reference frame (in passive rotation) and the rotation of the point or vector (in active rotation) are always opposite, all sine functions in rotation matrices of the passive rotation must be reversed in sign. On other words, the rotation of the sensors can be represented by three elemental passive

rotation matrices, as expressed in Eqn. (2.6), Eqn. (2.7), and Eqn. (2.8).

$$R_X(\alpha) = \begin{bmatrix} 1 & 0 & 0 \\ 0 & \cos\alpha & \sin\alpha \\ 0 & -\sin\alpha & \cos\alpha \end{bmatrix} \tag{2.6}$$

$$R_Y(\beta) = \begin{bmatrix} \cos\beta & 0 & -\sin\beta \\ 0 & 1 & 0 \\ \sin\beta & 0 & \cos\beta \end{bmatrix} \tag{2.7}$$

$$R_Z(\gamma) = \begin{bmatrix} \cos\gamma & \sin\gamma & 0 \\ -\sin\gamma & \cos\gamma & 0 \\ 0 & 0 & 1 \end{bmatrix} \tag{2.8}$$

The composition in Eqn. (2.9) represents a Z-Y-X passive rotation sequence. The previously mentioned extrinsic rotations (active) become intrinsic rotations (passive) in this equation because the sensors are rotated about the axes of themselves. This rotation sequence is widely known as the yaw-pitch-roll order or ZYX convention Euler angles which is commonly used in orientation measurement; more details are described in the next sections.

$$R = R_X(\alpha)R_Y(\beta)R_Z(\gamma) = \begin{bmatrix} c_\beta c_\gamma & c_\beta s_\gamma & -s_\beta \\ s_\alpha s_\beta c_\gamma - c_\alpha s_\gamma & s_\alpha s_\beta s_\gamma + c_\alpha c_\gamma & s_\alpha c_\beta \\ c_\alpha s_\beta c_\gamma + s_\alpha s_\gamma & c_\alpha s_\beta s_\gamma - s_\alpha c_\gamma & c_\alpha c_\beta \end{bmatrix} \tag{2.9}$$

2.2 Overview of Tilt Measurement

2.2.1 Definitions of the Tilt Angles

There are two common methods to define the tilt of an object. In the first method, two of the three Euler angles in yaw-pitch-roll sequence, namely roll and pitch, are used to represent the tilt of an object with respect to the horizontal plane [15, 20, 37], as depicted in Fig. 2.3. The initial position of the sensor, with the positive O_3-axis in the vertical downward direction, is considered as the reference frame. In this sequence, yaw does not affect the tilt (therefore Ψ is considered as

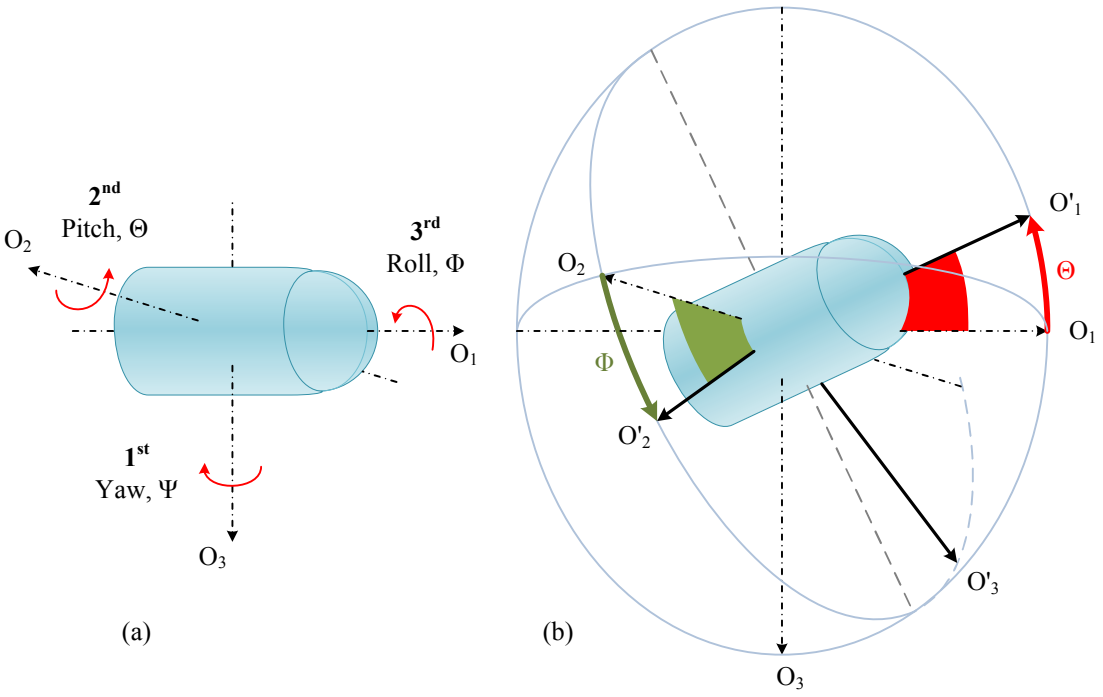

Figure 2.3: Definition of the tilt angles based on the yaw-pitch-roll order Euler angles: (a) initial position and (b) two tilt angles

zero in Fig. 2.3), pitch (Θ) changes the inclination of the O_1-axis, and roll (Φ) is the rotation angle of the object about the moving O_1-axis [13]. Since the two angle play different roles, they are not interchangeable.

In the second method, two components of the tilt are defined as shown in Fig. 2.4. Here, one angle (θ_1) is the inclination of the O_1-axis, while another one (θ_2) is the inclination of the O_2-axis, with respect to the horizontal plane [27, 28, 45]. This definition is not based on any rotation sequence; therefore, the roles of the two components are interchangeable. When being compared with the Euler angles, θ_1 seem to be same as Θ. In contrast, θ_2 is really different from Φ, particularly when $|\Theta|$ increases to 90 deg.

In some studies, a similar definition of $\theta_{1,2}$ can be found. In Fig. 2.5(a), the tilt components (θ'_1 and θ'_2) are defined as the angles of the O_1- and O_2-axes with the vertical upward direction [30]. Meanwhile, in Fig. 2.5(b), the angle between O_3-axis and the negative gravitational vector (θ_3) is used [31]. In this work, $\theta_{1,2}$,

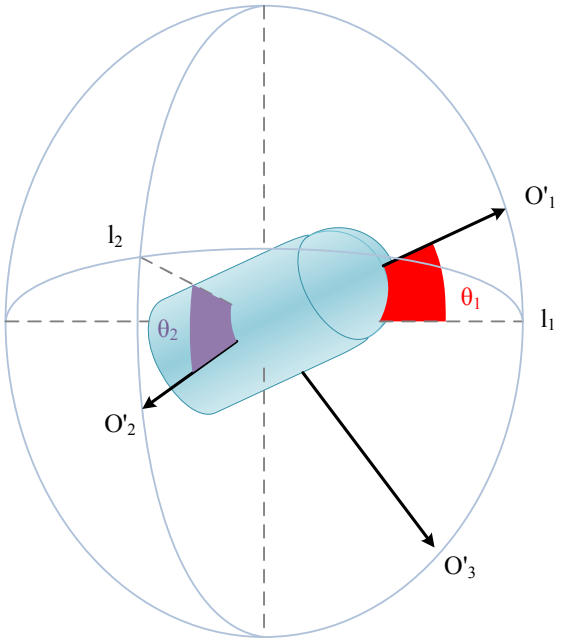

Figure 2.4: Definition of the tilt in which two components are interchangeable

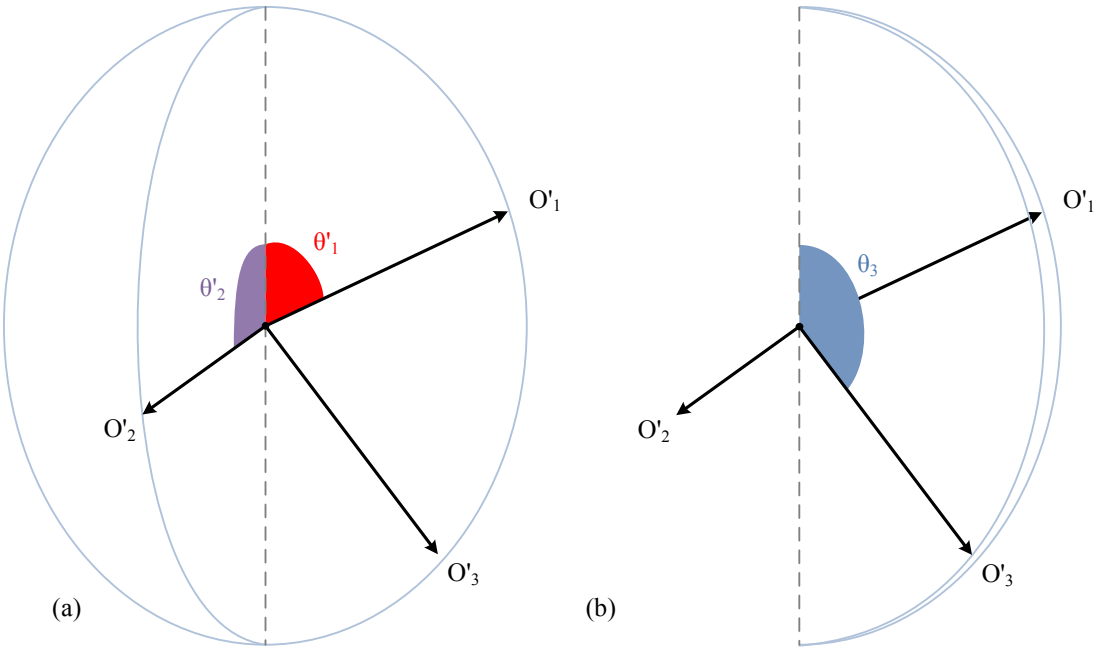

Figure 2.5: Another definition of the tilt based on the non-Euler angles: (a) the tilt has two components and (b) only one inclination is used

$\theta'_{1,2}$, and θ_3 are called non-Euler angles. Although there are some differences between their definitions and applications; the values of $\theta_{1,2}$, $\theta'_{1,2}$, and θ_3 can be calculated by the same method. Therefore, in this work, only calculations of θ_1 and θ_2 are taken into account.

2.2.2 Conventional Method of Tilt Measurement

2.2.2.1 Sensors and the Mounting Orientation

Tilt measurement with triaxial accelerometers is a well-known technique. The basic concept is that the tilt angles can be calculated from three components of the gravitational vector ($\mathbf{g}$). In general, the mounting position of the sensor is customizable as long as their coordinate axes are parallel to those of the measured object, as shown in Fig. 2.6. Hence, the tilt of the sensor is also the inclination of the measured object. During static or quasi-static conditions, the tilt angles are calculated from absolute voltages of the sensor outputs; the formulas depend on which type of angles is used to define the tilt.

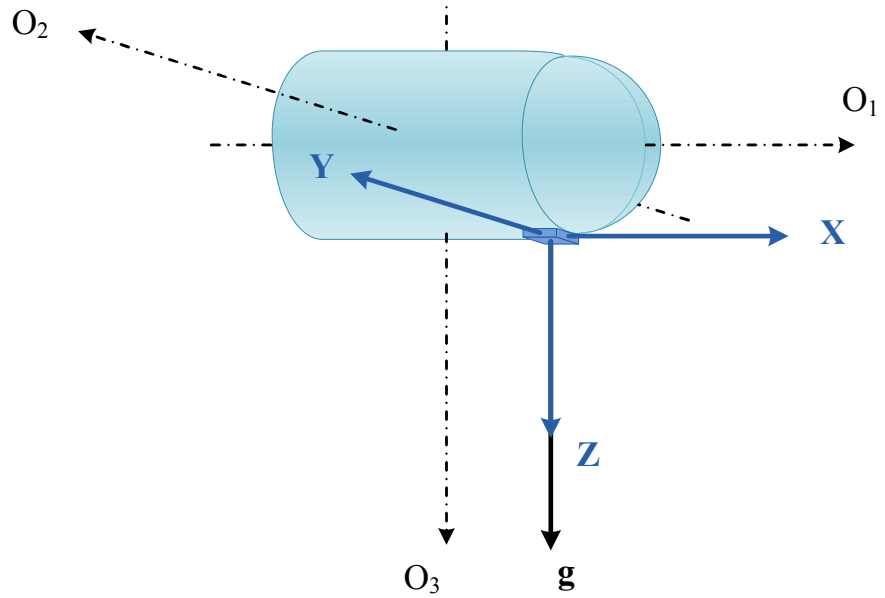

Figure 2.6: Coordinate system of the measured object and the conventional mounting method for accelerometers

2.2.2.2 Using the Euler Angles

When using the Euler angles, calculation of the tilt is built from the rotation sequence. As mentioned in Sec. 2.1.2, the rotation matrix of the yaw-pitch-roll order (ZYX convention) Euler angles is expressed in Eqn. (2.9). Because the Z-axis of the reference frame points vertically downward, the gravitational vector is initially represented by a column vector that is $[0\ 0\ 1]^T$. Thus, when the rotation sequence changes the orientation of the sensor, new coordinates of $\mathbf{g}$ are calculated by Eqn. (2.10) and then by Eqn. (2.11). Here, $\mathbf{g}$ has been normalized to make sure the rigor of the equation.

$$\mathbf{g} = R_{ZYX} \begin{bmatrix} 0 \\ 0 \\ 1 \end{bmatrix} \tag{2.10}$$

$$\frac{1}{|\mathbf{g}|} \begin{bmatrix} g_X \\ g_Y \\ g_Z \end{bmatrix} = \begin{bmatrix} -\sin\Theta \\ \cos\Theta \sin\Phi \\ \cos\Theta \cos\Phi \end{bmatrix} \tag{2.11}$$

On the basis of Eqn. (2.11), the value of Φ can be computed by Eqn. (2.12) and Θ is computed in Eqn. (2.13). These calculations can also be built from Fig. 2.7. In Eqn. (2.12), the $\arctan 2$ function (with two arguments) is used instead of the arctan function (only one argument) to return the appropriate quadrant of the computed angle. The $\arctan 2$ function can gather information on the signs of the two inputs and the output of the tradition arctan function, whose range is $(-\pi/2, +\pi/2)$, to return the correct result in the range of $(-\pi, +\pi)$.

$$\Phi = \arctan 2(g_Y, g_Z) \tag{2.12}$$

$$\Theta = \arcsin\left(-\frac{g_X}{\sqrt{g_X^2 + g_Y^2 + g_Z^2}}\right) \tag{2.13}$$

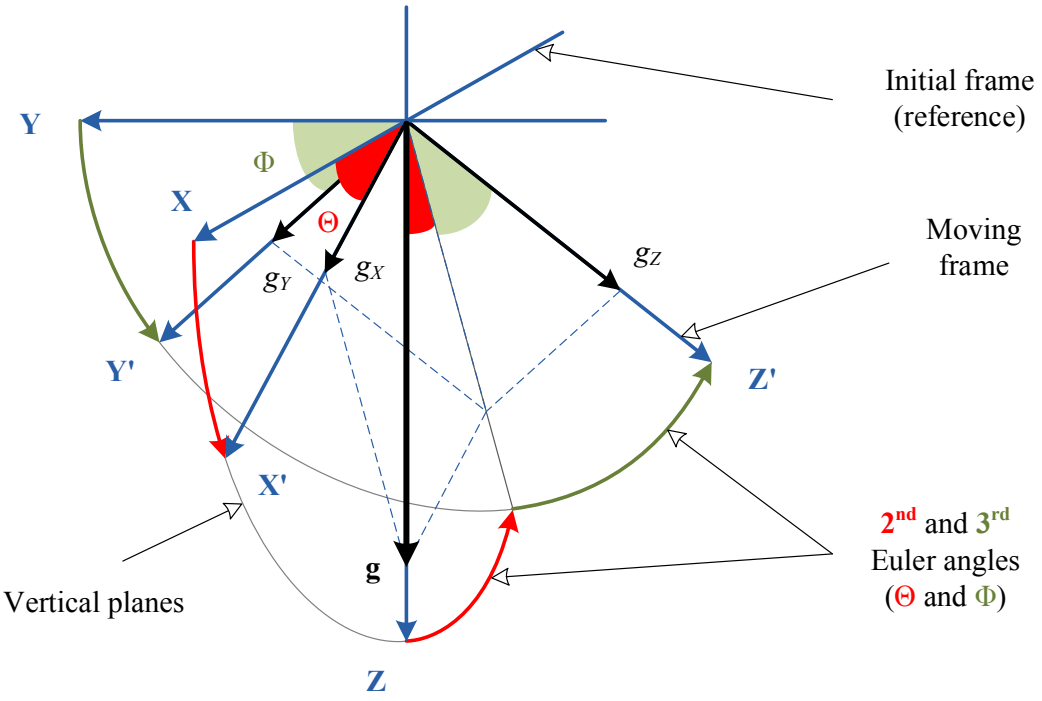

Figure 2.7: Calculation of the tilt when using the Euler angles

2.2.2.3 Using the Non-Euler Angles

Because the non-Euler angles are defined by the geometric relations, the calculation of the tilt is built visually. In Fig. 2.8, the sum of θ_1 and the angle between g_X and **g** is 90 deg. Hence, θ_1 can be computed by Eqn. (2.14). Here, in order to make the form of Eqn. (2.14) be same as Eqn. (2.13), a minus sign is added. In other works, this sign could be changed, depending on the convention of the author. Similarly, θ_2 can be determined by Eqn. (2.15). When the tilt angles are defined by the remaining methods (see Fig. 2.5), their values can be calculated by the same type of equation or computed from θ_1 and θ_2.

$$\theta_1 = \arcsin\left(-\frac{g_X}{\sqrt{g_X^2 + g_Y^2 + g_Z^2}}\right) \tag{2.14}$$

$$\theta_2 = \arcsin\left(-\frac{g_Y}{\sqrt{g_X^2 + g_Y^2 + g_Z^2}}\right) \tag{2.15}$$

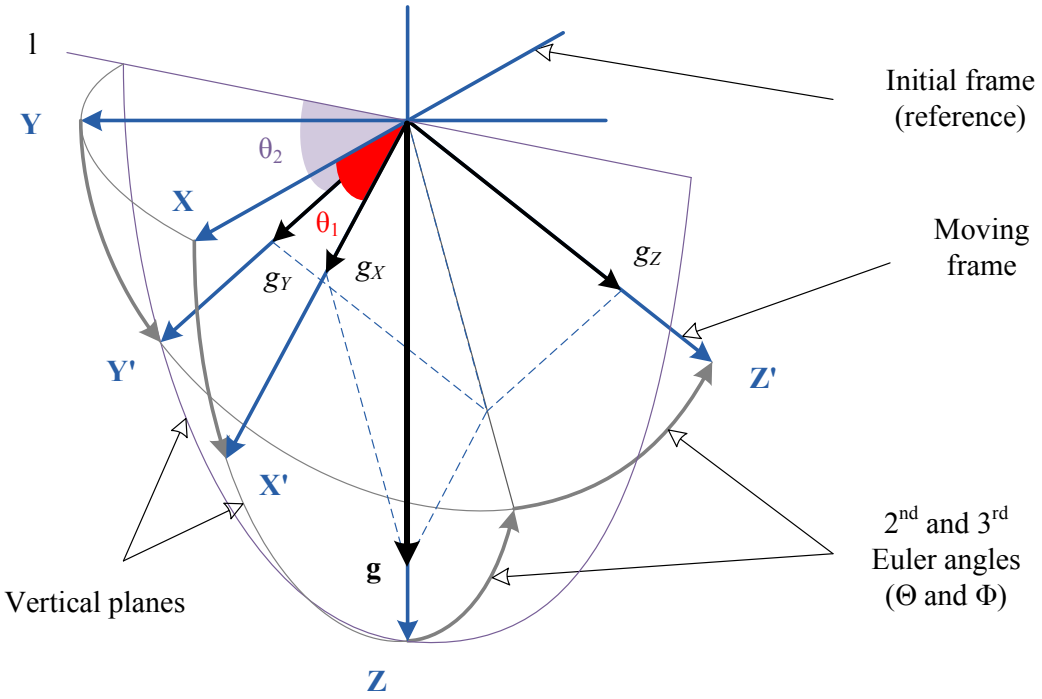

Figure 2.8: Calculation of the tilt when using the non-Euler angles

2.3 Major Challenges and Prevailing Solutions

2.3.1 Limitations of Digital Accelerometers

Both analog and digital accelerometers are commonly utilized for measuring the tilt angles. Because of the convenience and the EMI immunity, the digital accelerometers are good choices in many applications. However, this type of the acceleration sensor has certain limitations.

The limitations of the digital accelerometers are due to the on-chip analog to digital converters (ADCs). The on-chip ADCs commonly have limited data rates (e.g., 400–800 Hz) and limited data resolutions (e.g., 8–16 bits). In certain orientations, the limitation of the resolution could have a significant effect on the measurement accuracy because the tilt angles are calculated by non-linear functions [27]. On the other hand, the built-in ADCs generally have very few conversion modes, without an external trigger. This means that if the sensor

data need to be synchronized with an external clock source [20], the precise timing may not be guaranteed. Another problem is the digital switching noise in analog units (inside the MEMS) caused by sharing power and ground with digital units on a common substrate [35]. Figure 2.9 demonstrates the effects in a digital accelerometer which is similar to a mixed-mode IC. Because the connection wires have resistances ($2 \times R_{wire}$), any fast transient in the digital signals will cause a ripple in both common power source and ground point of the MEMS. In addition, there is a coupling effect between the digital and analog units. Thus, the sensitive portions in the analog units may be disturbed, and therefore the error could be generated.

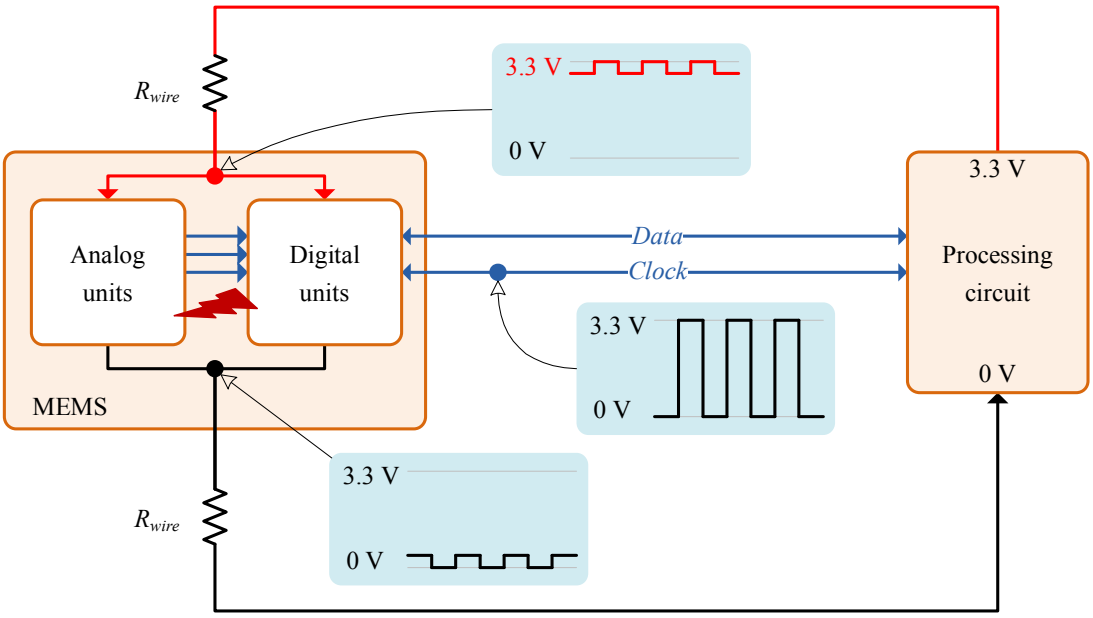

Figure 2.9: Influence of digital switching noise and crosstalk in digital accelerometers

2.3.2 Advantages and Drawbacks of Analog Sensors

When using the analog accelerometers, the mentioned above drawbacks of the digital accelerometers can be solved by adding an external ADC. The performance of the external ADCs is chosen to satisfy requirements of each application. Although

the intrinsic noise of the accelerometers itself could reduce the effective resolution of the output data, this should be less a problem when more advanced sensors are used. This type of the accelerometer also has another advantage that is to allow processing the output signals in analog form [6]. In this case, the response speed can be maximized and the tilt can be determined without any quantization error. However, single-ended signals are very sensitive to electromagnetic interference presents on connection wires [42]. Therefore, EMI suppression is important if we want to take the full advantage of the analog accelerometers.

EMI can be reduced by many methods. Some common solutions are introduced in [46]. One of the simplest methods of EMI reduction is using filters. However, the filters always cause time delay, and therefore limit the bandwidth of the output signals. Figure 2.10 demonstrates an example in which the external noise in sensor signals (three upper graphs) causes significant errors in the unfiltered output angle (fourth graph). Meanwhile, when a digital filter is used, the disturbance is almost rejected (last graph). However, the required sample for filtering is up to 200 when using a moving average filter. This could cause a remarkable time delay and should be avoided in many cases. Other methods are using shielded cables, shielding system, and preprocessors. They can isolate the analog circuits from the external EMI or convert the signals to other forms before transmitting. However, these methods are not suitable when the installment space must be minimized, as in [20].

2.3.3 Limitations of the Measurement Method

Tilt measurement with accelerometers is based on a vital assumption that is the sensors are static or quasi-static. When there is no movement, the accelerometer can exactly measure three components (g_X, g_Y, and g_Z) of the gravitational vector. In actual, movement and vibration could appear; the magnitude and orientation of these motions are represented by a linear acceleration vector ($\mathbf{a}$). Thus, the accelerometer readings are three components of $\mathbf{F}$ which is the sum of $\mathbf{g}$ and $\mathbf{a}$, as depicted in Fig. 2.11. Consequently, components of $\mathbf{g}$ and those of $\mathbf{F}$ are different. In other words, using accelerometer readings to compute the tilt

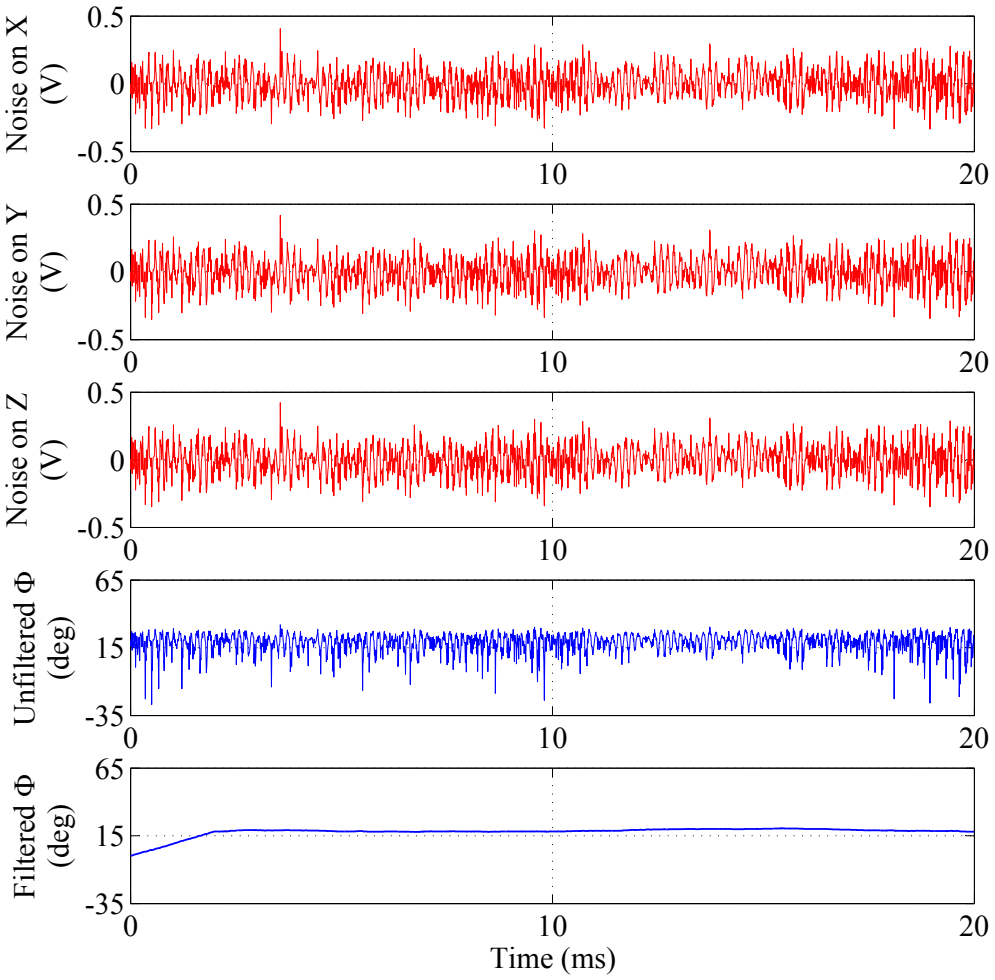

Figure 2.10: External noise and the effects on the computed tilt angles

angles could not be precise under the dynamic conditions. Hence, there is a need for special algorithms, additional sensors, or both of them.

In medical applications, the use of special algorithms and additional sensors for tilt measurement can be found in many studies [8]. Höller et al. proposed a horizon stabilization device that uses a triaxial accelerometer mounted on the tip of a flexible endoscope [19, 20]. They also proposed an algorithm to reduce shock-based error [18]. However, their algorithm quantifies the linear acceleration based on a comparison between magnitude of $\mathbf{F}$ and $\mathbf{g}$ without their direction, which is not sufficient [7]. Figure 2.12 illustrates a context when this algorithm cannot

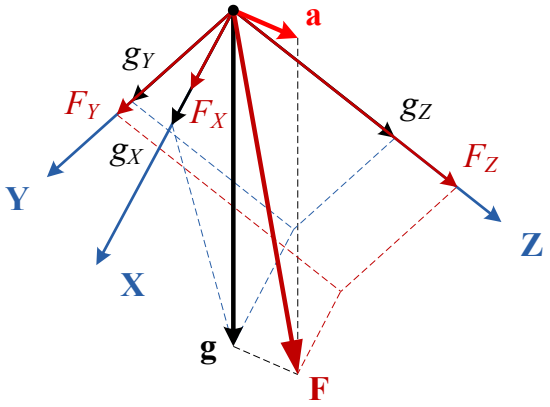

Figure 2.11: Differences between the gravitational components and the accelerometer readings when the linear acceleration is nonzero

distinguish two values of Φ. The problem is clearly depicted in Figure 2.12(b) in which $\mathbf{F}$ is different from $\mathbf{g}$ while $|\mathbf{F}|$ completely equals $|\mathbf{g}|$. In this case, although the sensor is aligned horizontally, its readings are same as the sensor data in Figure 2.12(a), when $\Phi = -30$ deg. Another study of endoscopic horizon stabilization was conducted by Warren et al. [47] in which the algorithm is based on that of Höller et al. Hence, both studies could have a same limitation.

Angle measurement using accelerometer and gyroscope is common in medical applications. Luinge et al. examined tilt angle measurements of the human body [31] and improved the method by adding a triaxial gyroscope [29]. Their method requires some assumptions, which could limit the application. In some studies, gyroscopes and accelerometers are used to measure the joint angles of the human body [12, 48]. However, the calculations in 2D models are different from those in 3D models. The fundamentals of the combination among an accelerometer, a gyroscope, and a Kalman filter can be found in [30]. However, the method is still limited to stationary or nearly stationary subjects. In general, measuring the tilt angles in the static or nearly static state is simple. Under the influence of motion, estimating the tilt angles is still a challenge. Moreover, reducing the size of the sensors and hardware is an important requirement for many medical devices.

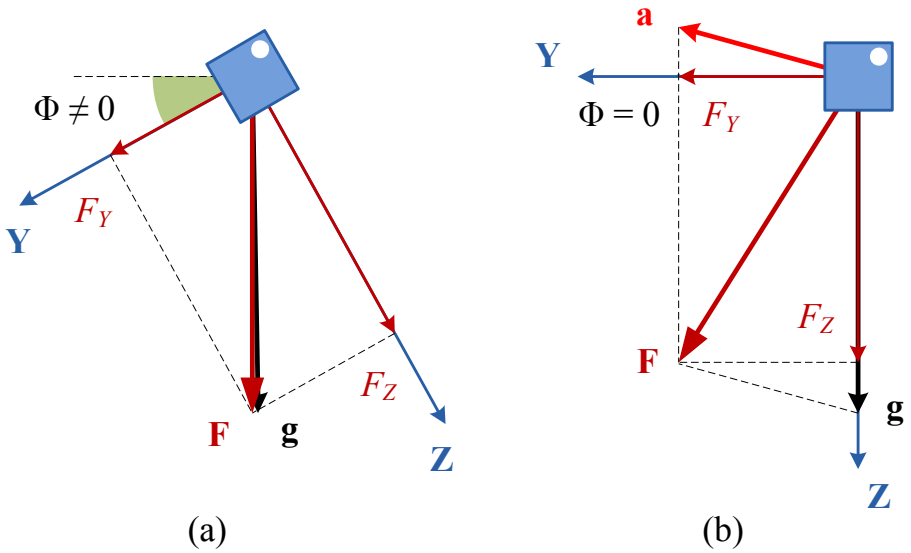

Figure 2.12: Quantifying the linear acceleration by comparing magnitude of **F** and **g**: (a) there is no confusion and (b) appearance of the error

2.4 Conclusion

In this chapter, the author has presented the fundamentals of tilt measurement, including rotation and mathematical representation, tilt definition and angle calculations, and the common limitations of the measurement technique that uses the inertial sensors. Simultaneously, many related studies have been reviewed to complement a panoramic view of the background. The concepts, terminologies, and equations in this chapter are very important for the subsequent chapters.

Chapter 3

EMI Reduction: in Measuring the Pitch Angle

This chapter presents the first study on interference reduction in measuring the tilt angles with analog accelerometers. First, the sensor is mounted on a special orientation which is defined by a rotation matrix. After that, new calculation formulas were built from the rotation sequence. This allows computing the pitch angle from the differential voltage between sensor signals to avoid the influence of the common-mode interference. Both simulation and experimental results confirmed that the pitch angle can be immune to the external noise. Hence, by using the proposed method, one tilt angle can be precisely measured without the need for shielded cables, filters, and preprocessors [9].

3.1 Introduction

The objective of this study is to improve the EMI immunity of the pitch angle, the second rotation in the yaw-pitch-roll order Euler angles. First and foremost, a new mounting orientation for the analog accelerometer is defined based on a so-called pitch-improved rotation matrix. After that, the corresponding calculation formulas are built. In the new equations, the pitch angle is computed from the differential voltage between sensor outputs, whereas the roll angle is still

calculated from single-ended values. This means that the pitch angle is not dependent on the common-mode interference which disturbs all sensor outputs identically. All external noise tends to induce only the common-mode signal on the lines while the same connections minimize differential voltage due to the interference [21].

The proposed method was examined by simulations and confirmed by experiments. In simulations, the author theoretically verified the new calculation method and its capability to reduce the interference. The results showed that the pitch angle can be precisely calculated under the disturbance of external noise. The output angles and noise intensity are almost independent. On the other hand, there is no improvement in roll angle, in comparison to conventional method. The experimental results showed that the power of the external noise can be reduced up to 165 times (about 22 dB) and the angle error in the pitch angle can be reduced up to 20 times in average.

3.2 Proposed Method

3.2.1 New Mounting Orientation

The new sensor mounting orientation is defined based on the pitch-improved rotation matrix, R_{Θ}. This matrix is built up from two elemental rotations: the first one rotates the sensor frame about the X-axis by $\alpha = 45$ deg and the second one rotates the sensor about the Z-axis by $\gamma = 45$ deg. After these rotations, the old sensor frame that is XYZ-frame becomes xyz-frame, as demonstrated in Figure 3.1. It should be noted that the tilt angles are not dependent on the sensor mounting method because they actually represent the orientation of the measured object. When changing the mounting orientation of the sensor, the tilt angles are not affected; however, the calculation algorithm must be altered.

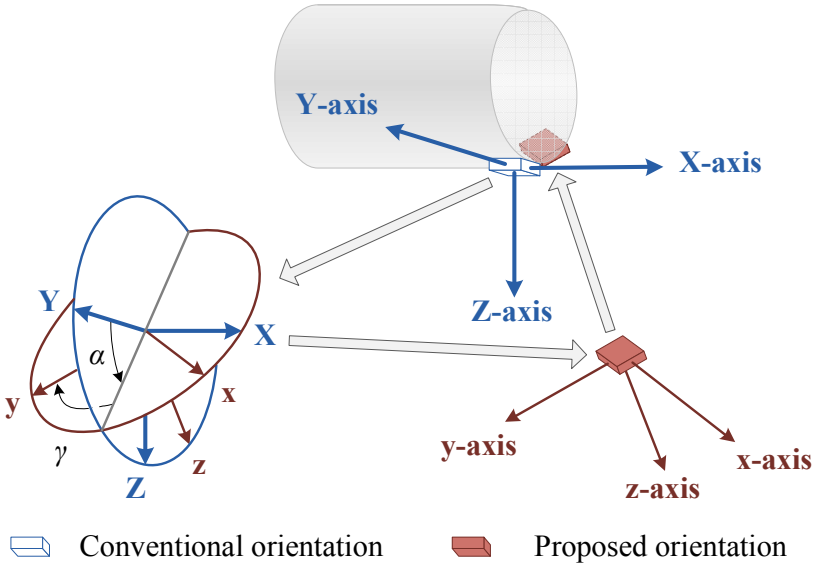

Figure 3.1: The definition of the proposed orientation in measuring the pitch angle

3.2.2 New Calculation Formulas

New calculation formulas are built based on the rotation matrix. First, because the sensor frame is rotated about the axes of itself, these rotations are passive and intrinsic. Hence, two elemental rotations expressed in Eqn. (2.6) and Eqn. (2.8) are combined to calculate R_Θ in Eqn. (3.1). After substituting the given values of α and γ, all elements of R_Θ are identified in Eqn. (3.2). This matrix rotates the sensor frame by Eqn. (3.3) in which g_x, g_y, and g_z are three components of the gravitational vector on the new sensor frame (xyz-frame). On the basis of Eqn. (3.3) and Eqn. (2.11), the relation between the gravitational components and the tilt angles is determined in Eqn. (3.4).

$$
\begin{aligned}
R_\Theta &= R_Z(\gamma)R_X(\alpha) \\
&= \begin{bmatrix} \cos\gamma & \cos\alpha\sin\gamma & \sin\alpha\sin\gamma \\ -\sin\gamma & \cos\alpha\cos\gamma & \cos\gamma\sin\alpha \\ 0 & -\sin\alpha & \cos\alpha \end{bmatrix}
\end{aligned} \tag{3.1}
$$

$$R_\Theta = \frac{1}{2}\begin{bmatrix} \sqrt{2} & 1 & 1 \\ -\sqrt{2} & 1 & 1 \\ 0 & -\sqrt{2} & \sqrt{2} \end{bmatrix} \tag{3.2}$$

$$\frac{1}{|\mathbf{g}|}\begin{bmatrix} g_x \\ g_y \\ g_z \end{bmatrix} = R_\Theta \frac{1}{|\mathbf{g}|}\begin{bmatrix} g_X \\ g_Y \\ g_Z \end{bmatrix} \tag{3.3}$$

$$\frac{1}{|\mathbf{g}|}\begin{bmatrix} g_x \\ g_y \\ g_z \end{bmatrix} = \frac{1}{2}\begin{bmatrix} -\sqrt{2}\sin\Theta + \cos\Theta\sin\Phi + \cos\Theta\cos\Phi \\ \sqrt{2}\sin\Theta + \cos\Theta\sin\Phi + \cos\Theta\cos\Phi \\ -\sqrt{2}\cos\Theta\sin\Phi + \sqrt{2}\cos\Theta\cos\Phi \end{bmatrix} \tag{3.4}$$

The tilt angles can be calculated by combining the sub-equations in Eqn. (3.4). First, these sub-equations are numbered 1–3 from top to bottom. Then, by subtracting two sides of Eqn. (3.4.1) from the corresponding sides of Eqn. (3.4.2), $\sin\Theta$ can be determined by Eqn. (3.5). Similarly, Eqn. (3.6) and Eqn. (3.7) are the results of the combination among three sub-equations in two different ways. Thus, $\tan\Phi$ can be calculated by Eqn. (3.8).

$$\sin\Theta = \frac{\sqrt{2}}{2}\frac{(g_y - g_x)}{|\mathbf{g}|} \tag{3.5}$$

$$\frac{(g_x + g_y - \sqrt{2}g_z)}{|\mathbf{g}|} = 2\cos\Theta\sin\Phi \tag{3.6}$$

$$\frac{(g_x + g_y + \sqrt{2}g_z)}{|\mathbf{g}|} = 2\cos\Theta\cos\Phi \tag{3.7}$$

$$\tan\Phi = \frac{g_x + g_y - \sqrt{2}g_z}{g_x + g_y + \sqrt{2}g_z} \tag{3.8}$$

Finally, the tilt angles can be computed from the output voltages (U_x, U_y, and U_z) of the sensor by Eqn. (3.9) and Eqn. (3.10) because these voltages are directly proportional to the gravitational components.

$$\sin\Theta = \frac{\sqrt{2}}{2}\frac{(U_y - U_x)}{\sqrt{U_x^2 + U_y^2 + U_z^2}} \tag{3.9}$$

$$\tan \Phi = \frac{U_x + U_y - \sqrt{2}U_z}{U_x + U_y + \sqrt{2}U_z} \tag{3.10}$$

3.2.3 Interference Cancellation Mechanism

First, the effects of the external noise are considered. Because of the disturbance on the transmission lines, the measured voltages (U_{mx}, U_{my}, and U_{mz}) are the sum of the sensor signals and external noise (n_x, n_y, and n_z), respectively. By using well-balanced lines for signal connections, we can assume that n_x, n_y, and n_z are identical ($n_x = n_y = n_z = n$). In other words, they are common-mode interference. This assumption is reasonable in actual condition [21].

Second, in practical measurement, all voltages in Eqn. (3.9) and Eqn. (3.10) must be substituted by the measured values. Although the signals are affected by noise, the value of U defined in Eqn. (3.11) can be restored from U_m defined in Eqn. (3.12). Ideally, U is a constant and equal to the sensor sensitivity. However, because of the sensor error, the magnitude of U slowly changes during the operation. Hence, the value U can be recovered by filtering U_m with a low cutoff frequency. This filter allows updating the changes in U (caused by the sensor error) and rejecting the disturbance of EMI. It should be noted that the above filter absolutely does not affect the response speed of the measurement system.

$$U = \sqrt{U_x^2 + U_y^2 + U_z^2} \tag{3.11}$$

$$U_m = \sqrt{U_{mx}^2 + U_{my}^2 + U_{mz}^2} \tag{3.12}$$

Finally, the tilt angles are calculated by Eqn. (3.13) and Eqn. (3.14). In Eqn. (3.13), the term of the external noise (n) is eliminated. This means that the result is not dependent on the external noise. In contrast, the roll angle is still disturbed by interference because the term of noise in Eqn. (3.14) affects the result. In other words, there is no improvement in the roll angle.

$$\Theta = \arcsin\left[\frac{\sqrt{2}}{2}\frac{(U_{my} - U_{mx})}{U_m}\right]$$

$$= \arcsin\left[\frac{\sqrt{2}}{2}\frac{(U_y - U_x)}{U}\right] \tag{3.13}$$

$$\Phi = \arctan 2\left[\left(U_{mx} + U_{my} - \sqrt{2}U_{mz}\right), \left(U_{mx} + U_{my} + \sqrt{2}U_{mz}\right)\right]$$

$$= \arctan 2\left\{\left[U_x + U_y - \sqrt{2}U_z + (2 - \sqrt{2})n\right], \left[U_x + U_y + \sqrt{2}U_z + (2 + \sqrt{2})n\right]\right\} \tag{3.14}$$

3.2.4 Calibration Process

In tilt measurement, both scale factor and zero-g level of the accelerometer should be calibrated. This calibration can significantly improve the measurement accuracy. In this study, the calibration was performed based on [36]. Here, a more precise calibration is also described, including the improvement of cross-axis interactions and any rotation of the sensor package on the circuit board. However, this process requires some specific orientations, which may not be available in practical implement.

3.3 Simulations

3.3.1 Simulation Setup

Simulations were performed to examine the new calculation algorithm. In Fig. 3.2, the input tilt angles (Θ_O and Φ_O) are used to create the sensor outputs of two virtual accelerometers. The first sensor is on the conventional orientation, whereas

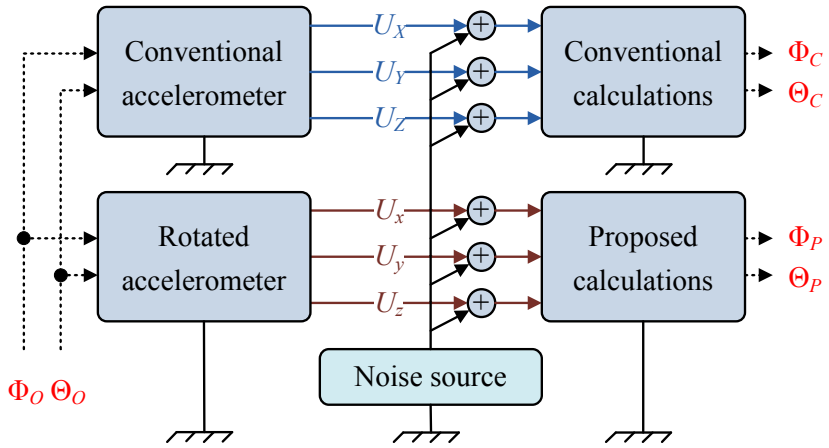

Figure 3.2: Main components of the simulation model

the second one is on the proposed orientation. The sensitivity of both sensors is 1 V/g. A white Gaussian common-mode noise whose RMS value is 50–100 mV is added to all sensor signals. This high intensity is chosen to demonstrate the capability of the proposed algorithm to reduce the external noise. The conventional method [37] calculates Θ_C and Φ_C, whereas the proposed method computes Θ_P and Φ_P. All results are compared to the original angles for evaluation. Because the roll angle cannot be determined by accelerometer when $\Theta_O = \pm 90$ deg, all simulations are performed with the range of Θ_O is -89 to $+89$ deg and Φ_O is -180 to $+180$ deg.

3.3.2 Simulation Results

Angles errors were used as the major criterion for evaluating. Hence, instead of showing the computed angles, the author reported the differences between each angle and the corresponding original value.

The simulation results are shown in following figures. In Fig. 3.3, all differences between the computed angles and the original ones are equal to zero. This means that, theoretically, there is no limitation in the formulas of the proposed method when being compared with those of the conventional method. In the next test, when the RMS value of the external noise is 50 mV, Fig. 3.4(a) shows that

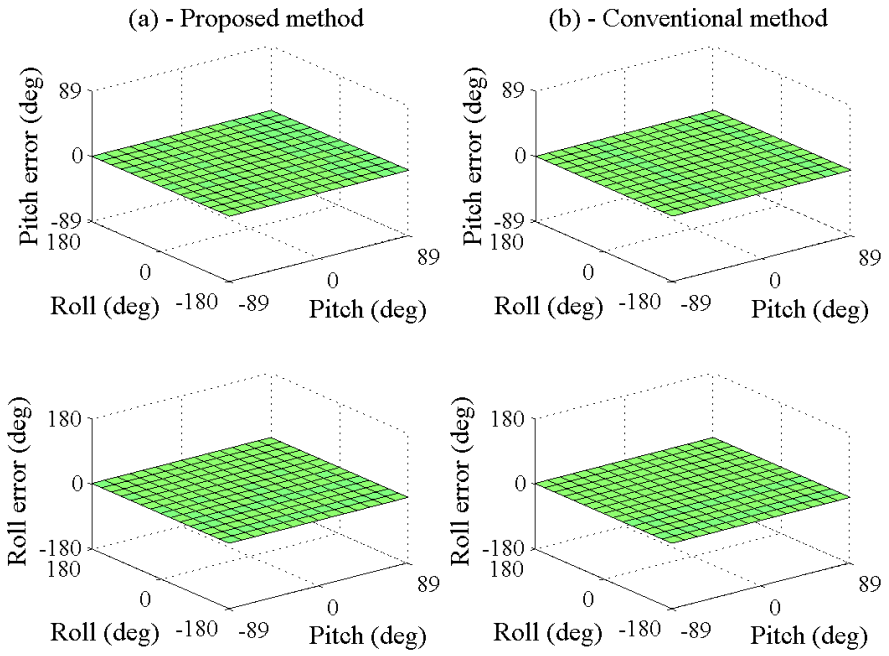

Figure 3.3: Precise results of both methods when there is no noise

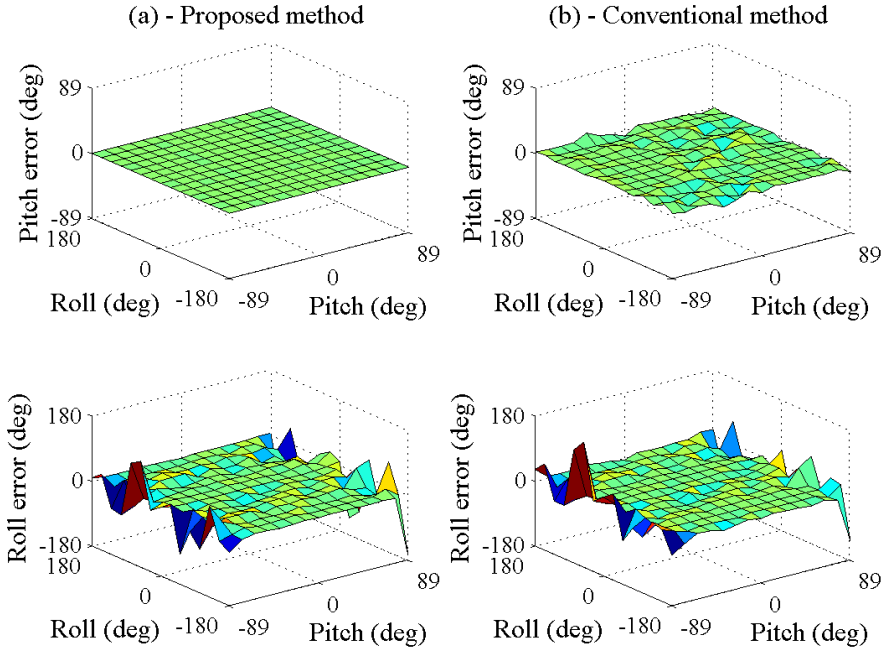

Figure 3.4: Angle errors under the effects of the external noise: $n_{RMS} = 50$ mV

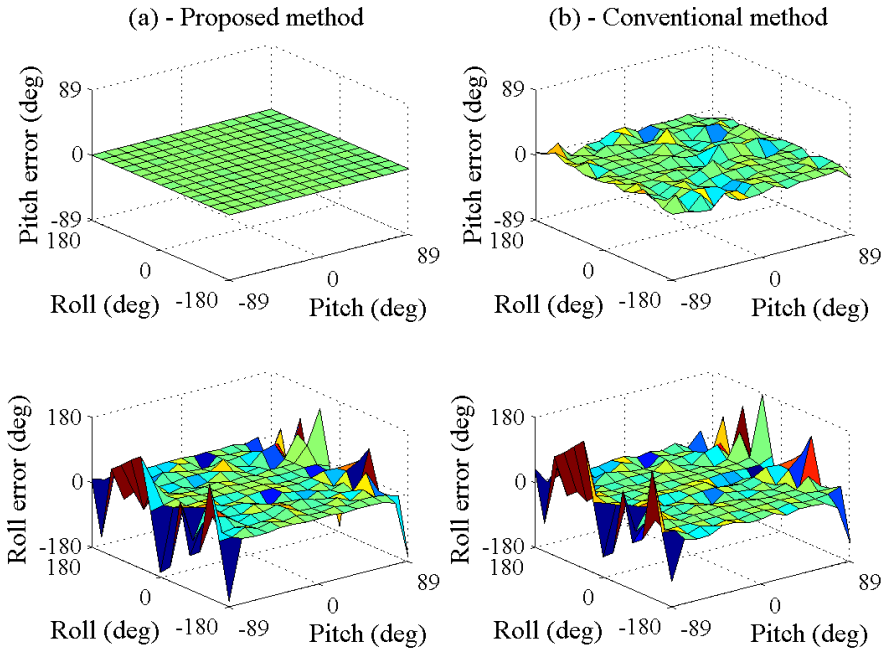

Figure 3.5: Angle errors under the effects of the external noise: $n_{RMS} = 100$ mV

the error of the pitch angle of the proposed method always equals to zero. Thus, this angle does not depend on the common-mode noise. In contrast, there is no improvement in the roll angle. The roll angle and both angles of the conventional method in Fig. 3.4(b) change randomly. When the RMS value of external noise increases to 100 mV, the results are shown in Fig. 3.5. The differences between Fig. 3.4 and Fig. 3.5 confirm that stronger interference causes larger errors in Φ_P, Θ_C, and Φ_C. These figures also point out the dependences of angle errors on the increment of the pitch angle.

Therefore, in the last evaluation, the mean value and standard deviation of the angle errors in some specific ranges of the pitch angle are considered. In this test, both input angles were changed; the increment step is 1 deg. The ranges of the pitch angle increase from -89 to $+89$ deg. The results are shown in Table 3.1; then differences between them are illustrated in Fig. 3.6 and Fig. 3.7. The pitch angle of the proposed method has no error. Meanwhile, the pitch angle computed by the conventional method has significant deviations (SD = 5.2–5.8 deg). When the slop of the sensor (absolute value of the pitch angle) increases, the variability

Table 3.1: Dependence of angle errors (mean and SD) on the range of the pitch angle

Range No.	Values of Θ_O (deg)	Mean (and SD) of errors (deg)			
		In Θ_P	In Θ_C	In Φ_P	In Φ_C
1	−89 to −80	0 (0)	3.4 (5.2)	−0.4 (68.6)	0 (64.2)
2	−80 to −60	0 (0)	0.9 (5.5)	0.1 (28.9)	−0.1 (23.7)
3	−60 to −30	0 (0)	0.3 (5.6)	−0.1 (10.7)	−0.1 (8.6)
4	−30 to 30	0 (0)	0 (5.8)	0 (7.5)	0 (6.1)
5	30 to 60	0 (0)	−0.2 (5.6)	0.2 (10.7)	0.1 (8.7)
6	60 to 80	0 (0)	−1.0 (5.5)	−0.2 (28.1)	0.3 (22.6)
7	80 to 89	0 (0)	−3.3 (5.3)	1.0 (68.6)	0.1 (63.6)

of the SD is almost small while the mean values have a asymmetric change. This means that when filtering the pitch angle of the conventional method, the use of the average value could not be a good solution. On the other hand, the errors in the roll angles of both methods are large. They also strongly increase when the absolute value of the pitch angle increases. When pitch is close to ±90 deg, the roll angles of both methods are no longer reliable, although the mean values of the errors are close to zero. Therefore, when comparing the angle errors of the two methods, the disparity between the standard deviations is more important than the difference of the mean values.

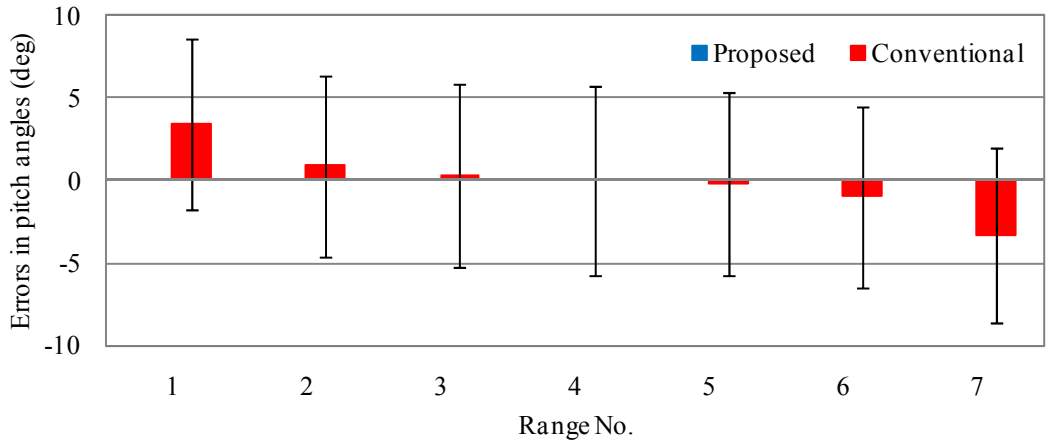

Figure 3.6: Errors in the computed pitch angles in different ranges of the original pitch angle

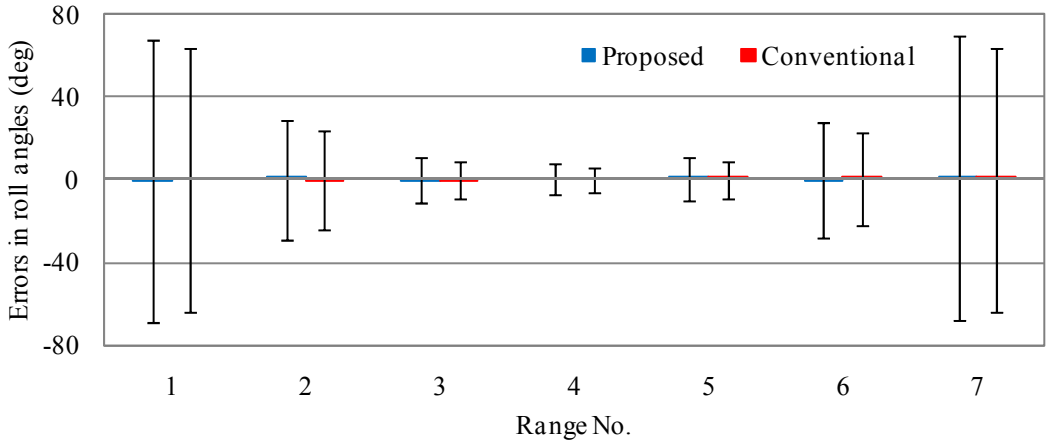

Figure 3.7: Errors in the computed roll angles in different ranges of the original pitch angle

3.4 Experiments

3.4.1 Experimental Setup

All experiments are performed with two triaxial analog accelerometers attached on a rotation frame. First of all, the type of the main sensors is chosen based on

Table 3.2: Specifications of the chosen accelerometer, KXR94-2050

Parameters	Units and values			
	Units	Min	Typ.	Max
Zero-g offset	V	1.6	1.65	1.7
Sensitivity	mV/g	647	660	673
Non-linearity	% of FS		0.1	
Cross axis sensitivity	%		2	
Bandwidth (-3 dB)	Hz	640	800	960
Noise density	$\mu g/\sqrt{\text{Hz}}$		45	
Supply voltage	V	2.5	3.3	5.25
Analog output resistance	kΩ	24	32	40

the noise density. Because the objective of the all test is to evaluate the intensity of the external noise and the EMI immunity of the new method, the intrinsic noise of the sensors should be minimized. In other words, lower noise density the sensors have, more precise results we can achieve. Hence, the author chose KXR94-2050 [2], a common type of analog accelerometers of Kionix, Inc. The main specifications of this sensor are given in Table 3.2. In comparison with noise densities of other accelerometers, that can be found easily on the market, such as 150 $\mu g/\sqrt{\text{Hz}}$ of ADXL335 [1], 350 $\mu g/\sqrt{\text{Hz}}$ of MMA7361LC [4], or 100 $\mu g/\sqrt{\text{Hz}}$ of KXSC7-2050 [3], the intrinsic noise of the chosen type (45 $\mu g/\sqrt{\text{Hz}}$) is significantly smaller. Second, two sensors were attached onto the measurement system: one of them was mounted by conventional method while the other was attached on the proposed orientation with an adapter, as shown in Fig. 3.8.

Three-core twisted cables (1 m in length) are used to connect the sensors and measuring circuits. Each cable is twisted from three enameled wires, as in Fig. 3.9. Because the diameter of each core is small (0.25 mm), the twisted cables are thin and flexible. The sensitivity of the sensor is low (660 mV/g at 3.3 V power

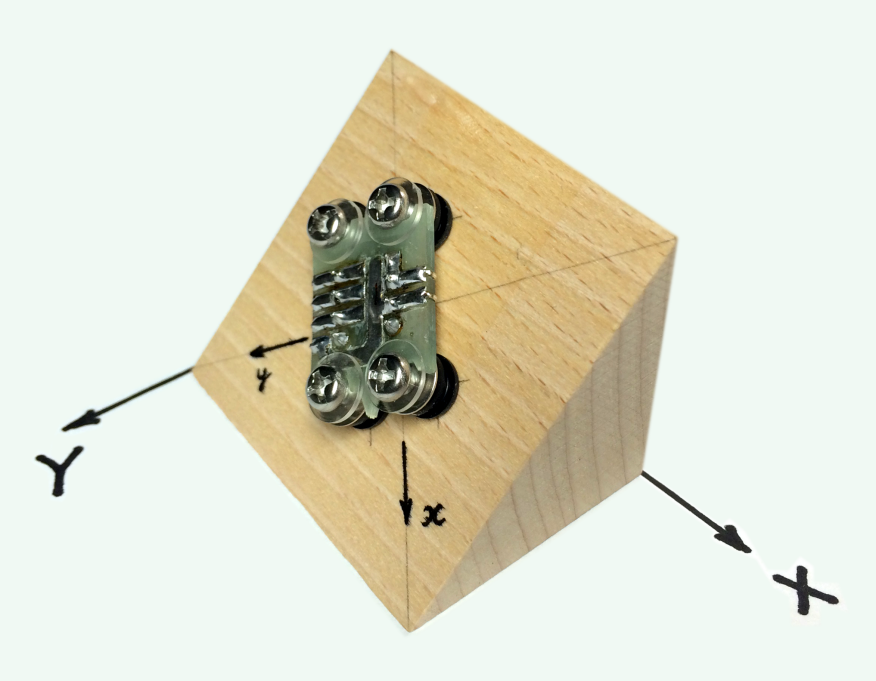

Figure 3.8: Adapter for altering the attachment of the accelerometer

supply); therefore, all signals are amplified six times before processing. Hence, the effective sensitivity of the accelerometer is 3.96 V/g.

All tests were conducted in the actual environment. The external noise is the summation of unwanted or disturbing energy from all natural and man-made sources. Both bandwidth and power density of the noise are uncontrollable and unknown; however, its RMS value is measured and shown in the first experiment. The author performed the measurements under the stationary states. The rotation frame was fixed at the desire positions before each measurement to minimize the disturbance of motion. The signals are captured by a digital oscilloscope and then the data are processed by the computer software.

3.4.2 Experimental Results

First, the similarity of the external noise presents in single-ended signals is examined. The AC coupling mode was used to measure noise only. Figure 3.10 shows

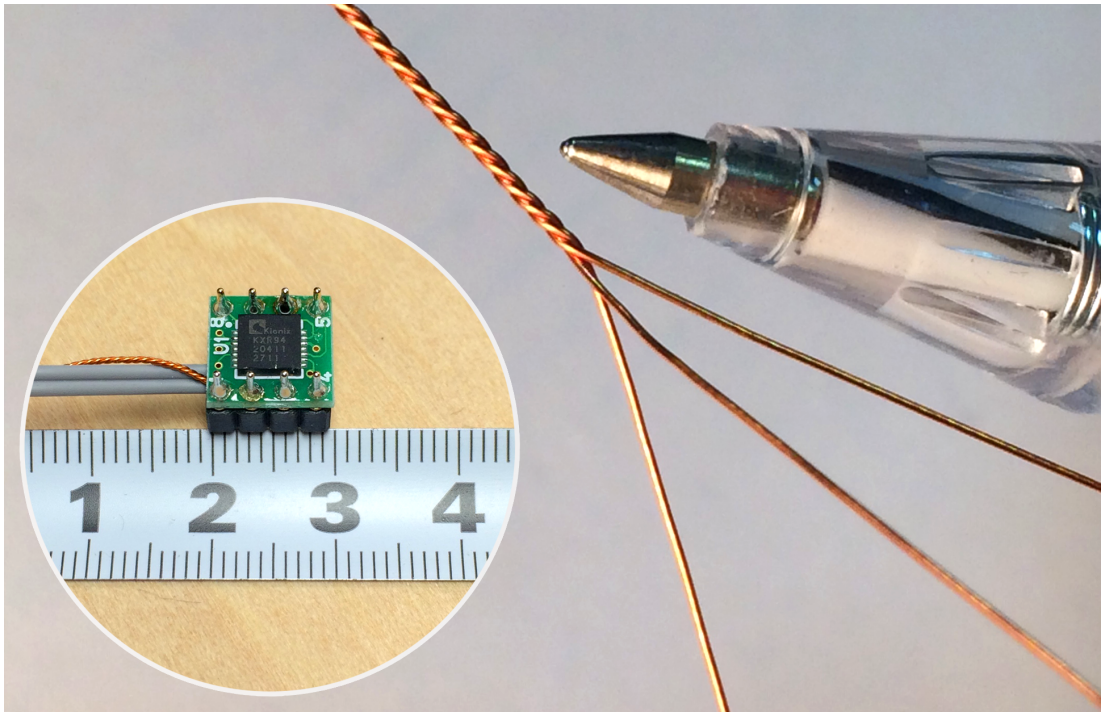

Figure 3.9: Analog accelerometer and the three-core twisted cable

the measured signals on the y-axis, x-axis, and the difference between them.

The instantaneous variability of two first charts is similar. The RMS value of noise on the y-axis (113.1 mV) is almost equal to that on the x-axis (111.7 mV). In addition, the RMS value of the differential voltage between the y- and x-axes is 8.8 mV. This means that the power of the noise is reduced about 165 times (22 dB) when working with differential voltage. This result confirms the assumption in Sec. 3.2.3.

Second, the efficiency of EMI reduction is demonstrated in Fig. 3.11. Here, the true value of the pitch angle is -25 deg and roll angle is -100 deg. The pitch angle of the proposed method is stable, whereas that of the conventional method fluctuates over time. On the other hand, both roll angles are affected by noise; their mean values are different.

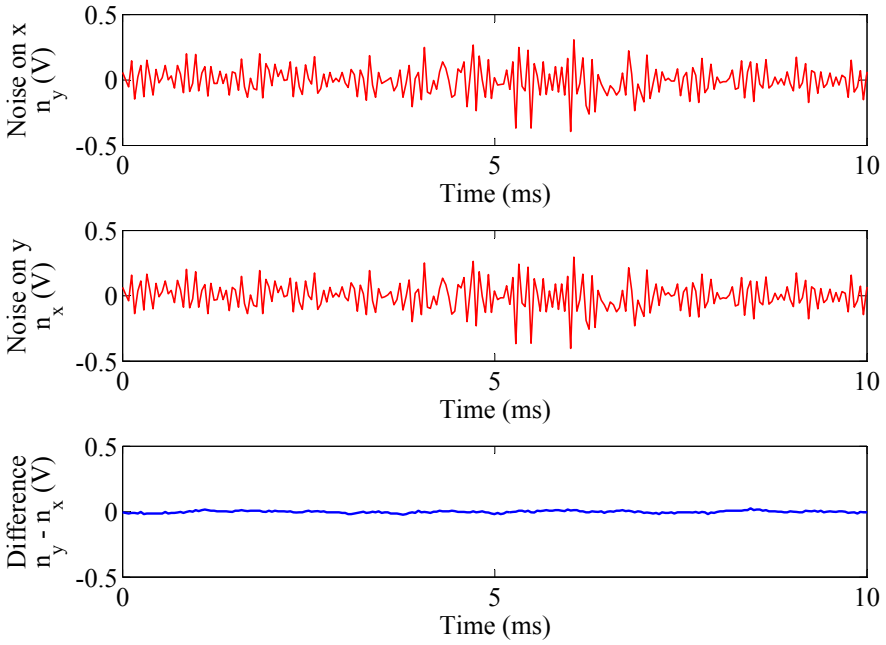

Figure 3.10: Noises in the connection wires and the difference between them

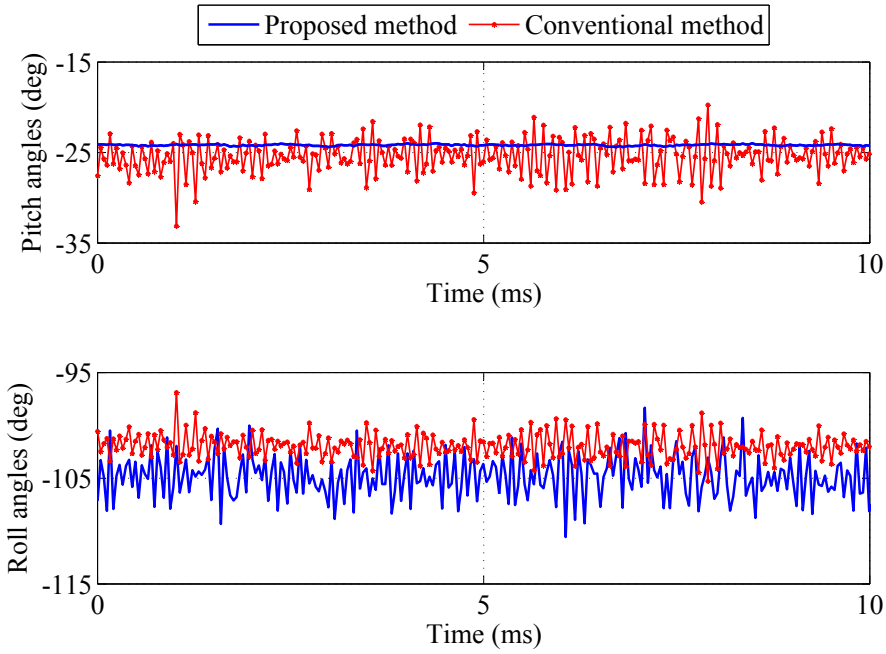

Figure 3.11: Stability of the pitch angle computed by proposed method and the fluctuations of the remaining angles

Table 3.3: Errors (mean and SD) in computed angles on some specific orientations

Test No.	True angles (deg)		Mean (and SD) of errors (deg)			
	Θ_O	Φ_O	In Θ_P	In Θ_C	In Φ_P	In Φ_C
1	-80	50	2.1 (0.5)	-1.9 (2.1)	-13.3 (8.2)	-19.0 (5.6)
2	-70	-90	1.7 (0.3)	-0.3 (2.7)	-11.8 (6.9)	-17.7 (3.6)
3	-30	-170	0.9 (0.1)	-0.2 (1.8)	-7.0 (0.3)	-4.1 (1.4)
4	-10	30	0.3 (0.1)	0.5 (1.3)	-1.4 (1.0)	3.9 (0.5)
5	0	0	0.2 (0.1)	0.1 (1.1)	0.5 (0.3)	0.2 (1.1)
6	10	45	0.1 (0.1)	0.7 (2.1)	1.2 (1.9)	1.1 (0.1)
7	30	160	-0.5 (0.1)	1.1 (0.9)	-1.8 (1.9)	6.3 (0.1)
8	70	-50	-1.3 (0.3)	1.4 (0.5)	4.4 (4.9)	11 (5.0)
9	80	-20	-2.3 (0.5)	2.3 (1.2)	10.5 (3.3)	16.9 (9.5)

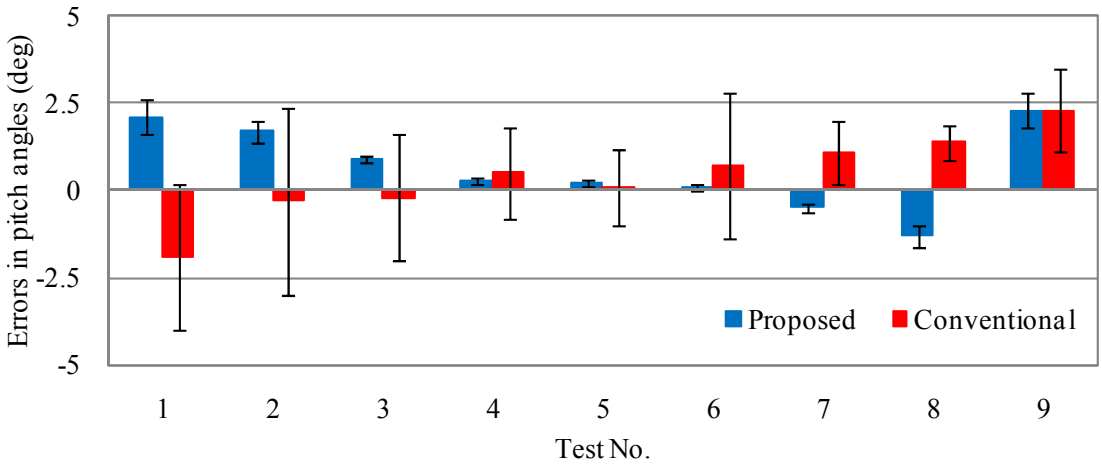

Figure 3.12: Differences between the errors in the computed pitch angles

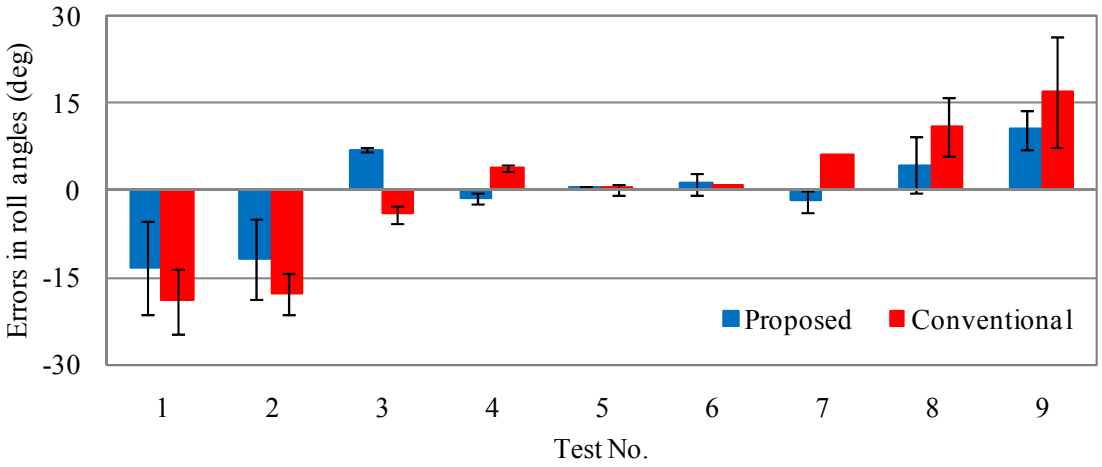

Figure 3.13: Differences between the errors in the computed roll angles

Finally, the author quantified the EMI immunity of the pitch angle on some specific orientations. The signals were sampled 250 times in 10 ms for calculating the angles and errors. After that, the mean value and standard deviation of the angle errors are computed; the result is rounded to one decimal place and shown on Table 3.3. Consequently, the comparisons between the errors of each angle are clearly depicted in Fig. 3.12 and Fig. 3.13. In the pitch angles, errors of Θ_P and Θ_C have the similar mean value. However, the variability of Θ_P is 2–20 times smaller than that of Θ_C. When the absolute value of Θ_O is high, mean values of errors increase, while the difference between the standard deviations decreases.

Hence, the improvement in the pitch angle is strongly depends on the slop of the object. In the roll angles, the higher absolute value of Θ_O is, the larger errors in the computed results of both methods occur. It should be noted that the graphs shown in Figs. 3.12 and 3.13 are the angles measured in a few individual orientations. Therefore, the trend of the data in these figures is not clear and changed irregularly.

3.5 Discussion

Compared with the conventional method, the proposed method has notable advantages. The conventional method calculates the tilt angles based on the absolute voltages of single-ended signals, which are very sensitive to EMI. In contrast, the proposed method computes the pitch angle from the differential voltages. Therefore, the new method takes an advantage of the differential systems although the outputs of the sensor are still the single-ended signals.

A major drawback of the proposed method is misalignment when mounting the sensors. This problem causes systematic errors in the experimental result; the values can be estimated from the nonzero mean values.

3.6 Conclusion

In this chapter, a new method of interference reduction in tilt sensing with analog accelerometer has been presented. The new method is proposed based on mounting the accelerometer on a new orientation and developing new calculation formulas. The new formulas compute the pitch angle from the differential voltage which is immune to the external EMI. The measured data showed that by this way, the power of noise can be reduced up to 165 times (22 dB); the standard deviation of angle errors was reduced up to 20 times. Hence, this study can expand the applicability of analog accelerometers by changing the sensor mounting orientation only. Although only the pitch angle is improved, this can meet the requirements of many applications.

Chapter 4

EMI Reduction: in Measuring the Roll Angle

This chapter presents a development and validation of the new interference reduction method for measuring the roll angle with accelerometers. The main idea of the study in this chapter is similar to that in the previous chapter: the roll angle can be measured with less noise if both sensor orientation and calculation formulas are changed by a suitable rotation matrix. The EMI immunity is due to the calculation formulas using differential voltages among sensor outputs. Once again, the advantage of the differential signaling technique is taken within the single-ended system. Moreover, the sensor calibration, simulation model, and experimental system of the study in this chapter have been upgraded to evaluate the new method more exactly. The results confirmed the notable efficiency without any additional hardware and software. This study could be useful for systems which require the roll angle at high speed and high resolution with minimum resources [10, 11].

4.1 Introduction

In this chapter, the EMI immunity of the roll angle, the third rotation in the yaw-pitch-roll order Euler angles, is improved by a new measurement method.

First, the author proposed a so-called roll-improved rotation matrix to define a new mounting orientation for the accelerometer. Then, the rotation matrix is used to convert the conventional calculation formulas. After this conversion, the roll angle is completely calculated from the differences of the voltages between the sensor outputs. Therefore, the computed value is immune to external EMI, which perturbs all signals identically.

In comparison with the research in the previous chapter, the major working processes of the study in this chapter are upgraded. In the measurement method, a complete calibration process, including sensor calibration and orientation adjustment is introduced. In the simulation model, the differential-mode noise sources are added. This increases the reality of the input data and the accuracy of the simulation results. In the experimental system, a dedicated DAQ module is used instead of the digital oscilloscope. This change allows capturing the signals at high resolution and high data rate.

The simulation and experiment results confirmed the efficiency of the new method. The noise power was reduced 230 times (23.6 dB) and the standard deviation of angle errors could be reduced 5–22.5 times. In addition, there is neither improvement nor significant degradation in the pitch angle in comparison with the conventional measurement method.

4.2 Proposed Method

4.2.1 Hardware System

The measurement system consists of three typical units, as shown in Fig. 4.1. The sensor unit is a three-axis analog accelerometer mounted on a small circuit; the mounting orientation is described in Sec. 4.2.2. The next unit includes a tiny paired cable for power supply and a three-core twisted cable for transmitting three sensor signals. Here, the twisted cable is used to minimize the differential-mode EMI. The processing unit has several functions: subtracting the zero-g bias voltage from the sensor outputs, then capturing the signals, and finally calculating

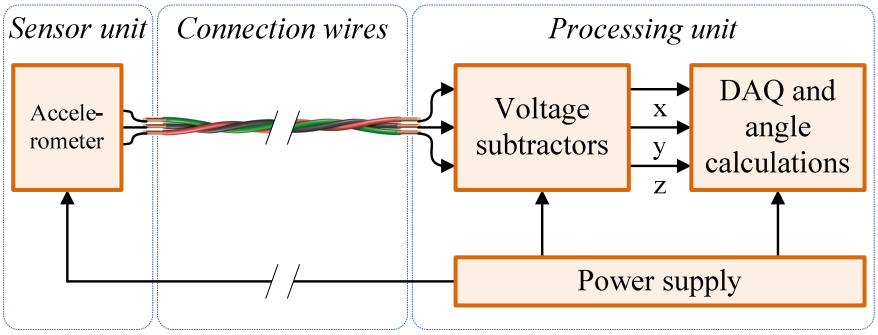

Figure 4.1: Three major units in the hardware system

the angles. The star grounding is used to avoid any unwanted errors caused by ground loops [17].

Regarding the device usage, the common types of electronic components and equipment were used. The accelerometer (KXR94-2050, Kionix) has a full scale of ± 2 g and a typical sensitivity of 660 mV/g. The twisted cable (1 m in length) is twisted from three tiny enameled wires (0.25 mm in diameter). In the processing circuit, instrumentation amplifiers (INA128, Texas Instruments) are used for voltage subtraction, while a compact hardware module (NI cDAQ-9178 and NI 9215, National Instruments) is utilized for data acquisition. Because the dynamic range of the DAQ device is higher than sensor sensitivity, the gain of INA128 is set to a value of 6.0. The angle calculations are performed by LabVIEW on a personal computer.

4.2.2 New Mounting Orientation

Figure 4.2 illustrates the new mounting orientation for the accelerometer. This orientation is defined by the roll-improved rotation matrix that rotates the XYZ-frame about the Z-axis by γ first, and then about the new X-axis by α. The optimized values of γ and α are proposed in Eqn. (4.1) to minimize the complexity of the formulas, and furthermore improve the EMI immunity. Both γ and α have negative values because they represent the rotations which appear clockwise when

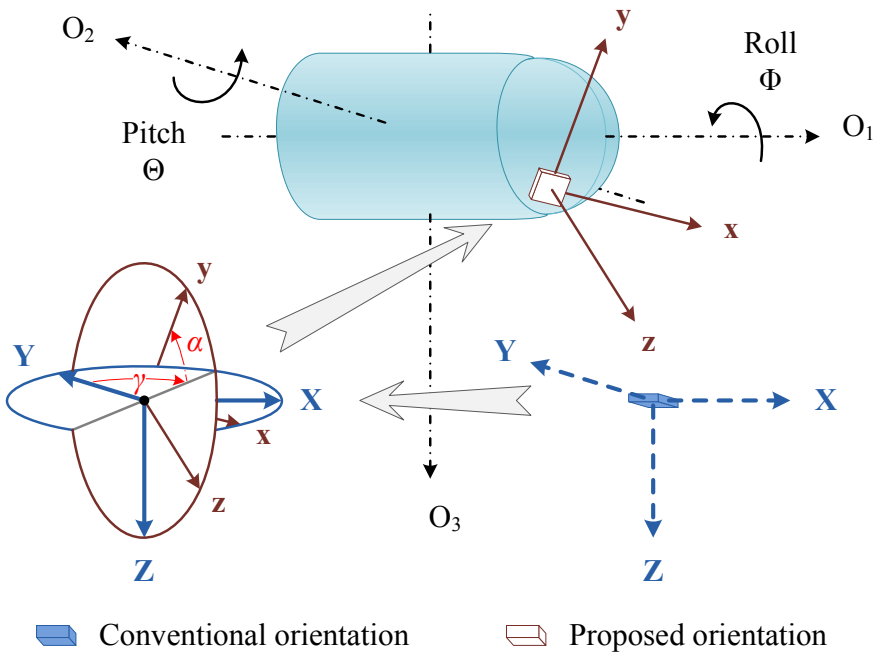

Figure 4.2: The definition of the proposed orientation in measuring the roll angle

observing in the negative direction of the axes.

$$\begin{bmatrix} \gamma \\ \alpha \end{bmatrix} = \begin{bmatrix} -\arctan\sqrt{2} \\ -\pi/4 \end{bmatrix} \tag{4.1}$$

The new orientation has distinctive features: O_1-, O_2-, and x-axes are co-planar; their plane and the bisector plane of the angle between y- and z-axes are parallel. In addition, three angles between O_1- and x-axes, O_1- and y-axes, O_1- and z-axes are simultaneously equal to $|\gamma|$.

4.2.3 New Calculation Formulas

The conventional formulas and the roll-improved rotation matrix were used to build the new formulas. First, two elemental rotation matrices expressed in Eqn. (2.6) and Eqn. (2.8) were combined to calculate R_Φ in Eqn. (4.2). After substituting the given values of γ and α, all elements of R_Φ are identified in Eqn. (4.3). This matrix rotates the sensor frame by Eqn. (4.4) in which g_x, g_y,

and g_z are three components of the gravitational vector on the new sensor frame (xyz-frame). Hence, the relation between the gravitational components and the tilt angles is determined in Eqn. (4.5).

$$R_\Phi = R_X(\alpha)R_Z(\gamma)$$

$$= \begin{bmatrix} \cos\gamma & \sin\gamma & 0 \\ -\cos\alpha\sin\gamma & \cos\alpha\cos\gamma & \sin\alpha \\ \sin\alpha\sin\gamma & -\cos\gamma\sin\alpha & \cos\alpha \end{bmatrix} \tag{4.2}$$

$$R_\Phi = \frac{\sqrt{6}}{6}\begin{bmatrix} \sqrt{2} & -2 & 0 \\ \sqrt{2} & 1 & -\sqrt{3} \\ \sqrt{2} & 1 & \sqrt{3} \end{bmatrix} \tag{4.3}$$

$$\frac{1}{|\mathbf{g}|}\begin{bmatrix} g_x \\ g_y \\ g_z \end{bmatrix} = R_\Phi \begin{bmatrix} -\sin\Phi \\ \cos\Theta\sin\Phi \\ \cos\Theta\cos\Phi \end{bmatrix} \tag{4.4}$$

$$\frac{1}{|\mathbf{g}|}\begin{bmatrix} g_x \\ g_y \\ g_z \end{bmatrix} = \frac{\sqrt{6}}{6}\begin{bmatrix} -\sqrt{2}\sin\Theta - 2\cos\Theta\sin\Phi \\ -\sqrt{2}\sin\Theta + \cos\Theta\sin\Phi - \sqrt{3}\cos\Theta\cos\Phi \\ -\sqrt{2}\sin\Theta + \cos\Theta\sin\Phi + \sqrt{3}\cos\Theta\cos\Phi \end{bmatrix} \tag{4.5}$$

The tilt angles can be calculated by combining the sub-equations in Eqn. (4.5). First, by adding or subtracting each side of a sub-equation from the corresponding sides of the others, some intermediate equations can be expressed in Eqn. (4.6), Eqn. (4.7), and Eqn. (4.8).

$$\frac{(g_z + g_y - 2g_x)}{|\mathbf{g}|} = \sqrt{6}\cos\Theta\sin\Phi \tag{4.6}$$

$$\frac{(g_z - g_y)}{|\mathbf{g}|} = \sqrt{2}\cos\Theta\cos\Phi \tag{4.7}$$

$$\frac{(g_x + g_y + g_z)}{|\mathbf{g}|} = -\sqrt{3}\sin\Theta \tag{4.8}$$

Therefore, $\tan\Phi$ can be calculated by Eqn. (4.9) and $\sin\Theta$ can be calculated by Eqn. (4.10).

$$\tan\Phi = \frac{g_z + g_y - 2g_x}{\sqrt{3}(g_z - g_y)} \tag{4.9}$$

$$\sin\Theta = -\frac{(g_x + g_y + g_z)}{\sqrt{3}\sqrt{g_x^2 + g_y^2 + g_z^2}} \tag{4.10}$$

Finally, these angles are calculated by Eqn. (4.11) and Eqn. (4.12) because the gravitational components are directly proportional to the output voltages of the sensor (U_x, U_y, and U_z).

$$\Phi = \arctan 2\left\{\left[(U_z - U_x) + (U_y - U_x)\right], \sqrt{3}(U_z - U_y)\right\} \tag{4.11}$$

$$\Theta = \arcsin\left[-\frac{(U_x + U_y + U_z)}{\sqrt{3}\sqrt{U_x^2 + U_y^2 + U_z^2}}\right] \tag{4.12}$$

4.2.4 Interference Cancellation Mechanism

The EMI cancellation is demonstrated by adding noise to all sensor signals. In practical calculation, all voltages in Eqn. (4.11) and Eqn. (4.12) must be substituted by measured voltages (U_{mx}, U_{my}, and U_{mz}) which are the sums of signals (U_x, U_y, and U_z) and external noise (n). Here, according to [21] and the confirmation in Sec. 3.4.2, the author assumed that the external noise on three conductors of twisted cable in this study is also identical. After rewriting Eqn. (4.11) and Eqn. (4.12), all terms of n in Eqn. (4.11) are eliminated by subtractions of differential voltages. Hence, the external noise cannot affect the roll angle. In contrast, all terms of n are remained in Eqn. (4.12); their random variation causes unknown errors in the pitch angle. This influence is inevitable because all voltages in Eqn. (4.12) are single-ended, as in the formulas of the conventional method which can be found in [15, 20, 37].

4.2.5 Calibration Processes

The calibration processes include sensor calibration and orientation adjustment. In the first process, the output scale factor and zero-g bias level of the sensor were calibrated based on [36]. At the beginning of the next process, the sensor was mounted onto the object; an error of several degrees is acceptable. After that, the orientation of the sensor was adjusted to satisfy the geometrical relations in section 4.2.2. This calibration includes two steps: (i) while the object was aligned on a horizontal plane ($\Phi = \Theta = 0$), α was adjusted to ensure that $|g_z| = |g_y|$ and $g_x = 0$; (ii) while the object was aligned with O_1-axis pointed vertically downwards ($\Theta = -90$ deg), γ was adjusted to ensure that $g_z = g_y = g_x$. These two steps should be repeated to make sure all above requirements are satisfied at the same time. It should be noted that the sensor misalignment absolutely does not affect the EMI immunity. The EMI cancellation is due to using the differential voltages.

4.3 Simulations

4.3.1 Simulation Setup

In this study, the author set up a simulation model which is more realistic than that in chapter 3. In Fig. 4.3, two virtual accelerometers whose sensitivity are 660 mV/g generate the ideal sensor signals (U) from the original angles (Φ_O and Θ_O). All signals are added two types of the external noise: common-mode noise has the RMS value of $n_c = 50$–100 mV; differential-mode noise (from six independent sources) has the RMS value of $n_d = 0.5$–1 mV, respectively. The ratio of n_c to n_d was chosen based on the typical common-mode rejection ratio (CMRR) of devices which use low cost twisted cables for transmitting analog signals [5]. Finally, two methods calculate angles from disturbed signals (U_m). Because the roll angle cannot be determined by accelerometer when $\Theta_O = \pm 90$ deg, all simulations are performed with the range of Θ_O is -89 to $+89$ deg and Φ_O is -180 to $+180$ deg.

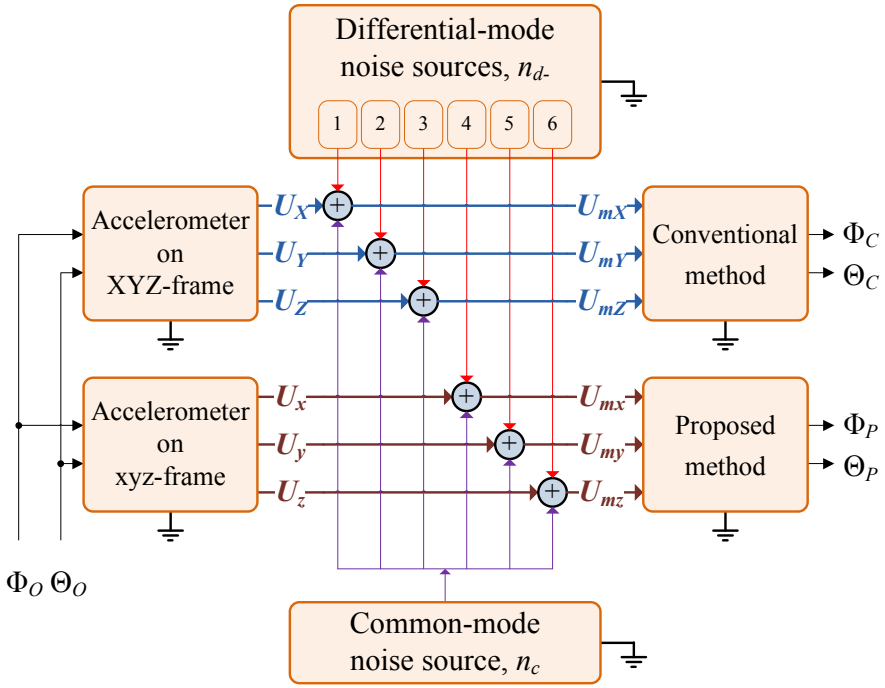

Figure 4.3: One common-mode noise source and six differential-mode noise sources in the simulation model

4.3.2 Simulation Results

The results of both methods were evaluated by subtracting the corresponding original values from the computed values. Figure 4.4 shows the results when there is no external noise ($n_c = n_d = 0$). In this case, all differences are equal to zero. This proves that the new equations calculate the angles as precisely as the conventional formulas. When $n_c = 50$ mV, the upper graph in Fig. 4.5(a) shows small errors in the roll angle of the proposed method. Hence, this angle is almost immune to the external noise. In contrast, the lower graph in Fig. 4.5(a) and both graphs in Fig. 4.5(b) show large errors in three remaining angles. This means that the random noise has significant effects on them. Another simulation with a higher noise intensity (Fig. 4.6) also confirmed the similar results. Furthermore, the higher noise level induces the larger errors in these angles; and the changes in angle errors depend on the magnitude of the pitch angle. The statistical analysis of the angle errors, therefore, is considered in the next test.

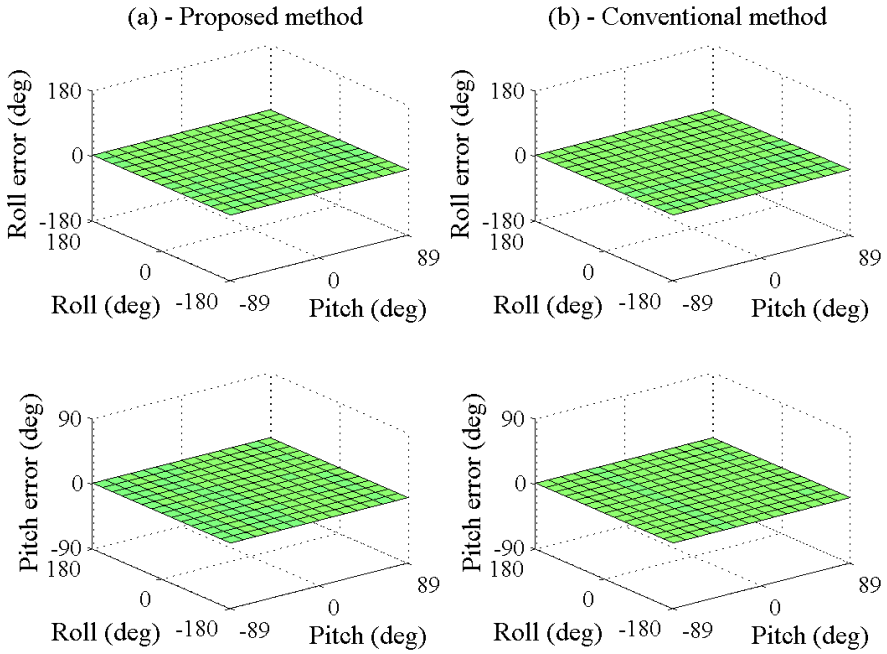

Figure 4.4: Both methods compute the angles precisely when there is no noise

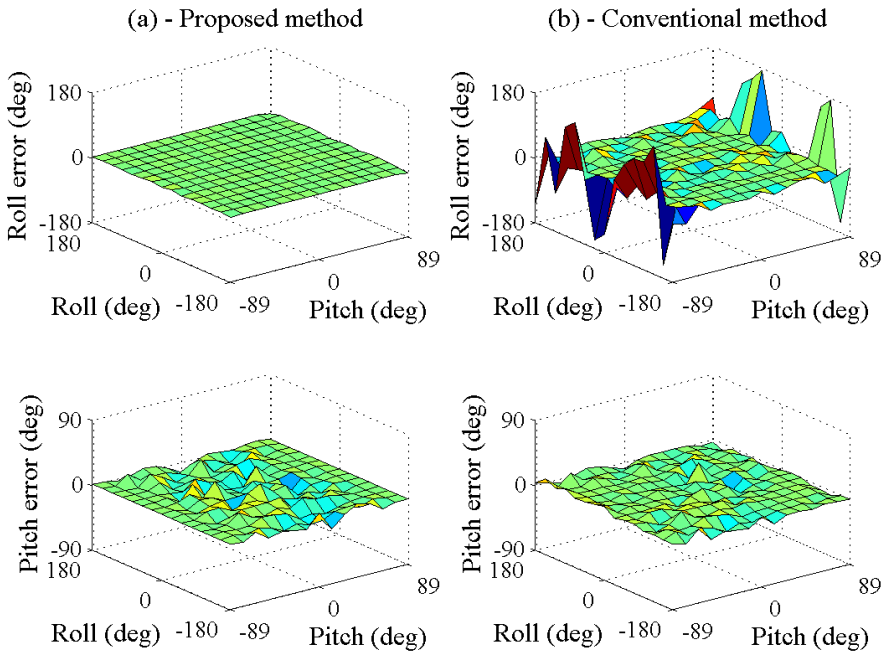

Figure 4.5: Angle errors under the effects of the external noise: $n_c = 50$ mV and $n_d = 0.5$ mV

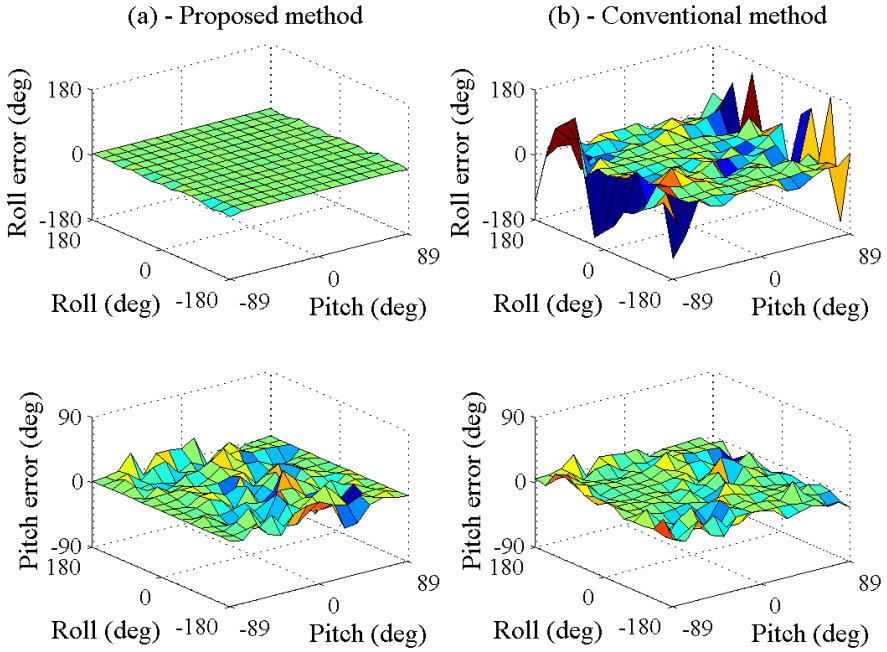

Figure 4.6: Angle errors under the effects of the external noise: $n_c = 100$ mV and $n_d = 1$ mV

Table 4.1 shows mean and SD of the angle errors when the pitch angle is changed from -89 to $+89$ deg. Consequently, clearer comparisons between the angle errors are shown in Fig. 4.7 and Fig. 4.8. When the magnitude of Θ_O increases, the SD of errors in Φ_P is almost small (0.1–2.0 deg), while that of Φ_C is greater and has a significant increase (9.3–73.9 deg). In other words, the precision of the proposed method is significantly higher than that of the conventional method. Furthermore, both of them depend on the slope of the object: the higher slope, the lower precision. Changing this slope also has different effects on the SD of errors in Θ_P and Θ_C which are disturbed strongly by noise. Regarding the measurement accuracy, there is little difference between two methods because the mean values of all angles are small, except Θ_C when $60 \leq |\Theta_C| \leq 89$ deg. Although the mean values of all angles are generally small, the reliability of Φ_C, Θ_P, and Θ_C are very low because of their high variations. In contrast, the value of Φ_P truly reflects the orientation of the sensor.

Table 4.1: Mean values and SD of angle errors on some specific ranges of the pitch angle

Range No.	Values of Θ_O (deg)	Mean (and SD) of errors (deg)			
		In Φ_P	In Φ_C	In Θ_P	In Θ_C
1	-89 to -80	0 (1.9)	-1.0 (73.0)	0.6 (3.2)	6.2 (8.0)
2	-80 to -60	0 (0.3)	0.4 (33.5)	1.5 (7.0)	2.5 (8.2)
3	-60 to -30	0 (0.1)	0.1 (13.5)	2.0 (11.3)	0.7 (8.3)
4	-30 to 0	0 (0.1)	0 (9.3)	1.0 (13.8)	0.3 (8.8)
5	0 to 30	0 (0.1)	0.1 (9.4)	-0.9 (13.9)	-0.2 (8.9)
6	30 to 60	0 (0.1)	-0.1 (13.9)	-1.8 (11.3)	-0.7 (8.3)
7	60 to 80	0 (0.3)	0.2 (34.4)	-1.6 (7.1)	-2.3 (8.3)
8	80 to 89	0 (2.0)	0.8 (73.9)	-0.5 (2.5)	-6.2 (8.1)

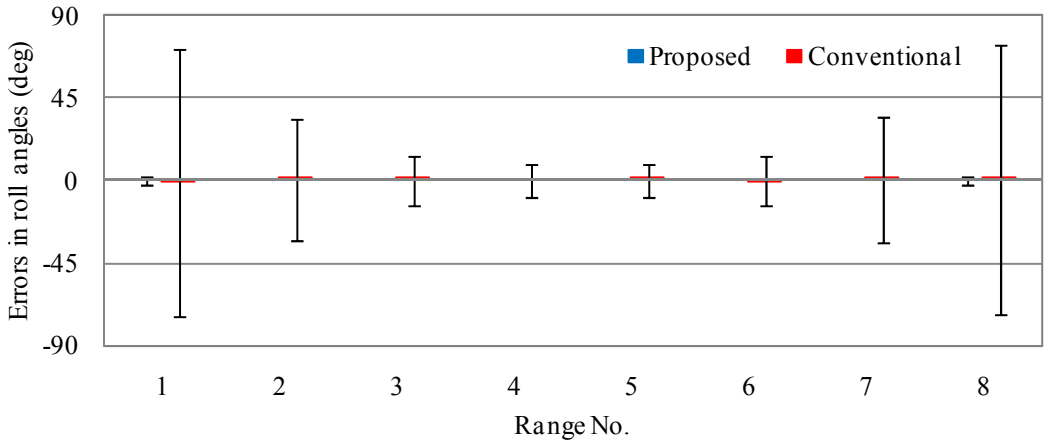

Figure 4.7: Errors in the computed roll angles in different ranges of the original pitch angle

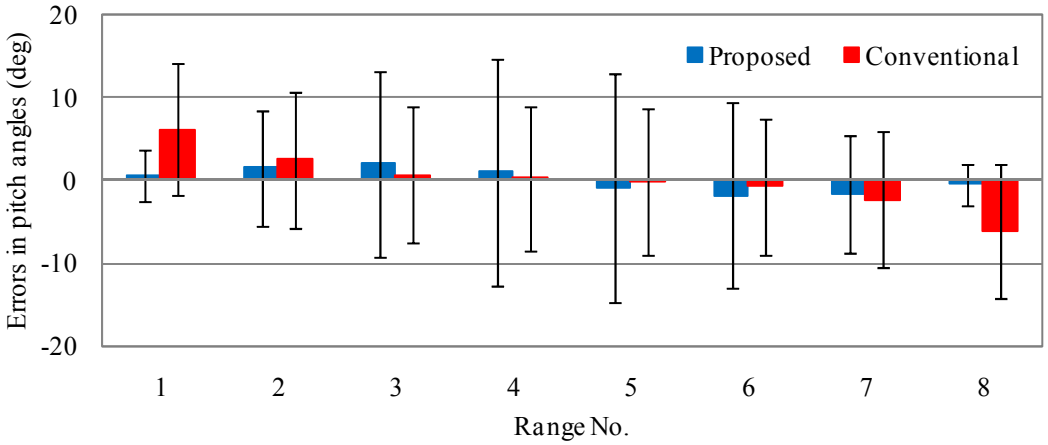

Figure 4.8: Errors in the computed pitch angles in different ranges of the original pitch angle

4.4 Experiments

4.4.1 Experimental Setup

All experiments were conducted with a mechanical system. Fig. 4.9(a) shows a sensor mounting frame which has two mounting points for two accelerometers.

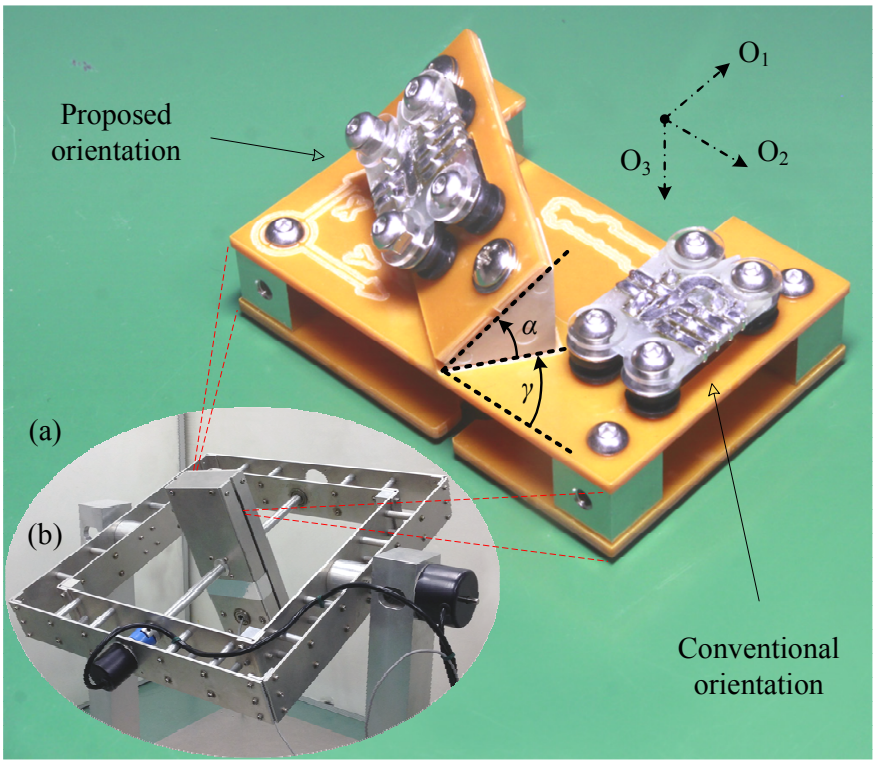

Figure 4.9: Mechanical system in experiments: (a) sensor mounting frame and (b) rotation frame

Around each sensor, there are four bolts and rubber spacers for orientation adjustment. The mounting frame was attached in a rectangular box which can be rotated about two perpendicular axes in the rotation frame, as shown in Fig. 4.9(b). The true rotation angles were measured by two encoders and a microcontroller circuit (ATmega128, Atmel).

In order to evaluate the effects of EMI only, all measurements were conducted under fully static conditions. The whole system was installed at the place where the background vibration is negligible. The rotation angles were fixed at specific values before capturing the signal. In each test, the signals from the sensors were sampled at the highest rate of the DAQ device (100 kHz) in 1 s. The high speed allows capturing as much noise as possible. The EMI sources are all natural and man-made sources present around the measurement system.

4.4.2 Experimental Results

Similar to the experiments in the previous study, a comparison between the RMS values of common-mode and differential-mode interference was repeated in a new configuration. Noise in each single-ended signal was approximated by the difference between the instantaneous voltage and its mean value. In Fig. 4.10, measured noises in three single-ended signals change identically; their RMS values are 104.8 mV, 104.3 mV, and 102.4 mV. On the other hand, the RMS values of following differential noises are 6.8 mV and 6.7 mV. This means that the noise power in differential signals is about 230 times (23.6 dB) smaller than the noise power in single-ended signals.

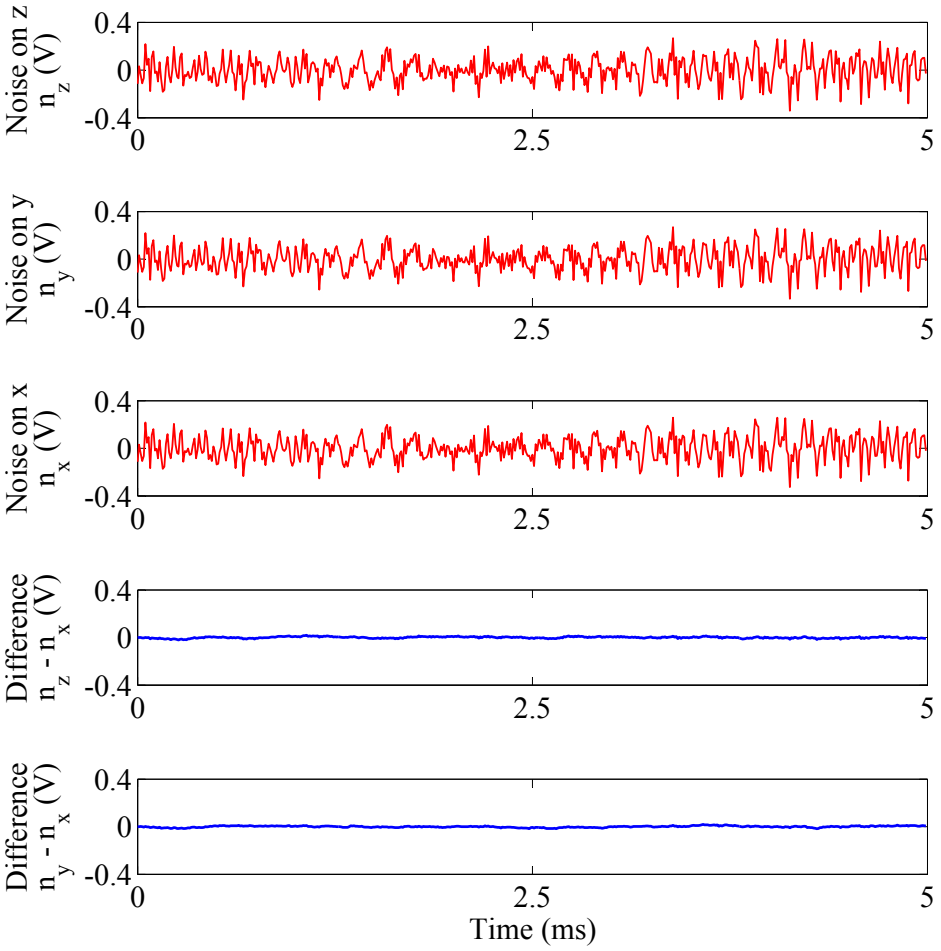

Figure 4.10: Measured noises in single-ended signals and differential signals

After that, the effects of noise on computed angles are demonstrated in Fig 4.11, with the true angles are: $\Phi_O = -45$ deg and $\Theta_O = 80$ deg. In the first graph, the roll angle computed by the proposed method is nearly equal to the true value, whereas the angle computed by the conventional method changes very fast in a range from -77 to -12 deg (error is up to 33 deg). In the second graph, the value computed by the proposed method seems to be better than the result of the conventional method; actually, this could be changed, depending on the orientation.

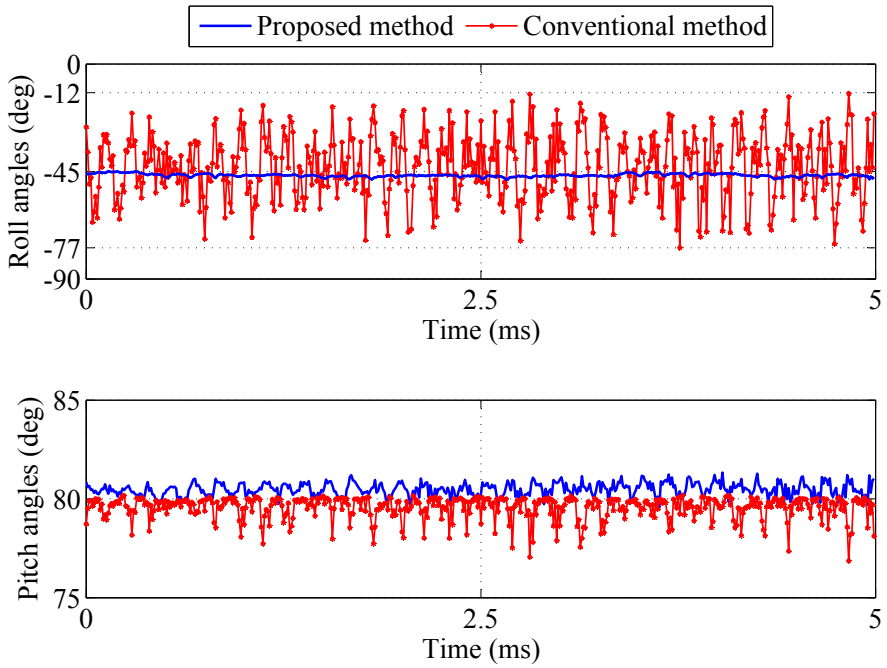

Figure 4.11: Differences between the angles of two methods when $\Phi_O = -45$ deg and $\Theta_O = 80$ deg

In the last experiment, angle errors on some specific orientations were reported in Table 4.2. In addition, the comparisons between the errors of each angle are clearly shown in Fig. 4.12 and Fig. 4.13. First, the mean values of all errors were compared. They are different and not greater than 1.6 deg. Sometimes, the errors of the proposed method are smaller than the errors of the conventional method and vice versa. Hence, there is no remarkable disparity between the accuracy of the two methods. Second, the SD of errors in the roll angles were considered.

Table 4.2: Angle errors (mean and SD) on some specific orientations

Test No.	True angles (deg)		Mean (and SD) of errors (deg)			
	Θ_O	Φ_O	In Φ_P	In Φ_C	In Θ_P	In Θ_C
1	-90	-	- -	- -	0.8 (0.1)	1.4 (0.9)
2	-80	15	-0.4 (0.5)	1.3 (7.2)	-0.8 (0.3)	0.2 (1.7)
3	-60	-130	-1.3 (0.2)	-1.5 (4.5)	-0.2 (1.4)	-1.3 (0.7)
4	-30	55	-0.7 (0.1)	0.6 (0.5)	-0.4 (1.9)	-0.6 (0.3)
5	0	0	-0.2 (0.1)	0 (1.7)	0.1 (2.2)	0.1 (1.7)
6	30	170	-0.6 (0.2)	-0.7 (2.4)	-0.4 (1.9)	0.7 (0.7)
7	60	-95	-1.0 (0.2)	0.1 (2.9)	0.2 (1.1)	0.3 (0.6)
8	80	-45	-1.6 (0.5)	1.5 (12.4)	0.6 (0.4)	-0.4 (0.5)
9	90	-	- -	- -	-1.4 (0.1)	-1.5 (1.0)

The proposed method always has smaller errors than the conventional method. The reduction ratio is from 5 times (when $\Phi_O = 55$ deg and $\Theta_O = -30$ deg) to 22.5 times (when $\Phi_O = -130$ deg and $\Theta_O = -60$ deg). This means that the

precision of the proposed method is significantly higher than the conventional method. In addition, the graphs in Figs. 4.12 and 4.13 also confirm the changes in angle errors when the slope of the object increases, as in the simulation results. Particularly, when this slope is close to ±90 deg, the roll angle computed by the conventional method could be not reliable.

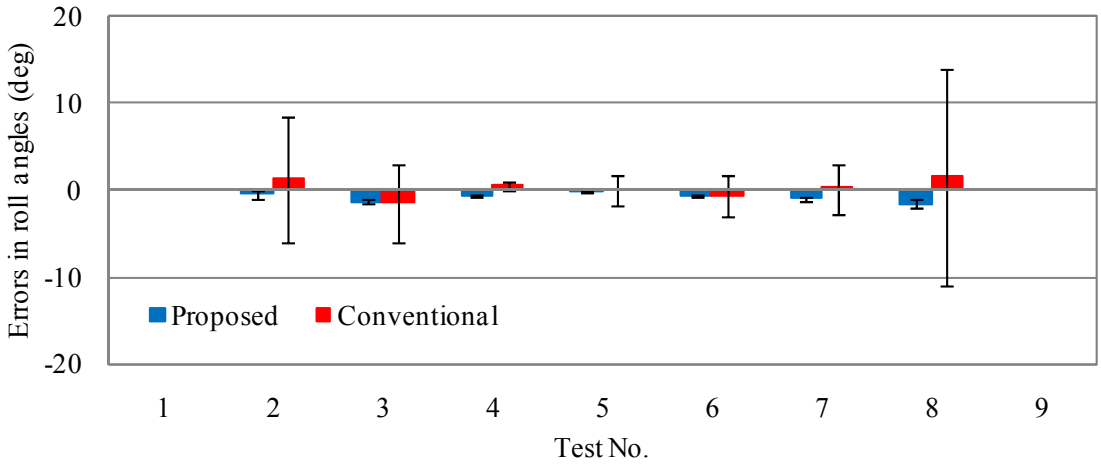

Figure 4.12: Differences between the errors in the computed roll angles

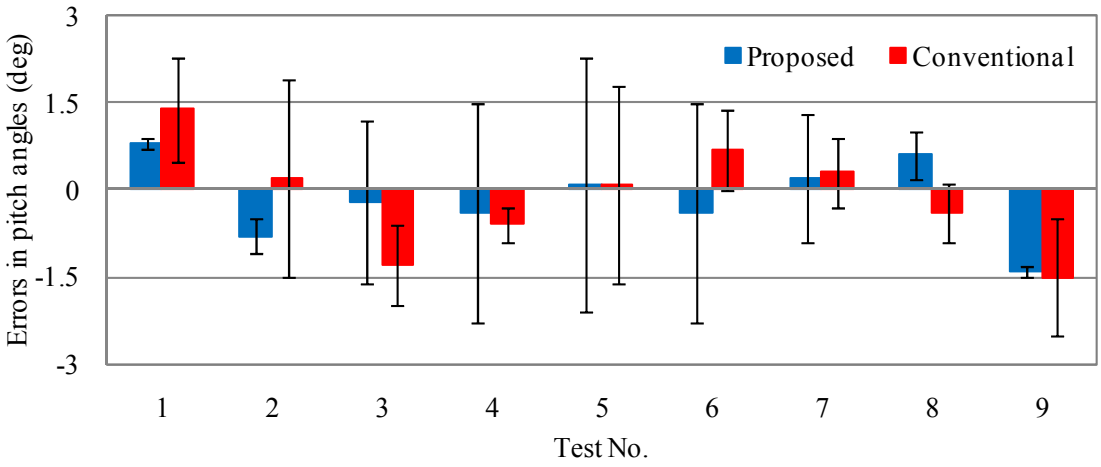

Figure 4.13: Differences between the errors in the computed pitch angles

4.5 Discussion

By mounting the accelerometer on the new orientation, the proposed method can compute the roll angle from the differential voltages to take an advantage of the differential signaling technique. Both simulations and experiments have confirmed the capability to reduce EMI of the proposed method. The roll angle was measured precisely and accurately, although neither shielded cables nor filters were used.

In comparison with the results in Sec. 3.3.2 and Sec. 3.4.2, there are some remarkable differences. First, in simulations, the results of the previous study seem to be better than the current study. Actually, the disparities are due to the simulation models. If the same model is used in both studies, there is no significant difference. Second, in experiments, the mean values of the angle errors are strongly reduced in this study, as the result of the new calibration processes. This mean that even the sensor is mounted on a special orientation, the systematic error is less a problem if the whole system is well calibrated.

4.6 Conclusion

In this chapter, the author has developed and validated a new EMI cancellation method for accelerometers in measuring the roll angle. In this method, the roll angle is completely calculated from the differences in voltage between the sensor outputs. Hence, the common-mode interference induced in connection wires is rejected by a well-known mechanism, as in differential systems. The EMI immunity has been achieved by a new design which takes an advantage of the differential signaling technique within the single-ended system. Both simulations and experiments have been conducted to demonstrate the EMI immunity. The results showed that the angle errors were reduced 5–22.5 times, depending on each orientation. Moreover, the proposed method neither improved nor degraded the accuracy of the pitch angle. Therefore, this study has partially addressed a drawback of the analog sensor in orientation measurement without the need for additional hardware or software.

Chapter 5

EMI Reduction: Solution for Both Non-Euler Angles and Overall Evaluations

This chapter not only presents a solution for the last research on EMI reduction but also provides overall evaluations of the three presented studies. First, the author introduces a solution to improve the EMI immunity of both tilt angles simultaneously when the non-Euler angles are used to represent the tilt. The key mechanism of this study is similar to that in the previous studies; however, the rotation matrices are changed, and therefore the sensor is mounted on new orientations. Second, the novelty and applicability of the three introduced studies are reviewed by evaluating the common advantages and disadvantages of the key idea. In this section, some alternative solutions of the proposed methods are also theoretically introduced. Because of the similarity in the EMI reduction mechanism, only key contributions which are rotation matrix and main formulas are mentioned.

5.1 Introduction

In the previous chapters, when the Euler angles are used to define the two components of the tilt, only one tilt angle can be improved in each study. Because the roles of Θ and Φ are really different, each of them has dedicated applications. Therefore, the use of two separated sensors would be considered when the precision of both angles are required at the same time.

In some cases, there is another method that is using the non-Euler angles. This solution should be considered if the tilt can be represented by two components whose roles are interchangeable, in more details: they are defined by the similar descriptions, as in [28, 30]; the equations which compute these angles have the same form; and the angles have the same range of values (e.g., -90 to $+90$ deg or 0 to $+180$ deg). This type of the tilt angles is suitable for the systems in which the inclinations of two individual coordinate axes (with respect to the gravity or horizontal plane) need to be determined or maintained.

The use of the non-Euler angles has some advantages. Because of the definition, the change in one angle does not affect the remaining one. For instance, in Fig. 2.4, a rotation about the O_2-axis can change θ_1 to any value while θ_2 is constant; and a rotation about the O_1-axis can adjust θ_2 while θ_1 is unchanged. Meanwhile, in Fig. 2.3, when the two angles are defined by a rotation sequence that is yaw-pitch-roll, the change in one angle could affect the other. Here, adjusting the roll angle (Φ, the third rotation) while the pitch angle (Θ, the second rotation) is fixed can be done easily by rotating the object about the O_2-axis. However, it is difficult to change the pitch angle while the roll angle is kept constant. This movement cannot be done by only one elemental rotation. Another advantage of using the non-Euler angle is that both θ_1 and θ_2 can be determined in all orientations. Meanwhile, although the Euler angles have some merits in attitude expression [16, 22], Φ cannot be computed when $\Theta = \pm 90$ deg. Even when $|\Theta|$ is not exactly equal to 90 deg, the value of Φ may not be precise and should not be used [37].

This chapter has two separated hafts. In the first one, a method of EMI reduction for both θ_1 and θ_2 is proposed. This method uses the same reduction

mechanism as in chapters 3 and 4. Thus, only main contributions, including definition of the new orientation and the process of developing the new equations, are shown. The novelty of the study is both angles can be simultaneously immune to EMI instead of only one angle as in the previous chapters. In the second haft, the author evaluates the common advantages as well as the disadvantages of the three presented methods and introduces a equivalent mounting orientation for each study.

5.2 Solution of EMI Reduction for Both Non-Euler Angles

5.2.1 New Mounting Orientation

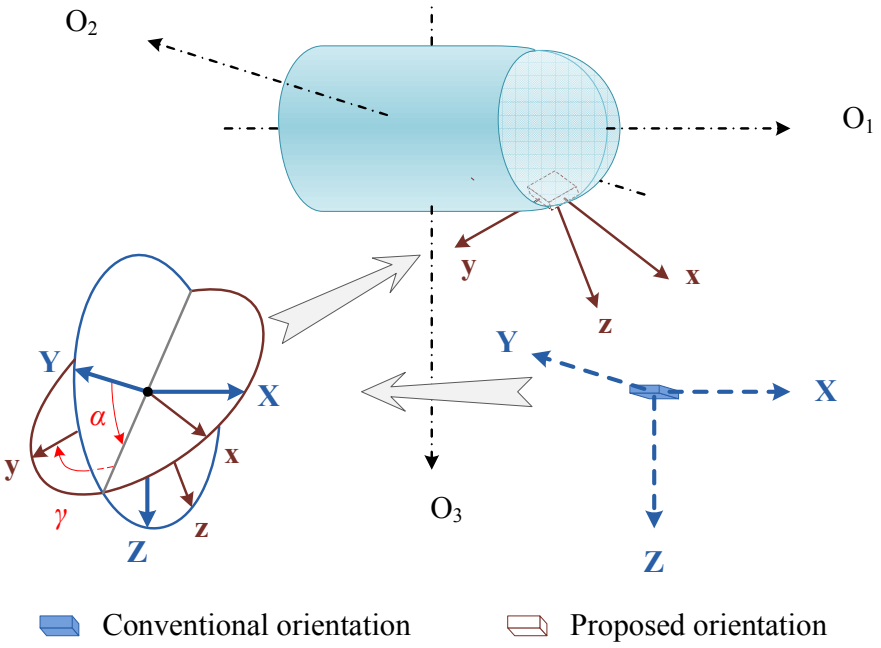

Figure 5.1: The definition of the proposed orientation in measuring both non-Euler tilt angles

Figure 5.1 illustrates the new mounting orientation for the accelerometer. This orientation is defined by a rotation matrix that rotates the XYZ-frame about the

X-axis by α first, and then about the new Z-axis by γ. The values of α and γ are proposed in Eqn. (5.1). Both α and γ have positive values because they represent the rotations which appear counterclockwise when observing in the negative direction of the axes.

$$\begin{bmatrix} \alpha \\ \gamma \end{bmatrix} = \begin{bmatrix} \arctan\sqrt{2} \\ \pi/4 \end{bmatrix} \tag{5.1}$$

5.2.2 New Calculation Formulas

The conventional formulas and the rotation matrix are combined to build the new formulas. First, two elemental rotation matrices expressed in Eqn. (2.6) and Eqn. (2.8) were combined to calculate $R_{\theta_{1,2}}$ in Eqn. (5.2). After substituting the given values of α and γ, all elements of $R_{\theta_{1,2}}$ are calculated and shown in Eqn. (5.3). Hence, the relation between the gravitational components on the two coordinate systems can be determined in Eqn. (5.4).

$$\begin{aligned} R_{\theta_{1,2}} &= R_Z(\gamma)R_X(\alpha) \\ &= \begin{bmatrix} \cos\gamma & \cos\alpha\sin\gamma & \sin\alpha\sin\gamma \\ -\sin\gamma & \cos\alpha\cos\gamma & \cos\gamma\sin\alpha \\ 0 & -\sin\alpha & \cos\alpha \end{bmatrix} \end{aligned} \tag{5.2}$$

$$R_{\theta_{1,2}} = \frac{\sqrt{6}}{6}\begin{bmatrix} \sqrt{3} & 1 & \sqrt{2} \\ -\sqrt{3} & 1 & \sqrt{2} \\ 0 & -2 & \sqrt{2} \end{bmatrix} \tag{5.3}$$

$$\begin{bmatrix} g_x \\ g_y \\ g_z \end{bmatrix} = \frac{\sqrt{6}}{6}\begin{bmatrix} \sqrt{3}g_X + g_Y + \sqrt{2}g_Z \\ -\sqrt{3}g_X + g_Y + \sqrt{2}g_Z \\ -2g_Y + \sqrt{2}g_Z \end{bmatrix} \tag{5.4}$$

The tilt angles can be calculated by combining the sub-equations in Eqn. (5.4). First, by adding or subtracting each side of a sub-equation from the corresponding

sides of the others, two intermediate equations are achieved, as in Eqn. (5.5) and Eqn. (5.6).

$$g_x - g_y = \sqrt{2} g_X \tag{5.5}$$

$$g_x + g_y - 2g_z = \sqrt{6} g_Y \tag{5.6}$$

Therefore, on the basis of the equations in Sec. 2.2.2.3, θ_1 can be calculated by Eqn. (5.7) and θ_2 can be calculated by Eqn. (5.8).

$$\begin{aligned} \theta_1 &= \arcsin\left(-\frac{g_X}{|\mathbf{g}|}\right) \\ &= \arcsin\left[\frac{1}{\sqrt{2}}\frac{(g_y - g_x)}{\sqrt{g_x^2 + g_y^2 + g_z^2}}\right] \end{aligned} \tag{5.7}$$

$$\begin{aligned} \theta_2 &= \arcsin\left(-\frac{g_Y}{|\mathbf{g}|}\right) \\ &= \arcsin\left[\frac{1}{\sqrt{6}}\frac{(2g_z - g_y - g_x)}{\sqrt{g_x^2 + g_y^2 + g_z^2}}\right] \end{aligned} \tag{5.8}$$

Finally, these angles are calculated by Eqn. (5.9) and Eqn. (5.10) because the gravitational components are directly proportional to the output voltages of the sensor. Here, the value of U is defined in Eqn. (5.11).

$$\theta_1 = \arcsin\left[\frac{1}{\sqrt{2}}\frac{(U_y - U_x)}{U}\right] \tag{5.9}$$

$$\theta_2 = \arcsin\left\{\frac{1}{\sqrt{6}}\frac{[(U_z - U_y) + (U_z - U_x)]}{U}\right\} \tag{5.10}$$

$$U = \sqrt{U_x^2 + U_y^2 + U_z^2} \tag{5.11}$$

5.2.3 Interference Cancellation Mechanism

Once again, the EMI cancellation is demonstrated by adding noise to all sensor signals. In practical calculation, all voltages in Eqn. (5.9) and Eqn. (5.10) must be substituted by the measured voltages which are the sums of signals and external noise (n). According to the Sec. 3.2.3, although the external noise affects the signals, the value of U can be recovered by filtering the disturbed value (U_m) with a low cutoff frequency. This filter does not degrade the response speed of the whole system.

After rewriting Eqns. (5.9) and (5.10) with the actual measured voltages, all terms of n in both equations are eliminated by subtractions of differential voltages. Hence, the external noise cannot affect θ_1 and θ_2. In other words, the new method can measure both tilt angles without the effects of the common-mode interference.

5.3 Overall Evaluations

5.3.1 Advantages and Challenges

In three chapters, the author has proposed, developed, and validated a new idea of EMI reduction for the analog accelerometers. Both simulations and experiments confirmed the notable improvement that is the computed values of one or two tilt angles can be immune to external noise without shielded cables, shielding systems, filters, and preprocessors. In other words, the new methods can measure the angles precisely and accurately within a minimum resource.

In general, the precision depends on the intrinsic noise density of sensors and quality of twisted cables. Meanwhile, the accuracy depends on the linearity of accelerometers and alignment of orientation [11]. Because the noise density of the sensor is not low enough (45 $\mu g/\sqrt{\text{Hz}}$), a comparison between the proposed methods and other EMI suppression methods was not presented in this work. This comparison should be performed only if the intrinsic noise of the sensor

is considerably smaller than the external interference after being suppressed. In other words, the better method cannot be determined by a low cost accelerometer.

The proposed methods can be combined with the others reduction methods such as using shielding systems, shielded cables, or filters to enhance the reliability of the results [9]. In analog systems, the combinations between the traditional solutions and new physical designs are widely used to enhance the noise immunity. For instance, good printed circuit boards and well-designed integrated circuits themselves partly reject the electromagnetic interference [41, 43].

In the proposed methods, quantity and size of the connection wires are other advantages. In spite of using the differential voltages, the proposed methods need three wires instead of six wires for transmitting three signals, as the normal differential configuration. The twisted cable in each study has a size of 0.5 mm, and could be much smaller if needed. In particular, a smaller twist cable may have a greater number of twists per meter, and therefore has better EMI cancellation [23]. However, when the distance between conductors is small, the effect of coupling capacitance on high frequency signals should be considered. In some applications, for example, in surgical robots or flexible endoscopes, small twisted wires can save more space than a set of three coaxial cables which have multi-layer materials.

There is another approach method that is using a truly differential configuration. In this case, there is the need for a differential accelerometer or the combination between a single-ended sensor and converters. The converters transform the single-ended signals to differential signals before transmitting. However, this long-established technique has its own limitations such as: the differential accelerometer is not commonly used; the converters require mounting space, separated power supply, and two electrical wires for each differential signal. Hence, the applicability of this solution may be limited.

Finally, the difficulty of sensor mounting was considered. The rotated accelerometer requires an adapter or a special circuit to convert the conventional orientation to the proposed orientation. Assembling adapter can be done with a high precision machine tool; however, the size of the sensor unit could increase.

This challenge may be less of a problem when the sensor is mounted separately. Particularly, when the accelerometer is far from the processing circuit, the proposed method could be an effective solution. In some cases, the attachment of the sensor can be done easier if there are some equivalent mounting methods. This idea is partially developed in the next sections.

5.3.2 Alternative Solution for the Non-Euler Angles

In the study of EMI reduction for the non-Euler angles, there is another rotation sequence that can be used to define the new mounting orientation of the sensor. In this sequence, the sensor is rotated about the Y-axis by $\beta = -\arctan\sqrt{2}$ first, and then about the new Z-axis by $\gamma = -45$ deg. Hence, the corresponding rotation matrix can be calculated in Eqn. (5.12)

$$R'_{\theta_{1,2}} = \frac{\sqrt{6}}{6}\begin{bmatrix} 1 & -\sqrt{3} & \sqrt{2} \\ 1 & \sqrt{3} & \sqrt{2} \\ -2 & 0 & \sqrt{2} \end{bmatrix} \tag{5.12}$$

By using this rotation matrix, the new calculation formulas can be built in the same way as the steps in Sec. 5.2. The detailed equations are formulated in Appendix C. The final calculations are shown in Eqns. (5.13) and (5.14). These equations are similar to those of the first solution. However, the positions of the two angles are exchanged and the sign of the numerator in Eqn. (5.14) has been reversed. Because the two tilt angles are computed from the differential voltages, they are immune to external EMI.

$$\theta_1 = \arcsin\left\{\frac{1}{\sqrt{6}}\frac{[(U_z - U_y) + (U_z - U_x)]}{U}\right\} \tag{5.13}$$

$$\theta_2 = \arcsin\left[\frac{1}{\sqrt{2}}\frac{(U_x - U_y)}{U}\right] \tag{5.14}$$

5.3.3 Alternative Solutions for the Euler Angles

In the latest research results, each method in chapter 3 and chapter 4 can be implemented by another solution. In the method of EMI reduction for the pitch angle, the same EMI cancellation capability can be achieved without the rotation of the sensor about the X-axis. In other words, the new mounting orientation (xyz-frame) is defined from the conventional (XYZ-frame) only by the rotation about the Z-axis. The rotation angle is unchanged, equal to 45 deg. Therefore, this conversion is more optimized and the implementation is simpler than the previously proposed design. After formulating the equations (see Appendix A), the rotation matrix and angle calculations are expressed in Eqns. (5.15), (5.16), and (5.17).

$$R'_{\Theta} = \frac{1}{2}\begin{bmatrix} \sqrt{2} & \sqrt{2} & 0 \\ -\sqrt{2} & \sqrt{2} & 0 \\ 0 & 0 & 2 \end{bmatrix} \tag{5.15}$$

$$\sin\Theta = \frac{\sqrt{2}}{2}\frac{(U_y - U_x)}{\sqrt{U_x^2 + U_y^2 + U_z^2}} \tag{5.16}$$

$$\tan\Phi = \frac{U_x + U_y}{\sqrt{2}U_z} \tag{5.17}$$

In the method of EMI reduction for the roll angle, there is another design in which the rotation matrix rotates the sensor about the Y-axis by $\beta = \arctan\sqrt{2}$ first, and then about the new X-axis by $\alpha = 45$ deg. The main formulas, therefore, are achieved as in Eqns. (5.18), (5.19), and (5.20). The detailed convertion steps can be found in Appendix B.

$$R'_{\Phi} = \frac{\sqrt{6}}{6}\begin{bmatrix} \sqrt{2} & 0 & -2 \\ \sqrt{2} & \sqrt{3} & 1 \\ \sqrt{2} & -\sqrt{3} & 1 \end{bmatrix} \tag{5.18}$$

$$\Phi = \arctan 2\left\{\sqrt{3}(U_y - U_z), [(U_z - U_x) + (U_y - U_x)]\right\} \tag{5.19}$$

$$\Theta = \arcsin\left[-\frac{(U_x + U_y + U_z)}{\sqrt{3}\sqrt{U_x^2 + U_y^2 + U_z^2}}\right] \tag{5.20}$$

5.4 Discussion and Conclusion

In this chapter, the author has introduced a method of EMI reduction when the non-Euler angles are used to represent the tilt. The most important advantage of this study is both components of the tilt can be improved at the same time. Hence, by using only one sensor mounted on the proposed orientation, the tilt angles can be immune to the external EMI without the need for additional software and hardware.

After introducing the last research on EMI reduction, the author has reviewed the advantages and disadvantages to highlight the novelty and applicability of the three presented studies. Although there are some shortcomings that need to be addressed in a further research, the proposed studies have partially solved the limitations of the tilt measurement technique. Moreover, this chapter provides some alternative designs for the presented studies. This supplementation allows designers to choose the solution which is more convenient for their applications.

Chapter 6

Sensor Fusion in Tilt Measurement for Surgical Devices

This chapter presents a new method for estimating the tilt angles of endoscopic images in static and dynamic states. Disorientation is one of the major challenges in NOTES procedures. Reorientation allows surgeons or gastroenterologists to work in off-axis conditions and provides an important reference for coupling a secondary image. This study presents a new sensor-fusion method for reducing the shock-based error. The key algorithm is a special predict-and-choose process which combines the accelerometer readings and the output data of a tri-axial gyroscope to predict the gravitational components. The prediction data are used to calculate the tilt angles. The result is evaluated by being applied in a well-known application, endoscopic horizon stabilization. Compared with the reference method, the proposed method has notable advantages. The simulation and experimental results showed small errors, smooth angle change, and a small delay time. The tilt angles are reliable without any cumulative error under the prolonged motion [8].

6.1 Introduction

NOTES is a recently invented surgical technique that allows access to the human body through natural orifices. A flexible endoscope is taken into the human body through a natural entry, such as the mouth, vagina, or anus [14]. Surgeons can perform the procedures with at least two working instrument channels, a camera, and an illumination system. This technique can minimize common complications such as wound infections, incisional hernias, postoperative pain, and adhesions. By avoiding skin incisions, NOTES has clinical and aesthetic advantages over other techniques [33].

Accessing the abdominal cavity through natural orifices makes it difficult to maintain spatial orientation. The direction of the camera mounted on the tip of the flexible endoscope changes continuously during the procedure. The endoscopic image can be rotated upside down, retroflexed, or oriented toward other reverse observation angles [34]. This can be a significant barrier for even experienced surgeons. The Natural Orifice Surgery Consortium for Assessment and Research (NOSCAR) working group identified many fundamental challenges to the safe introduction of NOTES [39]. Maintaining spatial orientation was identified as a vital requirement for every NOTES system. The group also suggested an electronic video stabilization/rectification solution and the use of multiple cameras to get a better in-line view of the operative field.

In this chapter, the author proposes a new sensor-fusion method for estimating the endoscopic orientation. The main sensor is a MEMS module that contains a triaxial accelerometer and a triaxial gyroscope. In the static state, three gravitational components (g-components) are accelerometer readings. In the dynamic state, the predict-and-choose process is used to estimate the next values of g-components from the current values. At each time-step, firstly, the effects of the three rotational components are separated into each of g-components to calculate the elemental changes. These amounts are used to predict some future values for g-components. Finally, the proposed algorithm chooses the most suitable value by analyzing the difference among prediction values and newest accelerometer

readings. In addition, a feedback loop is used to reduce not only the prediction deviation but also the sensor errors. The results are guaranteed to be good and without cumulative error. By using the prediction algorithm, the proposed method allows the small time delay and high speed responses.

The proposed method was tested by applying the results to a well-known application, endoscopic horizon stabilization. Many testing conditions in both simulation and experiment were used. In some conditions, the acceleration could reach up to 10 m/s^2, which is roughly equal to 1 g. The comparison with the reference method shows notable advantages of the proposed method. The testing results show a smaller error in angle, a smaller ripple, and a shorter time delay, even though the complexity and the size of the required hardware are similar.

6.2 Proposed Method

6.2.1 Additional Hardware and Data Characteristic

6.2.1.1 System Hardware

In addition to a computer and display devices, the system hardware consists of two major units. Figure 6.1 shows the inertial measurement unit (IMU), which contains a triaxial accelerometer and a triaxial gyroscope. The tiny circuit of IMU is hermetically sealed and attached to the tip of the flexible endoscope as shown in Fig. 6.2(a). Four tiny wires connect the IMU to an external box. The external box contains an 8-bit microcontroller and a video capture device. Both sensor data and captured video signal are sent to the computer for processing. This is the basic configuration for horizon stabilization. For other applications, additional hardware and software may be necessary.

6.2.1.2 Input Data

The input data is the motion of IMU. In surgery, the acceleration and angular velocity have their own characteristic. During the surgical procedure, the

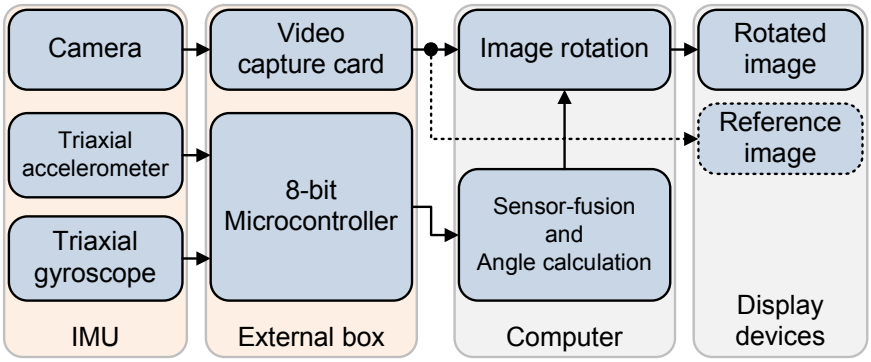

Figure 6.1: System overview with key components and key processes in the basic application

linear velocity of endoscope cannot be high. Thus, the magnitude of **a** is generally small or its direction changes alternately. When **a** is high in a motion, the duration cannot be long to avoid the rapid change in linear velocity. Other random movements and vibrations also introduce random changes in the sensor data. Therefore, each accelerometer reading F_k generally fluctuates around the corresponding g-component g_k. In other words, the mean value of F_k in each narrow window reflects the tendency of g_k to change. Here, the subscript k is used instead of x, y, and z to represent their collections (e.g., F_k means F_x, F_y, and/or F_z). The above characteristic will be used in later sections.

6.2.1.3 Output Data

The key output of the system is the tilt angles of the endoscopic camera. In Fig. 6.2(b), the roll angle (Φ) is the rotation angle of the camera image. The angle pitch angle (Θ) is the angular slope of the flexible endoscope tip. Hence, Φ is the most important data. It should be noted that Φ, Θ, and Ψ cannot be calculated from ω_x, ω_y, and ω_z by simple linear function because their reference frames are different.

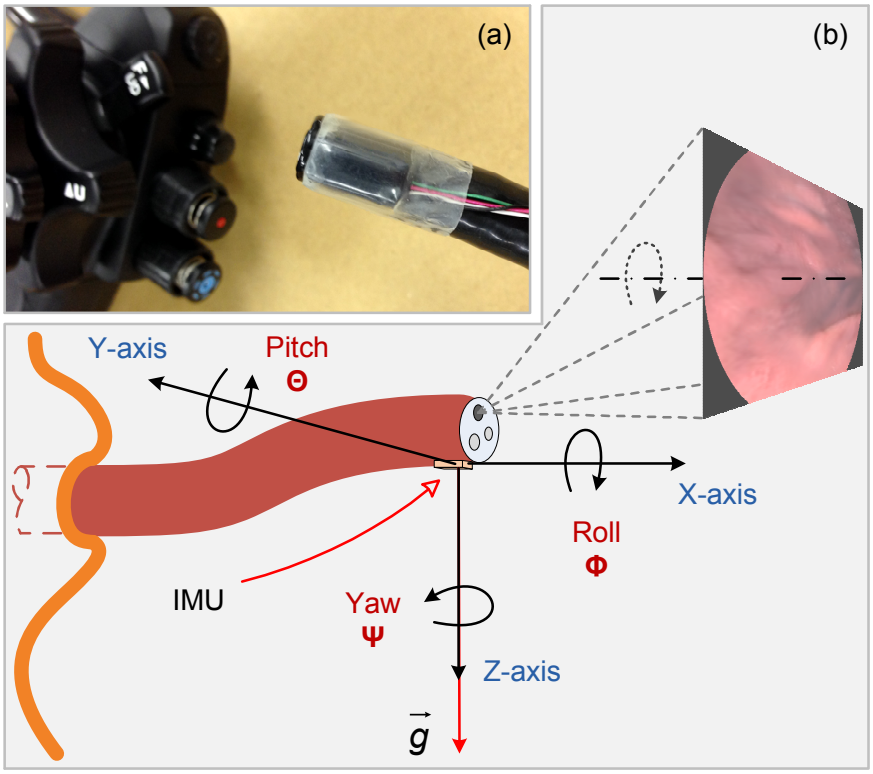

Figure 6.2: The tip of the flexible endoscope: (a) position of the IMU and (b) three elemental rotations

6.2.2 Sensor Fusion

The predict-and-choose process are used to combine data from accelerometer and gyroscope. In this process, the key operation is estimating the g-components under all conditions, as illustrated in Fig. 6.3. In any static state, **F** and **g** are identical. The g-components are directly measured with the accelerometer and the time point (n) is set to zero. When motion appears, the predict-and-choose process iteratively estimates **g** whenever getting the new data from sensors. The main steps are described in following subsections.

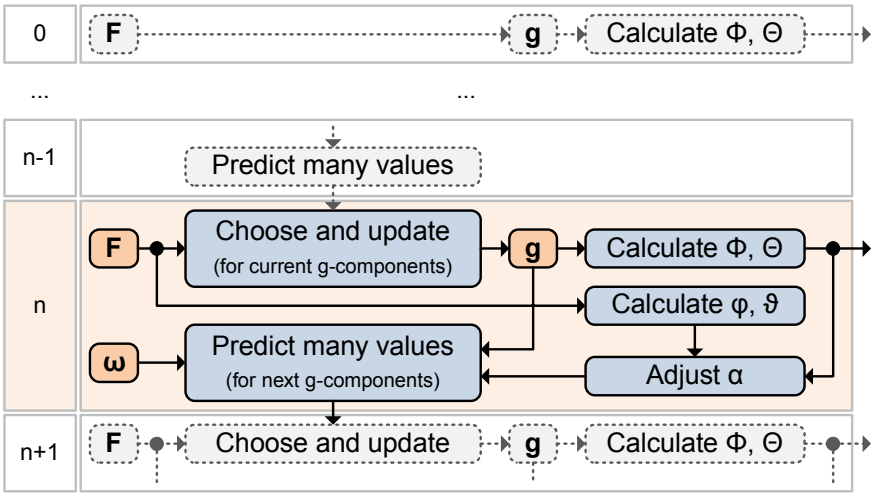

Figure 6.3: Sensor-fusion in the predict-and-choose process

6.2.2.1 Predicting Many Values

At each time-step, firstly, the elemental changes in g_k are estimated. The effects of each elemental rotation on each gravitational component are quantified. In Fig. 6.4(a), the influence of the rotation about Z-axis is considered. The component g_z is unchanged, whereas g_y and g_x are changed. The projection g_{yx} becomes g'_{yx}; their magnitudes are equal. The angle r'_z can be calculated from g_x, g_y, and ω_z. Using g'_{yx} and r'_z, we can compute $g_{x,1}$ and $g_{y,1}$. Therefore, the rotation about the Z-axis changes g_x and g_y by amounts that are determined by the difference between them and $g_{x,1}$ and $g_{y,1}$. Similarly, the change in g_x and g_z caused by the rotation about the Y-axis and the change in g_y and g_z arising from the rotation about the X-axis can be calculated, as shown in Fig. 6.4(b). Thus, six elemental changes (Δ values) are computed by using Eqn. (6.1) and then Eqn. (6.2). In Eqn. (6.1), coefficient α is used to slightly adjust the angular velocity. During some first time-steps, $\alpha = 1$; this gain coefficient will be changed later.

$$\begin{bmatrix} r'_x \\ r'_y \\ r'_z \end{bmatrix} = \begin{bmatrix} \arctan 2(g_{y_n}, g_{z_n}) + (\alpha \times \omega_{x_n}) \times \Delta_t \\ \arctan 2(g_{z_n}, g_{x_n}) + (\alpha \times \omega_{y_n}) \times \Delta_t \\ \arctan 2(g_{x_n}, g_{y_n}) + (\alpha \times \omega_{z_n}) \times \Delta_t \end{bmatrix} \tag{6.1}$$

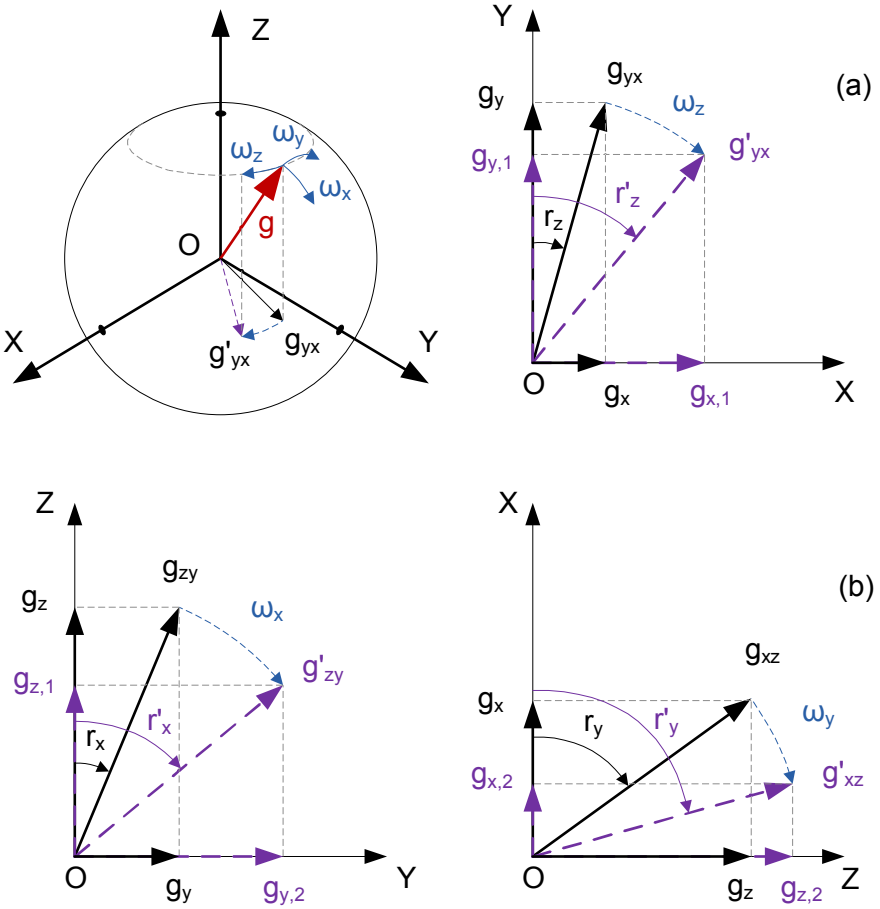

Figure 6.4: Gravitational vector changes caused by each rotation component: (a) rotation about Z-axis changes g_x and g_y; (b) rotation about the X-axis changes g_y and g_z; and the rotation about the Y-axis changes g_z and g_x

$$\begin{bmatrix} \Delta_{x,1} \\ \Delta_{x,2} \\ \Delta_{y,1} \\ \Delta_{y,2} \\ \Delta_{z,1} \\ \Delta_{z,2} \end{bmatrix} = \begin{bmatrix} \sqrt{g_{y_n}^2 + g_{x_n}^2} \times \sin r'_z - g_{x_n} \\ \sqrt{g_{x_n}^2 + g_{z_n}^2} \times \cos r'_y - g_{x_n} \\ \sqrt{g_{y_n}^2 + g_{x_n}^2} \times \cos r'_z - g_{y_n} \\ \sqrt{g_{z_n}^2 + g_{y_n}^2} \times \sin r'_x - g_{y_n} \\ \sqrt{g_{z_n}^2 + g_{y_n}^2} \times \cos r'_x - g_{z_n} \\ \sqrt{g_{x_n}^2 + g_{z_n}^2} \times \sin r'_y - g_{z_n} \end{bmatrix} \tag{6.2}$$

After getting the elemental changes, the magnitude of each $g_{k_{n+1}}$ is predicted. This step seems not to be complicated. Actually, the six elemental changes depend on not only the motion, but also unknown sensor errors and random noise.

Under the influence of error and noise, the Δ values could be changed in magnitude and reversed in sign. Therefore, instead of using only one expression for predicting $g_{k_{n+1}}$, the author flexibly adjusts g_k in many ways to get a set of prediction values. Basically, on each axis, we get k_1 to k_4 by adding or subtracting the Δ values as in Eqn. (6.3). On the other hand, the feedback loop allows using k_5 to k_8 to improve the smoothness of the result. The most suitable value is chosen in the next step.

$$\begin{bmatrix} k_1 \\ k_2 \\ k_3 \\ k_4 \\ k_5 \\ k_6 \\ k_7 \\ k_8 \end{bmatrix} = g_{k_n} + \begin{bmatrix} \Delta_{k,1} + \Delta_{k,2} \\ \Delta_{k,1} - \Delta_{k,2} \\ -\Delta_{k,1} + \Delta_{k,2} \\ -\Delta_{k,1} - \Delta_{k,2} \\ \Delta_{k,1} \\ -\Delta_{k,1} \\ \Delta_{k,2} \\ -\Delta_{k,2} \end{bmatrix} \tag{6.3}$$

6.2.2.2 Choosing the Most Suitable Value

The approximate value of $g_{k_{n+1}}$ is chosen from eight values of k_i. Firstly, the variation of F_k is considered. As soon as the accelerometer updates $F_{k_{n+1}}$, the author uses Eqn. (6.4) to quantify and Eqn. (6.5) to accumulate the fluctuation. Coefficient β_k is calculated from a sliding window of w past time-steps. The random vibration of IMU generally makes β_k decreases, whereas the directed movement of IMU generally makes β_k increases. Thus, a threshold of β_0 between 0 and 1 is used to identify the influence of motion. Secondly, eight differences between k_i and $F_{k_{n+1}}$ are considered. When motion is gentle, the smallest difference points out the best prediction value. When motion becomes stronger: if vibration has less effect ($\beta_k \geq \beta_0$), the smallest difference still determines which k_i is chosen; if vibration has greater effect ($\beta_k < \beta_0$), the second smallest difference is used to determine which k_i will be $g_{k_{n+1}}$. Hence, the elemental changes are used to flexibly adjust g-components at each time-step. Because of the mentioned characteristic in Sec. 6.2.1.2, this algorithm makes the prediction follows the true value of g_k.

Although F_k still affects predicted g_k, using some additional thresholds of β_k may reduce the ripple.

$$\delta_{k_n} = F_{k_{n+1}} - g_{k_n} \tag{6.4}$$

$$\beta_k = \frac{|\sum_{i=0}^{w-1} \delta_{k_{n-i}}|}{\sum_{i=0}^{w-1} |\delta_{k_{n-i}}|} \tag{6.5}$$

6.2.3 Angle Calculation and Feedback

6.2.3.1 Angle Calculation

Three values of g_x, g_y, and g_z reflect the tilt angles of the IMU. The value of Φ is computed by using Eqn. (2.12) while Θ is computed by Eqn. (2.13). These formulas are widely used in aircraft instrumentation, inertial navigation systems, and mobile devices [13, 15, 37].

6.2.3.2 Feedback Loop

A feedback loop is used to adjust the gain coefficient (α) of the angular velocity. The adjustment relies on the comparison between the tilt angles and two raw angles. In Fig. 6.3, the tilt angles (Φ and Θ) are calculated from the g-components, whereas the raw angles (φ and ϑ) are calculated from the components of $\mathbf{F}$ by the similar formulas. The gain coefficient is adjusted against the difference between tilt angles and raw angles in many consecutive time-steps.

The adjustment has two goals: to improve prediction errors and to improve sensor errors. The prediction errors are generated when using the approximate values in the previous step. Stronger fluctuation of $\mathbf{F}$ generally causes the larger prediction errors and the rapid change in angles. This effect is partly evaluated by α_n in Eqn. (6.6). Here, the offsets between tilt angles and raw angles affect numerators while the rapid change in raw angles affects the denominators. A positive factor d is used to limit the dynamic range of α_n. Equation (6.7) updates α

by accumulating all effects in a sliding window of v past time-steps. Generally, the fluctuation of $\mathbf{F}$ makes α slightly decrease whereas the constant offsets between two types of angles make α slightly increase. In other words, the angular velocity will be slowed down under vibration and sped up when the mean values of the raw angles change faster than those of the tilt angles. In actual implement, because the value of α is always greater than or equal to 1, the initial sensitivity of the gyroscope is chosen to be smaller than its typical value. During the operation, the effective sensitivity is automatically changed. By this adjustment, the feedback loop can reduce not only the ripple in output angles but also the sensor errors. The second improvement includes scale-factor errors and non-linearity. These errors have a notable impact on systems that use MEMS gyroscopes [26].

$$\alpha_n = \frac{|\Phi_n - \varphi_{n-1}|}{d + |\varphi_n - \varphi_{n-1}|} + \frac{|\Theta_n - \vartheta_{n-1}|}{d + |\vartheta_n - \vartheta_{n-1}|} \tag{6.6}$$

$$\alpha = 1 + \frac{\sum_{i=0}^{v-1} \alpha_{n-i}}{v} \tag{6.7}$$

6.2.4 Other Processes

6.2.4.1 Data Downsampling

In the microcontroller, a downsampling process is used to manage the high data rate from the sensors. Both accelerometer and gyroscope can provide several hundred samples per second. These values are much higher than the video frame rate. Some downsampling algorithms have been published previously [18]. In this study, the author chose the simple method of using the mean value, as in Eqn. (6.8) and Eqn. (6.9). Here, the values of the downsampling ratio (r_F and r_ω) are commonly chosen based on the ratios of the output data rates and the video frame rate.

$$\begin{bmatrix} F_x \\ F_y \\ F_z \end{bmatrix} = \frac{1}{r_F} \times \sum_{i=1}^{r_F} \begin{bmatrix} F_{x_i} \\ F_{y_i} \\ F_{z_i} \end{bmatrix} \tag{6.8}$$

$$\begin{bmatrix} \omega_x \\ \omega_y \\ \omega_z \end{bmatrix} = \frac{1}{r_\omega} \times \sum_{i=1}^{r_\omega} \begin{bmatrix} \omega_{x_i} \\ \omega_{y_i} \\ \omega_{z_i} \end{bmatrix} \tag{6.9}$$

6.2.4.2 Image Rotation

The image rotation is the last step in horizon stabilization. This process is performed by the software in the computer [20]. Only Φ is used to rectify the image orientation. The value of Θ is used to determine the region where the rectification should be skipped. When Θ is near $\pm 90^\circ$, horizon stabilization is meaningless.

6.2.4.3 Sensor Calibration

Sensor calibration before the first use is very important. In MEMS, the sensor error depends on the technology and on thermal stresses during soldering [37]. The calibration processes can be found in [36] for accelerometer and [26] for gyroscope. In this study, the accelerometer is calibrated for gain error and zero-g offset error. The gyroscope is calibrated for zero offset error only. All calibration factors are stored either in the microcontroller or in the computer.

6.3 Simulations

6.3.1 Simulation Setup

In simulations, a virtual IMU is created as shown in Fig. 6.5(a). Two functions f_1 and f_2 of time are used to control the continuous variability of the original tilt angles. The original angles were used to generate the ideal data. Two random noise sources n_1 and n_2 are added to ω_k and F_k to create the output data of the virtual IMU.

The simulations were conducted under various conditions. Four basic conditions were used: (i) fully static; (ii) linear acceleration only; (iii) rotation with small background vibration; and (iv) combined linear acceleration and rotation.

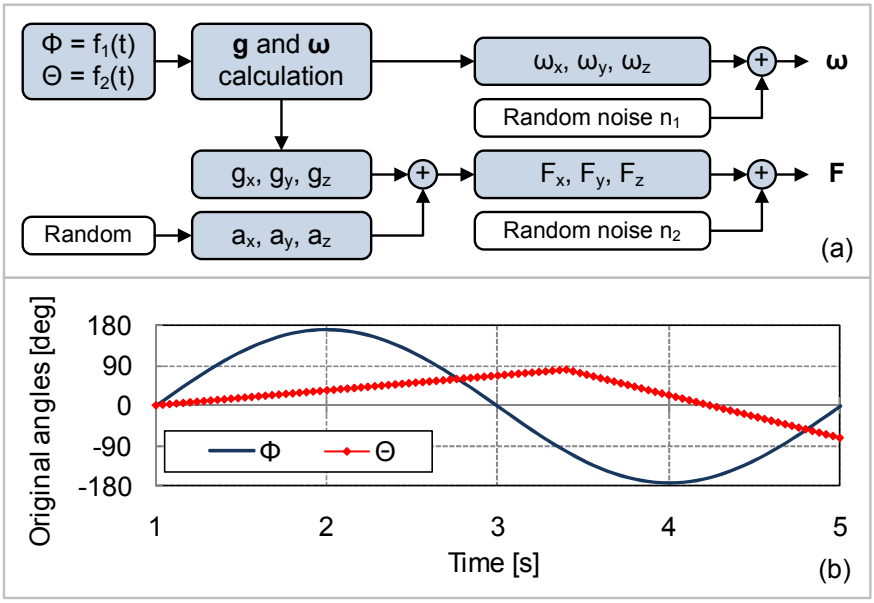

Figure 6.5: Generating the simulation data in the virtual IMU: (a) schematic diagram of virtual IMU and (b) original tilt angles for conditions (iii) and (iv), Φ changes as a sine function and Θ changes as a linear function

In conditions (i) and (ii), tilt angles are constant, $\Phi = -45$ deg and $\Theta = 30$ deg. In conditions (iii) and (iv), f_1 is a sine function and f_2 is a linear function, as shown in Fig. 6.5(b). The testing intensities of the linear acceleration were 0 m/s^2, 3 m/s^2, and 10 m/s^2 (about 1 g). The background vibration was 0.5 m/s^2, n_2 was equivalent to an acceleration of 0.3 m/s^2. The reference method is based on that reported in [20], which is a well-known study on horizon stabilization in NOTES.

6.3.2 Simulation Results

The results are evaluated according to the following criteria: accuracy, noise removal, and time delay. In the simplest condition, fully static (i), both methods give the same precise results. Figure 6.6 shows the simulation results for condition (ii). There is ripple in the reference method whereas the proposed method correctly reflects the stability of the tilt angles. Figure 6.7 shows the results for

condition (iii). There is a time delay of about 0.2 s in the reference method. Figure 6.8 and Fig. 6.9 show the simulation results for the condition (iv). When the strength of linear acceleration is about 3 m/s^2, the reference method gives high ripple angles. In particular, when the intensity is 10 m/s^2, the results do not reflect the tilt angle information because the angles are frozen. In contrast, in both cases, the proposed method still follows the changes in the original tilt angles. Moreover, there is little sudden change.

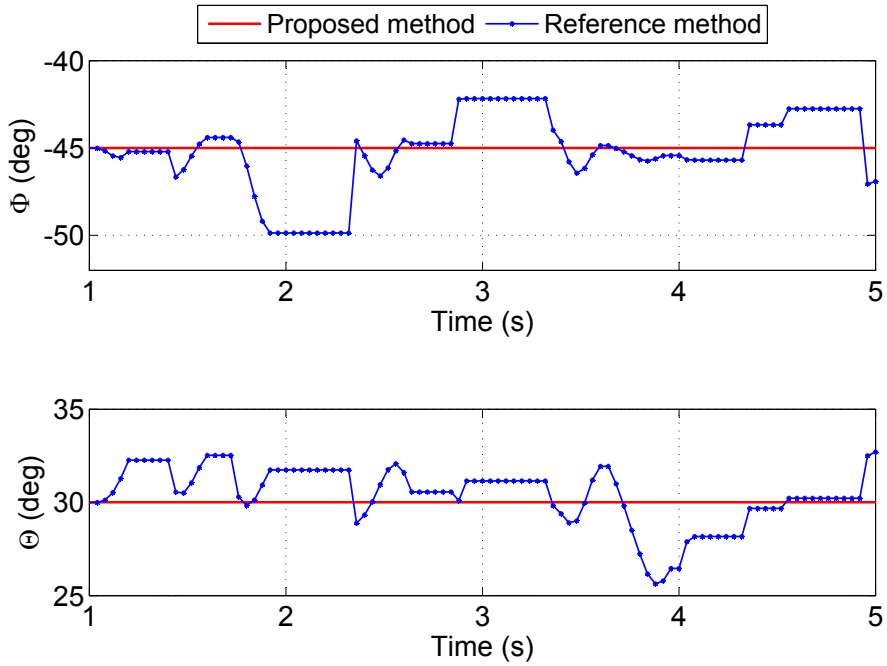

Figure 6.6: Simulation results under condition (ii), linear acceleration only: $a_{k_{max}} = 3$ m/s^2 and $\omega = 0$

6.4 Experiments

6.4.1 Experimental Setup

Two experiments were conducted: with a rotation frame and with a real camera. In the first experiment, the rotation frame (Fig. 6.10) is used again. Rotations about a_1 and a_2 are used to change Φ and Θ. The true values of the tilt angles

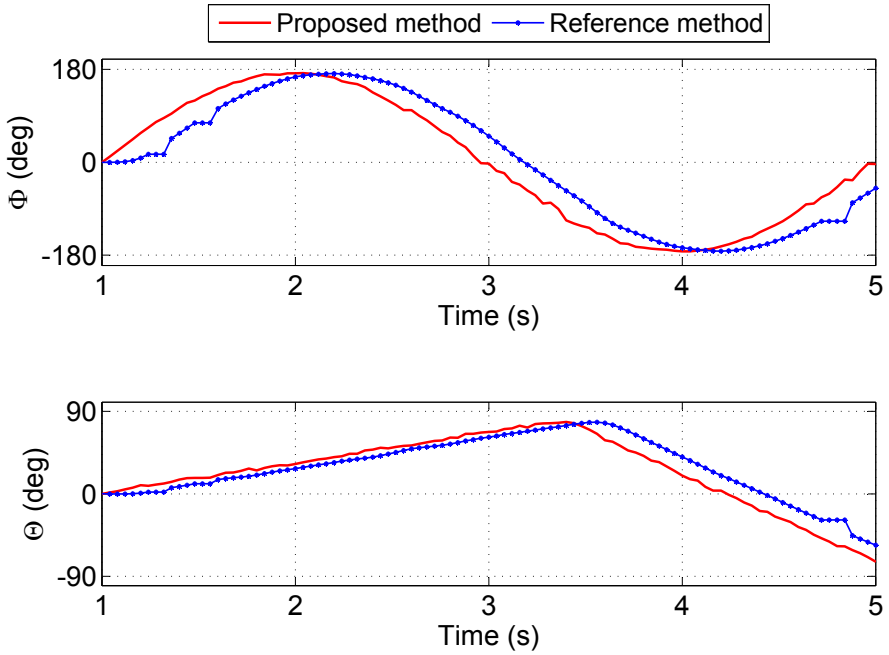

Figure 6.7: Simulation results under condition (iii), rotation with small background vibration: $a_{k_{max}} = 0.5$ m/s^2 and $\omega \neq 0$

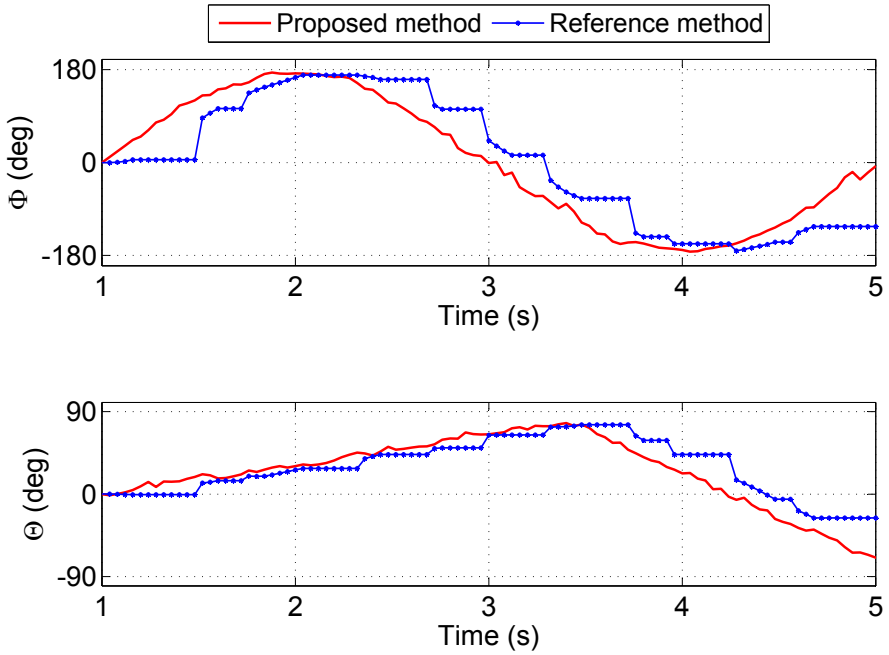

Figure 6.8: Simulation results under condition (iv), combined linear acceleration and rotation: $a_{k_{max}} = 3$ m/s^2 and $\omega \neq 0$

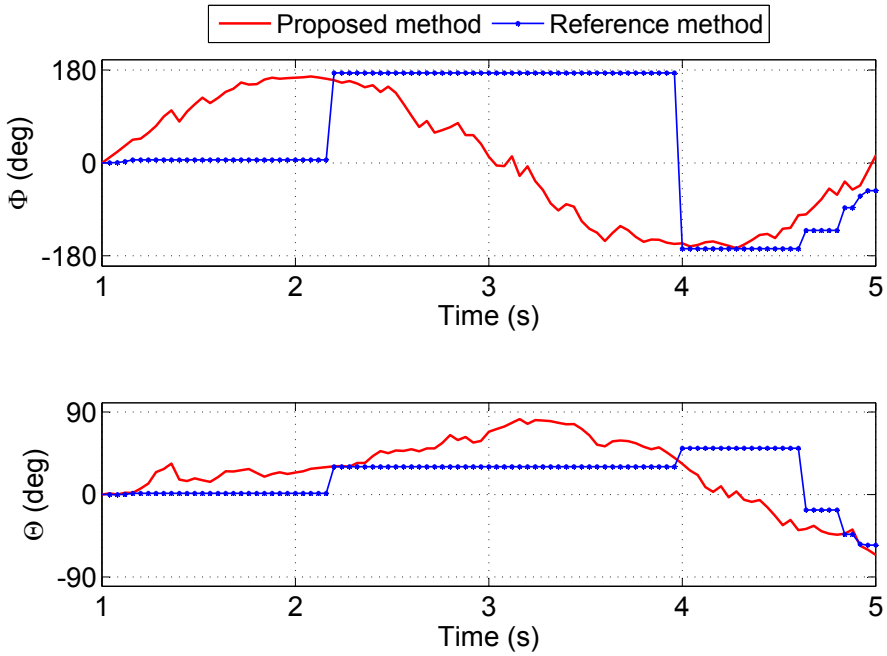

Figure 6.9: Simulation results under condition (iv), combined linear acceleration and rotation: $a_{k_{max}} = 10$ m/s^2 and $\omega \neq 0$

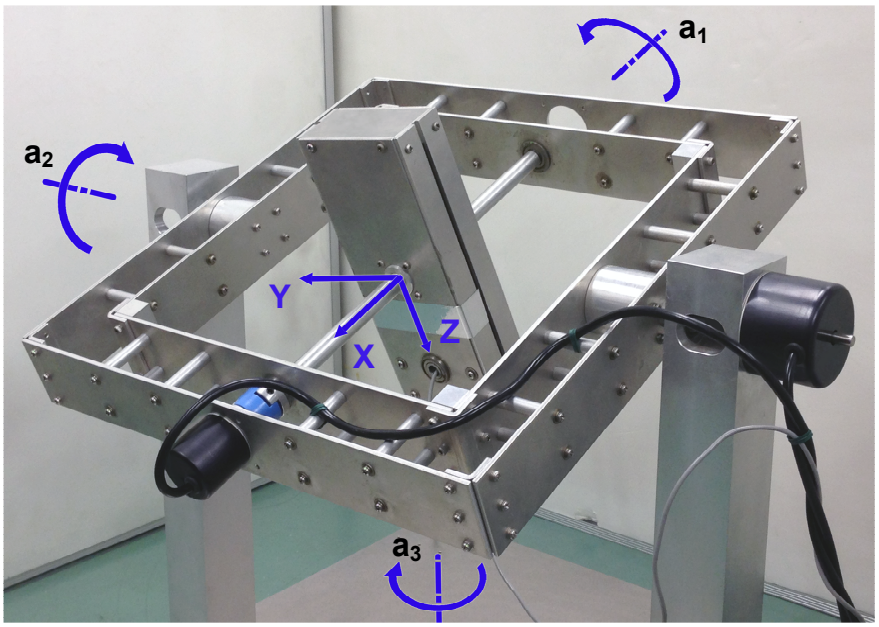

Figure 6.10: Rotation frame in the experiments

can be computed from two high-resolution encoders mounted along the a_1 and a_2 axes. The accelerometer has a resolution of 16 bits and a full scale of ± 2 g. The gyroscope also has a resolution of 16 bits and a full scale of 2000 deg/s. During each test, the box that contains the IMU was rotated by hand continuously. Both rotating direction and the angular velocity were changed smoothly to ensure that the maximum rate is not greater than the scale of the gyroscope. The motion noise was generated by a vibrator and the movement of the whole system on a horizontal surface. Both methods estimated the orientation of the IMU simultaneously; the results were recorded to being compared with the true angles provided by the encoders.

In the second experiment, the tilt angles of both methods were used to correct the orientation of real camera images. The camera was installed inside a circular frame, which made of paper. The frame was painted with many horizontal colorful lines to visually identify the image orientation. In this test, first, the camera was kept stable in some orientations to examine the performance of both methods in static conditions. After that, the camera was continuously moved and vibrated to verify the operation under dynamic conditions. In both cases, the better method can be determined by comparing the direction of the rectified video frames with the true orientation recognized by the colored lines.

6.4.2 Experimental Results

The first experiment confirmed the simulation results. Figure 6.11 shows the experimental results under a gentle motion; both methods give the good results. The time delay of the reference method is about 0.2 s whereas that of the proposed method is considerably smaller. When the motion becomes strong, as in Fig. 6.12, many frozen periods appear in the results of the reference method. The angles can be frozen up to 0.7 s. After these points, the tilt angles could change suddenly by hundreds of degrees in only one video frame. On the opposite side, during this time, the tilt angles of the proposed method still change smoothly.

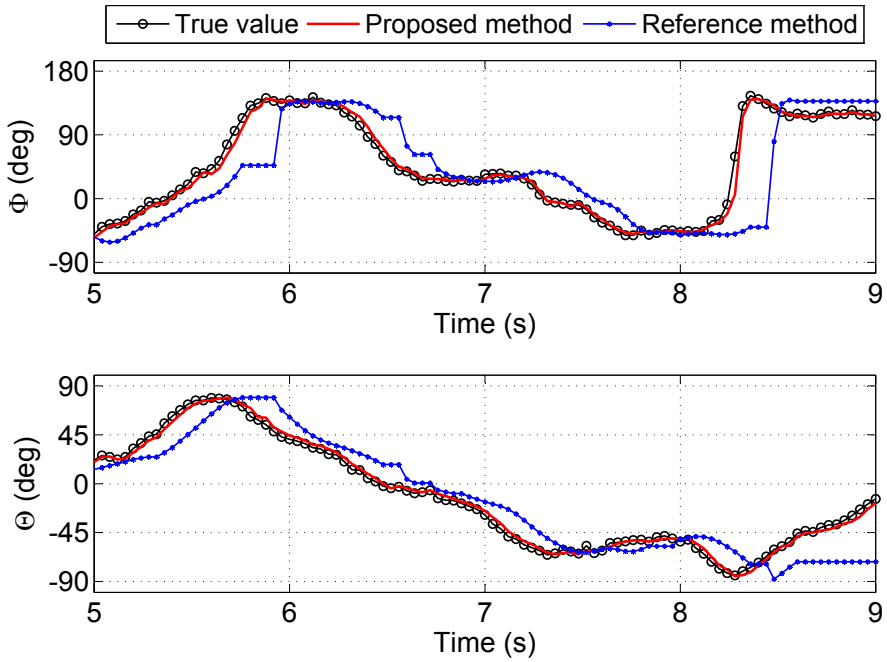

Figure 6.11: Experimental results when the motion noise is small

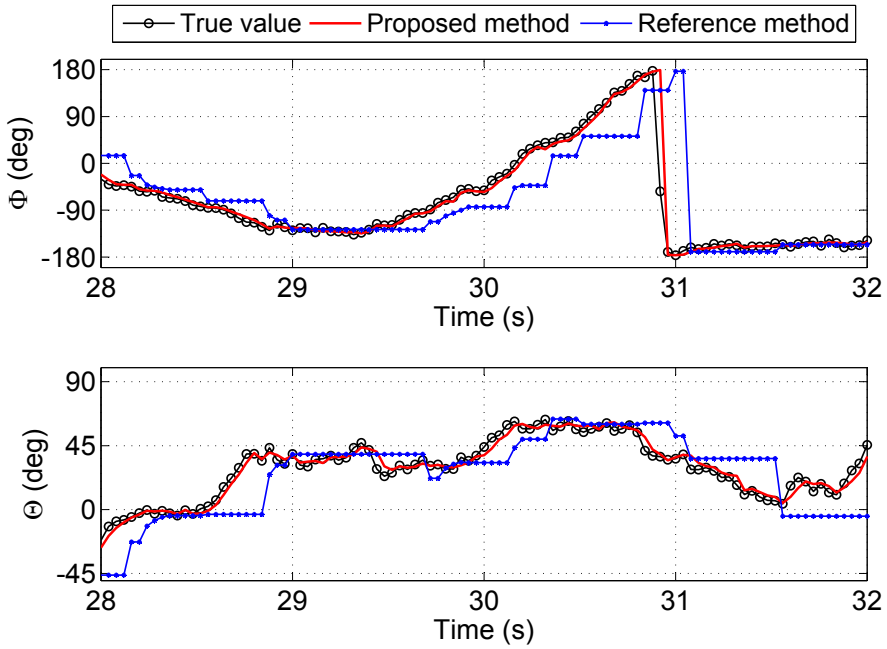

Figure 6.12: Experimental results under the strong motion

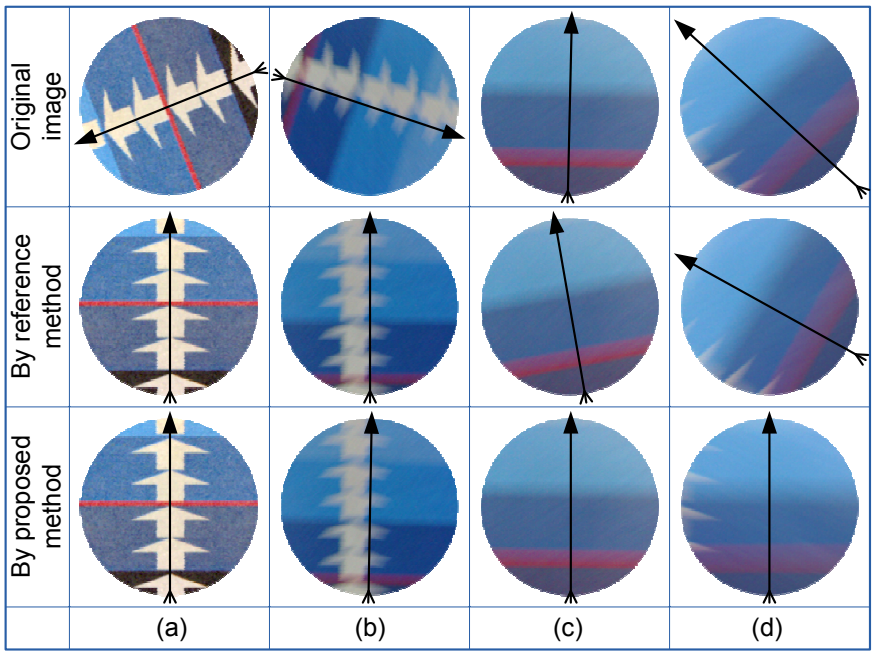

Figure 6.13: Using the output angles of both methods for horizon stabilization under some conditions: (a) static state, (b) weak motion, (c) strong motion, and (d) continuous strong motion

Figure 6.13 shows the testing results with real camera images. On each video frame, a black orientation-arrow is manually inserted based on the horizontal lines. In Fig. 6.13(a) and Fig. 6.13(b), when there is no motion or gentle motion, both output images are rectified without any error. In Fig. 6.13(c), under the stronger motion, the difference appears. Some skew video frames can be detected when using the angles of the reference method. In Fig. 6.13(d), the error becomes large because the angles are frozen under the continuous motion.

6.5 Discussion

In addition to the main advantages of a small error, small time delay, and smooth angle changes, the proposed method has other advantages. Because the algorithm relies on the basic trigonometric functions, the whole calculation process can be performed by low-performance systems. The compact software and its prediction

algorithm minimize the time delay. The response speed can be enhanced by changing the data rate. Lower downsampling ratios give a higher data rate and faster angle update, which may be useful in some cases.

Fast updating the angles has both advantages and drawbacks. The redundant data from the sensors is used to improve the reliability of the results by means of downsampling which is actually a simple low-pass-filter. Hence, by reducing the downsampling ratio, we can enhance the response speed and track any fast change in the orientation. Consequently, the accuracy could increase if the linear acceleration is minor. In the other cases, the accuracy depends on the spectrum of acceleration: high frequency vibrations may degrade the stability, while slow changes in the acceleration have less influence. In horizon stabilization, the response speed is limited by the video frame rate, an error of a few degrees is acceptable, and the stability of the results is important; therefore, using a high downsampling ratio (e.g., a ratio of 16 as in the simulations) or adding a digital filter for the output angles is a good option.

In general application, when the mentioned characteristic in Sec. 6.2.1.2 is not applicable, there is a common barrier for the inertial sensor-fusion techniques. If the linear acceleration vector is nonzero and constant during many time-steps, confusion could appear. Because $\mathbf{F}$ is the sum of $\mathbf{g}$ and $\mathbf{a}$, it is difficult to separate the effect of gravitational acceleration and linear acceleration. Even when $|\mathbf{F}|$ equals to $|\mathbf{g}|$, linear acceleration could be still changed continuously, as depicted in Fig. 6.14. In this case, the gyroscope can take effect. Because of sensor error and integration step, the precision may not be high. Better sensor-fusion technique guarantees higher precision during longer time. The proposed method should be evaluated under the similar condition in other research.

There are different opinions about spatial disorientation in NOTES. Beside many studies identified the necessity of a fixed horizon, Sodergren et al. had another view about horizon stabilization [44]. The NOSCAR working group also concluded that spatial disorientation can be overcome through practical experience [40]. However, these studies mention the combinations with a secondary image source or interface for higher-level NOTES procedures. In this sense, the orientation of each image could be an important reference. Another potential

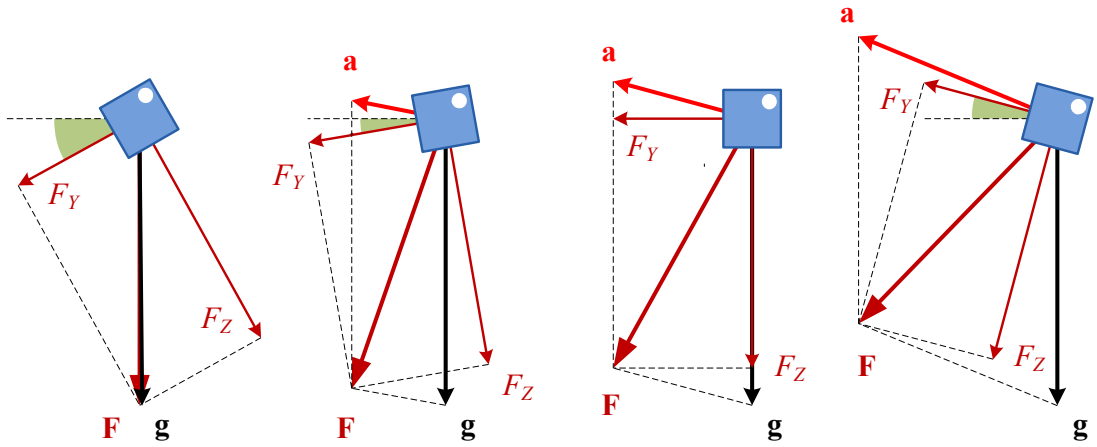

Figure 6.14: An example of the context in which the linear acceleration is nonzero and changed continuously while $|\mathbf{F}| = |\mathbf{g}|$ in many consecutive time-steps

application is in robot-assisted NOTES. Nowadays, the support of the surgical robots is not unusual [25, 38].

Although mounting the IMU on existing flexible endoscopes may limit the performance, this should be less of a problem for the newer devices, in which the sensors are directly integrated. The general purpose low-cost integrated MEMS is only $3 \times 3.5 \times 1$ mm. It is likely that a dedicated sensor for NOTES will be much smaller.

6.6 Conclusion

Estimating the spatial orientation in NOTES is necessary for developing new surgical devices. Hence, in this chapter, the author has proposed a new sensor-fusion method for estimating the orientation in the surgical system. Both simulation and experiment were conducted to evaluate the results. Compared with the reference method, the results of this study had notable advantages; it was more accurate and had a faster response. The flexible predict-and-choose algorithm allowed the tilt angles to be estimated without accumulation errors under various conditions,

including large vibration, random noise, and continuous movement. In addition, the IMU hardware is still small, simple, and similar to the existing devices.

In addition, the applicability of the study has also been considered. Although horizon stabilization, which is the common application, may not be necessary for some experienced surgeons, it could be helpful for other surgeons, gastroenterologists, and training activities. Other potential applications are in endoscopic image coupling, image stabilization, and surgical robots. Future studies may contribute to increasing the efficiency of dedicated surgical instruments for NOTES.

Chapter 7

Conclusions and Future Works

7.1 Conclusions

Tilt sensing is necessary for many applications in many fields. Although the tilt angles can be defined in some specific ways, they are measured by the same mechanism.

In this work, the author has proposed, developed, and validated two methods for partially overcoming the common challenges in the tilt measurement technique. The first method is introduced to address a drawback of the sensors, whereas the second one is proposed to solve a limitation of the measurement mechanism. Both methods have the same research objective that is to increase the measurement precision and accuracy when the system operates in the actual conditions.

The whole work is divided into four elemental studies and presented in seven chapters. The work starts with an introduction of the main contents including research objectives and major contributions. In the next chapter, the technical background is briefly presented and the related works are reviewed. The contents of this chapter are very important for the remaining parts because they provide the most necessary concepts in tilt measurement, all terminologies in the subsequent descriptions, and basic formulas for developing more complicated equations.

The chapter ends with a summary of challenges and prevailing solutions in tilt measurement.

On the basis of these challenges, the author has proposed four elemental studies in four consecutive chapters. They are also the main contributions of this work; the detailed achievements are summarized as below:

- In chapter 3, the method of interference reduction in measuring the pitch angle can reduce the noise power 165 times (about 22 dB) and error in the pitch angle 2–20 times, when using the analog accelerometers. In other words, this method can improve the EMI immunity of the second angle in the yaw-pitch-roll sequence Euler angles without the need for any additional software and hardware.

- In chapter 4, the method of interference reduction in measuring the roll angle can reduce the noise power 230 times (about 23.6 dB) and error in the roll angle 5–22.5 times, when using the analog accelerometers. Hence, this method can improve the EMI immunity of the third angle with a minimum resource. It should be noted that the first angle in this sequence (yaw angle) is not the tilt and cannot be determined by the accelerometers.

- In chapter 5, the method of interference reduction in measuring both components of the tilt when these components are defined by the non-Euler angles has been proposed and theoretically proved. After that, the overall evaluations of the three presented studies have been summarized; and the alternative design for each study has been introduced.

- In chapter 6, the method of sensor-fusion for tilt measurement in surgical devices has been proposed and successfully validated by simulations and experiments. The new algorithm allowed the tilt angles to be estimated without accumulation errors under various conditions, including large vibration, random noise, and continuous movement.

In conclusion, the above studies have been successfully presented and their results could contribute to increasing the applicability of the tilt sensing technique

in the medical field. Moreover, the results of some chapters can be applied to the measurement systems in a variety of fields.

7.2 Future Works

The studies in this work would be more useful and their applicability could be expanded if the following works can be supplemented:

- In the methods of EMI reduction, the works which need to be performed or should be solved by the better solutions are: (1) sensor calibration, (2) crosstalk in the twisted cable, and (3) the possibility of sensor-fusion after changing the mounting orientation. The improvements could be:

  In (1), a more advanced calibration process should be proposed to reduce the systematic errors because in practical implementation, there may be significant misalignment in the rotated orientation of the sensor. The misalignment can cause remarkable systematic errors in the computed angles. Hence, the author is going to propose a method by which the misalignment can be quantified and then the angles can be corrected.

  In (2), the effects of crosstalk in the twisted cables need to be simulated and measured. The results will be used to identify the suggested parameters of the twisted cable when the bandwidth of the signals is given. In an ongoing progress, the author uses the electrical model of the twisted pairs to simulate the coupling effect in the three-core twisted cable. The results will be available in a near future.

  In (3), an algorithm to combine the data of the rotated accelerometer and other sensors need to be taken into account. As mentioned in Sec. 2.3.3, the combination of several sensors may be required to estimate the gravitation components in the dynamic conditions. Consequently, the data of the rotated sensor need to be processed by new sensor-fusion methods.

- In the study presented in chapter 6, the proposed method should be compared with other methods which use both accelerometer and gyroscope in

general conditions. The results could be helpful for other authors, engineers, or technicians when choosing the solution for their works or their designs in other fields. The comparison between the performances of the method when changing its parameters should be also performed. The results would be an important reference if the proposed sensor-fusion method is utilized in another study.

If the above works are conducted in further studies and desired results are obtained, the method of EMI reduction will be an effective solution for many applications and a variety of fields; meanwhile the method of sensor-fusion provides another choice for related studies in the future.

Appendices

Appendix A

Equations Formulation for the Pitch Angle

The following appendices present the detailed steps of equations formulation for the alternative solutions of the three studies in chapters 3, 4, and 5. In each appendix, for convenience, the equations are indexed similar to those in the corresponding study. Hence, the descriptions of the whole process can be omitted.

The first appendix presents the detailed steps of equations formulation for the alternative solution of the design in chapter 3, EMI reduction for the pitch angle.

$$R'_{\Theta} = R_Z(\gamma)$$

$$= \begin{bmatrix} \cos\gamma & \sin\gamma & 0 \\ -\sin\gamma & \cos\gamma & 0 \\ 0 & 0 & 1 \end{bmatrix} \tag{A.1}$$

$$R'_{\Theta} = \frac{1}{2}\begin{bmatrix} \sqrt{2} & \sqrt{2} & 0 \\ -\sqrt{2} & \sqrt{2} & 0 \\ 0 & 0 & 2 \end{bmatrix} \tag{A.2}$$

$$\frac{1}{|\mathbf{g}|}\begin{bmatrix} g_x \\ g_y \\ g_z \end{bmatrix} = R'_{\Theta}\frac{1}{|\mathbf{g}|}\begin{bmatrix} g_X \\ g_Y \\ g_Z \end{bmatrix} \tag{A.3}$$

$$\frac{1}{|\mathbf{g}|}\begin{bmatrix} g_x \\ g_y \\ g_z \end{bmatrix} = \frac{1}{2}\begin{bmatrix} -\sqrt{2}\sin\Theta + \sqrt{2}\cos\Theta\sin\Phi \\ \sqrt{2}\sin\Theta + \sqrt{2}\cos\Theta\sin\Phi \\ 2\cos\Theta\cos\Phi \end{bmatrix} \tag{A.4}$$

$$\sin\Theta = \frac{\sqrt{2}}{2}\frac{(g_y - g_x)}{|\mathbf{g}|} \tag{A.5}$$

$$\frac{(g_x + g_y)}{|\mathbf{g}|} = \sqrt{2}\cos\Theta\sin\Phi \tag{A.6}$$

$$\frac{g_z}{|\mathbf{g}|} = \cos\Theta\cos\Phi \tag{A.7}$$

$$\tan\Phi = \frac{g_x + g_y}{\sqrt{2}g_z} \tag{A.8}$$

$$\sin\Theta = \frac{\sqrt{2}}{2}\frac{(U_y - U_x)}{\sqrt{U_x^2 + U_y^2 + U_z^2}} \tag{A.9}$$

$$\tan\Phi = \frac{U_x + U_y}{\sqrt{2}U_z} \tag{A.10}$$

Appendix B

Equations Formulation for the Roll Angle

This appendix presents the detailed steps of equations formulation for the alternative solution of the design in chapter 4, EMI reduction for the roll angle.

$$\begin{bmatrix} \beta \\ \alpha \end{bmatrix} = \begin{bmatrix} \arctan\sqrt{2} \\ \pi/4 \end{bmatrix} \tag{B.1}$$

$$\begin{aligned} R'_{\Phi} &= R_X(\alpha)R_Y(\beta) \\ &= \begin{bmatrix} \cos\beta & 0 & -\sin\beta \\ \sin\beta\sin\alpha & \cos\alpha & \cos\beta\sin\alpha \\ \cos\alpha\sin\beta & -\sin\alpha & \cos\beta\cos\alpha \end{bmatrix} \end{aligned} \tag{B.2}$$

$$R'_{\Phi} = \frac{\sqrt{6}}{6}\begin{bmatrix} \sqrt{2} & 0 & -2 \\ \sqrt{2} & \sqrt{3} & 1 \\ \sqrt{2} & -\sqrt{3} & 1 \end{bmatrix} \tag{B.3}$$

$$\frac{1}{|\mathbf{g}|}\begin{bmatrix} g_x \\ g_y \\ g_z \end{bmatrix} = R'_{\Phi}\begin{bmatrix} -\sin\Phi \\ \cos\Theta\sin\Phi \\ \cos\Theta\cos\Phi \end{bmatrix} \tag{B.4}$$

$$\frac{1}{|\mathbf{g}|}\begin{bmatrix} g_x \\ g_y \\ g_z \end{bmatrix} = \frac{\sqrt{6}}{6}\begin{bmatrix} -\sqrt{2}\sin\Theta - 2\cos\Theta\cos\Phi \\ -\sqrt{2}\sin\Theta + \sqrt{3}\cos\Theta\sin\Phi + \cos\Theta\cos\Phi \\ -\sqrt{2}\sin\Theta - \sqrt{3}\cos\Theta\sin\Phi + \cos\Theta\cos\Phi \end{bmatrix} \tag{B.5}$$

$$\frac{(g_y - g_z)}{|\mathbf{g}|} = \sqrt{2}\cos\Theta\sin\Phi \tag{B.6}$$

$$\frac{(g_z + g_y - 2g_x)}{|\mathbf{g}|} = \sqrt{6}\cos\Theta\cos\Phi \tag{B.7}$$

$$\frac{(g_x + g_y + g_z)}{|\mathbf{g}|} = -\sqrt{3}\sin\Theta \tag{B.8}$$

$$\tan\Phi = \frac{\sqrt{3}(g_y - g_z)}{g_z + g_y - 2g_x} \tag{B.9}$$

$$\sin\Theta = -\frac{(g_x + g_y + g_z)}{\sqrt{3}\sqrt{g_x^2 + g_y^2 + g_z^2}} \tag{B.10}$$

$$\Phi = \arctan 2\left\{\sqrt{3}(U_y - U_z), [(U_z - U_x) + (U_y - U_x)]\right\} \tag{B.11}$$

$$\Theta = \arcsin\left[-\frac{(U_x + U_y + U_z)}{\sqrt{3}\sqrt{U_x^2 + U_y^2 + U_z^2}}\right] \tag{B.12}$$

Appendix C

Equations Formulation for the Non-Enler Angles

This appendix presents the detailed steps of equations formulation for the alternative solution of the design in chapter 5, EMI reduction for both non-Euler angles.

$$\begin{bmatrix} \beta \\ \gamma \end{bmatrix} = \begin{bmatrix} -\arctan\sqrt{2} \\ -\pi/4 \end{bmatrix} \tag{C.1}$$

$$R'_{\theta_{1,2}} = R_Z(\gamma)R_Y(\beta) = \begin{bmatrix} \cos\beta\cos\gamma & \sin\gamma & -\cos\gamma\sin\beta \\ -\cos\beta\sin\gamma & \cos\gamma & \sin\beta\sin\gamma \\ \sin\beta & 0 & \cos\beta \end{bmatrix} \tag{C.2}$$

$$R'_{\theta_{1,2}} = \frac{\sqrt{6}}{6}\begin{bmatrix} 1 & -\sqrt{3} & \sqrt{2} \\ 1 & \sqrt{3} & \sqrt{2} \\ -2 & 0 & \sqrt{2} \end{bmatrix} \tag{C.3}$$

$$\begin{bmatrix} g_x \\ g_y \\ g_z \end{bmatrix} = \frac{\sqrt{6}}{6}\begin{bmatrix} g_X - \sqrt{3}g_Y + \sqrt{2}g_Z \\ g_X + \sqrt{3}g_Y + \sqrt{2}g_Z \\ -2g_X + \sqrt{2}g_Z \end{bmatrix} \tag{C.4}$$

$$g_x + g_y - 2g_z = \sqrt{6}g_X \tag{C.5}$$

$$g_y - g_x = \sqrt{2} g_Y \tag{C.6}$$

$$\theta_1 = \arcsin\left(-\frac{g_X}{|\mathbf{g}|}\right)$$

$$= \arcsin\left[\frac{1}{\sqrt{6}} \frac{(2g_z - g_y - g_x)}{\sqrt{g_x^2 + g_y^2 + g_z^2}}\right] \tag{C.7}$$

$$\theta_2 = \arcsin\left(-\frac{g_Y}{|\mathbf{g}|}\right)$$

$$= \arcsin\left[\frac{1}{\sqrt{2}} \frac{(g_x - g_y)}{\sqrt{g_x^2 + g_y^2 + g_z^2}}\right] \tag{C.8}$$

$$\theta_1 = \arcsin\left\{\frac{1}{\sqrt{6}} \frac{[(U_z - U_y) + (U_z - U_x)]}{U}\right\} \tag{C.9}$$

$$\theta_2 = \arcsin\left[\frac{1}{\sqrt{2}} \frac{(U_x - U_y)}{U}\right] \tag{C.10}$$

References

[1] ADXL335: Small, Low Power, 3-Axis $\pm 3g$ Accelerometer data sheet.

[2] KXR94-2050: $\pm 2g$ Tri-Axis Accelerometer Specifications data sheet.

[3] KXSC7-2050: $\pm 2g$ Tri-Axis Analog Accelerometer Specifications data sheet.

[4] MMA7361LC: $\pm 1.5g$, $\pm 6g$ Three Axis Low-g Micromachined Accelerometer data sheet.

[5] Stereo Hi-Fi Balun 500028, 500028-F data sheet.

[6] T. G. Constandinou and J. Georgiou. Micropower arcsine circuit for tilt processing. *Electronics Letters*, **44**:1336–1338, November 2008.

[7] H. V. Dao, T. T. Nguyen, and T. Komeda. Reducing the influence of vibration and movement in endoscopic orientation estimation with inertial sensors. In *CARS 2015–Computer Assisted Radiology and Surgery Proceedings of the 29th International Congress and Exhibition*, pages S117–S118, Barcelona, Spain, June 2015.

[8] Hung V. Dao and Takashi Komeda. Estimating endoscopic orientation in static and dynamic states with inertial sensors. *Journal of Medical Devices - Transaction of the ASME*, **10**(4):041003–041003–7, December 2016.

[9] Hung V. Dao, Takashi Komeda, and Trung T. Nguyen. Interference reduction in tilt measurement based on changing the sensor mounting method and calculation formulas. *Journal of Automation and Control Engineering*, **4**(6):424–429, December 2016.

[10] Hung Viet Dao and Takashi Komeda. Noise reduction based on a new sensor mounting method in tilt measurement with analog accelerometer. In *Proceedings of 10th South East Asian Technical University Consortium (SEATUC) Symposium*, February 2016.

[11] Hung Viet Dao, Takashi Komeda, and Trung Thanh Nguyen. Development and validation of a new interference cancellation method for accelerometers in orientation measurement. In *2016 11th France-Japan & 9th Europe-Asia Congress on Mechatronics (MECATRONICS) /17th International Conference on Research and Education in Mechatronics (REM)*, pages 152–157, Compiègne, France, June 2016.

[12] Hooman Dejnabadi, Brigitte M. Jolles, and Kamiar Aminian. A new approach to accurate measurement of uniaxial joint angles based on a combination of accelerometers and gyroscopes. *IEEE Transactions on Biomedical Engineering*, **52**(8):1478–1484, August 2005.

[13] James Diebel. Representing attitude: Euler angles, unit quaternions, and rotation vectors. Technical reference, Stanford University, Stanford, CA, October 2006.

[14] Xavier Dray and Anthony N. Kalloo. History of NOTES. In Anthony N. Kalloo, Jacques Marescaux, and Ricardo Zorron, editors, *Natural Orifice Translumenal Endoscopic Surgery: Textbook and Video Atlas*, Chapter 1, pages 3–11. Wiley-Blackwell, New Jersey, 1^{st} edition, June 2012.

[15] Eugene L. Duke, Robert F. Antoniewicz, and Keith D. Krambeer. Derivation and definition of a linear aircraft model. NASA reference publication 1207, National Aeronautics and Space Administration (NASA), Adwards, CA, August 1988.

[16] Fletcher Dunn and Ian Parberry. *3D Math Primer for Graphics and Game Development*, chapter 8. CRC Press, Taylor & Francis Group, Boca Raton, FL, 2011.

[17] Kim Fowler. Grounding and shielding. II. Grounding and return. IEEE Instrumentation and Measurement Magazine, June 2000.

[18] K. Höller, J. Penne, A. Schneider, J. Jahn, H. Girgis, J. Guttiérrez, T. Wittenberg, H. Feussner, and J. Hornegger. Suppression of shock based errors with gravity related endoscopic image rectification. In *Proceedings of 5th Russian-Bavarian Conference on Bio-Medical Engineering*, pages 43–47, Munich, Germany, July 2009.

[19] Kurt Höller, Jochen Penne, Joachim Hornegger, Armin Schneider, Sonja Gillen, Hubertus Feussner, Jasper Jahn, Javier Guttiérrez, and Thomas Wittenberg. Clinical evaluation of endorientation: Gravity related rectification for endoscopic images. In *Proceedings of 6th International Symposium on Image and Signal Processing and Analysis (ISPA 2009)*, pages 713–717, Salzburg, Austria, September 2009. IEEE.

[20] Kurt Höller, Jochen Penne, Armin Schneider, Jasper Jahn, Javier Guttiérrez, Thomas Wittenberg, Hubertus Feussner, and Joachim Hornegger. Endoscopic orientation correction. In *Medical Image Computing and Computer-Assisted Intervention – MICCAI 2009*, **5761** of *Lecture Notes in Computer Science*, pages 459–466, London, UK, September 2009. Springer.

[21] Howard Johnson and Martin Graham. *High-Speed Signal Propagation: Advanced Black Magic*, chapter 6. Prentice Hall, New Jersey, 2003.

[22] Chul Woo Kang and Chan Gook Park. Attitude estimation with accelerometers and gyros using fuzzy tuned kalman filter. In *Control Conference (ECC), 2009 European*, pages 3713–3718, Budapest, Hungary, August 2009.

[23] Alfonso Lago, Carlos M. Peñalver, Jorge Marcos, Jesús Doval-Gandoy, Andrés Nogueiras Meléndez, Óscar López, Félix Santiago, Francisco D. Freijedo, José Manuel Vilas, and

José Carlos Lorenzo. Geometric analysis and manufacturing considerations for optimizing the characteristics of a twisted pair. *IEEE Transactions on Electronics Packaging Manufacturing*, **32**:22–31, January 2009.

[24] Rebecka Larsdotter and David Jaller. *Automatic Calibration and Virtual Alignment of MEMS-Sensor Placed in Vehicle for Use in Road Condition Determination System*. Master's thesis, Chalmers University of Technology, Gothenburg, Sweden, 2014.

[25] Amy C. Lehman, Jason Dumpert, Nathan A. Wood, Lee Redden, Abigail Q. Visty, Shane Farritor, Brandon Varnell, and Dmitry Oleynikov. Natural orifice cholecystectomy using a miniature robot. *Surgical Endoscopy*, **23**(2):260–266, February 2009.

[26] Mark Looney. A simple calibration for MEMS gyroscopes. On EDN Europe, July 2010.

[27] Sergiusz Luczak and Waldemar Oleksiuk. Increasing accuracy of tilt measurements. *Engineering Mechanics*, **14**:143–154, January 2007.

[28] Sergiusz Luczak, Waldemar Oleksiuk, and Maciej Bodnicki. Sensing tilt with MEMS accelerometers. *IEEE Sensors Journal*, **6**:1669–1675, December 2006.

[29] H. J. Luinge and P. H. Veltink. Measuring orientation of human body segments using miniature gyroscopes and accelerometers. *Medical and Biological Engineering and Computing*, **43**(2):273–282, April 2005.

[30] H. J. Luinge, P. H. Veltink, and C. T. M. Baten. Estimating orientation with gyroscopes and accelerometers. *Technology and Health Care*, **7**(6):455–459, 1999.

[31] Henk J. Luinge and Peter H. Veltink. Inclination measurement of human movement using a 3-D accelerometer with autocalibration. *IEEE Transactions on Neural Systems and Rehabilitation Engineering*, **12**(1):112–121, March 2004.

[32] F. Landis Markley and John L. Crassidis. *Fundamentals of Spacecraft Attitude Determination and Control*, chapter 2. Springer New York, New York, 2014.

[33] Michael F. McGee, Michael J. Rosen, Jeffrey Marks, Raymond P. Onders, Amitabh Chak, Ashley Faulx, Victor K. Chen, and Jeffrey Ponsky. A primer on natural orifice transluminal endoscopic surgery: Building a new paradigm. *Surgical Innovation*, **13**(2):86–93, June 2006.

[34] Michael C. Meadows and Ronald S. Chamberlain. A review on the status of natural orifice transluminal endoscopic surgery (NOTES) cholecystectomy: Techniques and challenges. *Open Access Surgery*, **2010**(3):73–86, September 2010.

[35] Bram Nauta and Gian Hoogzaad. Substrate bounce in mixed-mode CMOS ICs. In Johan Huijsing, Rudy Plassche, and Willy Sansen, editors, *Analog Circuit Design: Volt Electronics; Mixed-Mode Systems; Low-Noise and RF Power Amplifiers for Telecommunication*.

[36] Mark Pedley. High precision calibration of a three-axis accelerometer. Application Note AN4399 Rev. 1 of Freescale Semiconductor, January 2013.

[37] Mark Pedley. Tilt sensing using a three-axis accelerometer. Application Note AN3461 Rev. 6 of Freescale Semiconductor, March 2013.

[38] Claudio Quaglia, Gianluigi Petroni, Marta Niccolini, Sebastiano Caccavaro, Paolo Dario, and Arianna Menciassi. Design of a compact robotic manipulator for single-port laparoscopy. *ASME Journal of Mechanical Design*, **136**(10):105001–105001–9, October 2014.

[39] D. Rattner and A. Kalloo. ASGE/SAGES working group on natural orifice translumenal endoscopic surgery. *Surgical Endoscopy*, **20**(2):329–333, February 2006.

[40] David W. Rattner, Robert Hawes, Steven Schwaitzberg, Michael Kochman, and Lee Swanstrom. The second SAGES/ASGE white paper on natural orifice transluminal endoscopic surgery: 5 years of progress. *Surgical Endoscopy*, **25**(8):2441–2448, August 2011.

[41] Jean-Michel Redouté and Anna Richelli. A methodological approach to emi resistant analog integrated circuit design. IEEE Electromagnetic Compatibility Magazine.

[42] Anna Richelli. EMI susceptibility issue in analog front-end for sensor applications. *Journal of Sensors*, **2016**, November 2015. Article ID 1082454.

[43] Anna Richelli and Jean-Michel Redouté. Increasing the emi immunity of cmos operational amplifiers using an on-chip common-mode cancellation circuit. In *Proceedings of the 2014 International Symposium on Electromagnetic Compatibility*, pages 698–702, Gothenburg, September 2014.

[44] Mikael H. Sodergren, Alexander Warren, Jean Nehme, James Clark, Sonja Gillen, Hubertus Feussner, Julian Teare, Ara Darzi, and Guang-Zhong Yang. Endoscopic horizon stabilization in natural orifice translumenal endoscopic surgery: A randomized controlled trial. *Surgical Innovation*, **21**(1):74–79, 2014.

[45] STMicroelectronics. *Tilt Measurement Using a Low-g 3-Axis Accelerometer*, 2010.

[46] Gabriel Vasilescu. *Electronic Noise and Interfering Signals: Principles and Applications*, chapter 9. Springer Berlin Heidelberg, New York, 2005.

[47] Alexander Warren, Peter Mountney, David Noonan, and Guang-Zhong Yang. Horizon stabilized—dynamic view expansion for robotic assisted surgery (HS-DVE). *International Journal of Computer Assisted Radiology and Surgery*, **7**(2):281–288, March 2012.

[48] R. Williamson and B. J. Andrews. Detecting absolute human knee angle and angular velocity using accelerometers and rate gyroscopes. *Medical and Biological Engineering and Computing*, **39**(3):294–302, May 2001.

List of Publications

[P.1] Hung V. Dao, and Takashi Komeda, "Estimating Endoscopic Orientation in Static and Dynamic States With Inertial Sensors," *Journal of Medical Devices – Transaction of the ASME*, **10**(4):041003–041003–7, doi:10.1115/1.4033332, December 2016 (print version).

[P.2] Hung V. Dao, Takashi Komeda, and Trung T. Nguyen, "Interference Reduction in Tilt Measurement Based on Changing the Sensor Mounting Method and Calculation Formulas," *Journal of Automation and Control Engineering*, **4**(6):424–429, doi:10.18178/joace.4.6.424-429, December 2016 (print version).

[P.3] H. V. Dao, T. T. Nguyen, and T. Komeda, "Reducing the Influence of Vibration and Movement in Endoscopic Orientation Estimation with Inertial Sensors," *Computer Assisted Radiology and Surgery 29th International Congress and Exhibition*, Barcelona, Spain, pp. S117–S118, June 2015.

[P.4] Hung Viet Dao, and Takashi Komeda, "Noise Reduction Based on a New Sensor Mounting Method in Tilt Measurement with Analog Accelerometer," *10th South East Asian Technical University Consortium (SEATUC) Symposium*, Tokyo, Japan, Paper No. PS11-02 7-SIT048, February 2016.

[P.5] Hung Viet Dao, Takashi Komeda, and Trung Thanh Nguyen, "Development and Validation of a New Interference Cancellation Method for Accelerometers in Orientation Measurement," *11th France-Japan & 9th Europe-Asia*

Congress on Mechatronics (MECATRONICS) /17th International Conference on Research and Education in Mechatronics (REM), Compiègne, France, pp. 152–157, June 2016.

[P.6] Trung Nguyen, Takashi Komeda, and Hung Dao, "Design and Model a Novel Ankle Foot Orthosis," *26th European Modeling and Simulation Symposium*, Bordeaux, France, pp. 47–53, September 2014.

[P.7] Trung Nguyen, Hung Dao, and Takashi Komeda, "A Novel Active Ankle Orthosis System: Idea and Design," *2014 International Conference on Mechatronics and Mechanical Design*, Hong Kong, Paper No. F021, December 2014.

[P.8] Trung Nguyen, Hung Dao, and Takashi Komeda, "Phase Detection and Foot Drop Prevention for the Novel Powered Ankle Foot Orthosis System," *9th i-CREATe 2015 international Convention on Rehabilitation Engineering & Assistive Technology*, Singapore, Article No. 13, August 2015.